BERGISCHE UNIVERSITÄT WUPPERTAL

Fakultät für Elektrotechnik, Informationstechnik und Medientechnik

Heat Transport in Metal Halide Perovskite Semiconductors

zur Erlangung des akademischen Grades eines Doktors der Ingenieurwissenschaften (Dr.-Ing.) genehmigte

Dissertation

von

M. Sc. Tobias Haeger

Referenten:

Prof. Dr. rer. nat. Thomas Riedl

Prof. Dr. rer. nat. Daniel Neumaier

Eingereicht am: 06.09.2022

Mündliche Prüfung am: 18.11.2022

Vorwort/Preface

Die vorliegende Dissertation entstand im Rahmen meiner Tätigkeit als wissenschaftlicher Mitarbeiter am *Lehrstuhl für Elektronische Bauelemente* an der Bergischen Universität Wuppertal.

An erster Stelle möchte ich mich herzlich bei meinem Doktorvater Prof. Dr. rer. nat. Thomas Riedl bedanken. Nicht nur für die Möglichkeit zur Anfertigung dieser Dissertation, sondern auch für seine fachliche Betreuung sowie die zahlreichen Diskussionen und Ratschläge. Die Zusammenarbeit, die erlangten Erkenntnisse und die Möglichkeit diese auf Konferenzen vorstellen zu können, habe ich als etwas Besonderes empfunden.

Für die Übernahme des Koreferats und das Erstellen des Gutachtens möchte ich mich bei Herrn Prof. Dr. rer. nat. Daniel Neumaier herzlich bedanken.

Ein großes Dankeschön geht an meinen Betreuer, Herrn Dr.-Ing. Ralf Heiderhoff, für seinen unermüdlichen Einsatz mich bei meiner Forschung zu unterstützen. Mit vielen Fachgesprächen und Tipps half er mir nicht nur bei dem Verfassen von Veröffentlichungen und Vorbereiten von Vorträgen, sondern auch bei der praktischen Arbeit. Für die Zusammenarbeit und die geteilte Erfahrung bedanke ich mich herzlich.

Herrn Dr.-Ing. Detlef Theirich danke ich für die vielen wissenschaftlichen Ratschläge bezüglich meiner Arbeit. Die Diskussionen über meine Forschungsergebnisse und wie diese präsentiert werden, halfen mir bei meiner wissenschaftlichen Arbeit enorm.

Ich blicke auf eine schöne und stets freundliche Zeit am Lehrstuhl zurück, was insbesondere an dem großartigen Team liegt. Die Zusammenarbeit habe ich sehr genossen. Dazu bedanke ich mich bei den aktuellen sowie ehemaligen Mitarbeitern: Tim Becker, Dr.-Ing. Andreas Behrendt, Kai Oliver Brinkmann, Maïmouna Wagane Diouf, Dr.-Ing. Tobias Gahlmann, Tim Hasselmann, Dr.-Ing. Lukas Hoffmann, Dr. Junjie He, Ting Hu, Eun Gyo Jeong, Ahmed Kadid, Cagdas Kocak, Cedric Kreusel, Dr. Naho Kurahashi, Andreas Makris, Timo Maschwitz, Bujamin Misimi, Dr. Alex Palma-Cando, Dr.-Ing. Neda Pourdavoud, Manuel Runkel, Dr.-Ing. Andre Räupke, Eugen Shkura, Manuel Theisen, Dr.-Ing. Sara Trost, Christian Tückmantel, Fereshteh Vahabzad, Dr. Pang Wang, Dr.-Ing. Kirill Zilberberg und Florian Zimmermann.

Danken möchte ich außerdem meinen studentischen Hilfskräften sowie meinen Abschlussstudenten, die ich während meiner Zeit am Lehrstuhl betreuen durfte. Ihre fleißige Mitarbeit half mir bei meiner Forschungsarbeit.

Abstract

Metal halide perovskites are attracting increasing interest for optoelectronic applications, such as solar cells, photodetectors, light-emitting diodes, and lasers. Metal halide perovskites afford facile tuning of the bandgap and their processability from solution allows for cost effective, high throughput roll-to-roll production. Still, metal halide perovskite semiconductors face challenges like reproducibility, upscaling, lead toxicity, and long-term stability. Furthermore, thermally activated processes strongly influence both stability and performance. As a result, studying the thermal properties of halide perovskites has become increasingly important.

In this thesis, the heat transport in metal halide perovskite semiconductors is investigated using a scanning thermal microscope (SThM). The further development of the SThM is shown, which, in addition to the measurement of the thermal conductivity and topography, also provides simultaneously access to thermal diffusivity and volumetric heat capacity. This novel scanning probe technique uses the advantages of the 3ω-method in the frequency domain without extensive sample preparation, provides high spatial resolution, and is independent of the temperature of the material/device under test. Additionally, a brief and comprehensive insight into the preparation of metal halide perovskites in the form of thin films and single crystals is given. Thus, the thermal properties of device-relevant halide perovskite thin films can be compared to that of single crystals.

In general, halide perovskites typically provide ultra-low (< 1 $W \, (m \, K)^{-1}$) thermal conductivities, which makes experimental access challenging. Different perovskite compositions of the ABX_3 structures are investigated to determine the influence of the A-site cation and halide (X=I, Br, Cl) on the thermal properties. In addition to the compositional influence, the dimensionality of the perovskite structural networks is also considered, where the varied crystal structure directly impacts the heat transport via phonons. Since perovskite devices may easily reach elevated temperatures above specific phase transition temperatures of the respective perovskite, it is also crucial to generate insights into thermal properties across structural phase changes. The thermal characteristics in thermal conductivity and heat capacity show a remarkable behavior during phase transitions for highly oriented large crystalline $CsPbBr_3$ thin films. The results reported in this thesis provide important insights into how the ABX_3 perovskite structure composition, polymorphs, and individual phase transitions affect heat transport and material-specific thermal properties, that are critical for thermal management in perovskite semiconductor devices.

Contents

Abbreviations and Symbols

Abbreviations	Description
AC calorimetry	adiabatic calorimetry
AFM	atomic force microscope
ALD	atomic layer deposition
AVC	anti-solvent vapor-assisted crystallization
CD	direction of compression
CL	cathodoluminescence
DUT	device under test
DTA	differential thermal analysis
EBSD	electron backscatter diffraction
ECU	electronic control unit
EDX	energy-dispersive x-ray spectroscopy
ETL	electron transport layer
FDTR	frequency domain thermoreflectance
GIWAXS	grazing incidence wide angle x-ray scattering
HTL	hole transport layer
IR	infrared
ITC	inverse temperature crystallization
KPFM	Kelvin probe force microscopy
LASER	light amplification by stimulated emission of radiation
LED	light-emitting diode
LIA	lock-in amplifier
LO phonons	longitudinal optical phonons
MDS	molecular dynamics simulation
MHP	metal halide perovskite
OLED	organic light-emitting diode
pc-AFM	photo-conductive atomic force microscopy
PFM	piezoresponse force microscopy
PHP	planar hot pressing
PL	photoluminescence
POM	polarized optical microscopy
PV	photovoltaic
PVD	physical vapour deposition
QMB	quartz micro-balance
RBS	Rutherford backscattering spectrometry
R2R	roll to roll
SE	secondary electrons
SEM	scanning electron microscope
SThM	scanning thermal microscope
TEM	transmission electron microscopy
TDTR	time domain thermoreflectance
UV	ultraviolet
XRD	x-ray diffraction

chemical formula	Description
Ag	silver
Al_2O_3	aluminum oxide
$BaTiO_3$	barium titanate
BCP	bathocuproine
Bi	bismuth
$BiFeO_3$	bismuth ferrite
Br	bromine
C	carbon
$CaTiO_3$	calcium titanate
CBP	4,4′-bis(N-carbazolyl)-1,1′-biphenyl
CIGS	copper indium gallium (di)selenide
Cl	chloride
Cs	cesium
CZTS	copper zinc tin sulfide
CZTSe	copper zinc tin selenide
F8	poly(9,9-di-n-octylfluorenyl-2,7-diyl)
FA	formamidinium
GaAs	gallium arsenide
GBL	gamma-butyrolactone
I	iodine
ITO	indium tin oxide
$LiNbO_3$	lithium niobate
MA	methylammonium
MeOH	methanol
Pb	lead
PBD	2-(4-Biphenyl)-5-(4-tert -butylphenyl)-134-oxadiazole
$PbTiO_3$	lead titanate
PCBM	[6,6]-Phenyl-C61-butyric acid methyl ester
PEDOT:PSS	Poly(3,4-ethylenedioxythiophene):poly(styrene sulfonate)
PVK	poly(9-vinylcarbazole)
Si	silicon
Sn	tin
SOCP	self-organized conducting polymer
Spiro-OMeTAD	2,2′,7,7′-tetrakis(N,N-di-4-methoxyphenylamino)-9,9′spirobifluorene)
$SrTiO_3$	strontium titanate
TFB	poly(9,9-dioctylfluorene-alt-N-(4-sec-butylphenyl)-diphenylamine)
TPBI	2,2',2"-(1,3,5-Benzinetriyl)-tris(1-phenyl-1-H-benzimidazole)
TPD	N,N'-diphenyl-N,N'-bis(m-tolyl)-1,1'-biphenyl-4,4'-diamine

Symbols	Description	unit
A	area	m^2, cm^2, mm^2
a	thermal diffusivity	mm^2/s
α	thermal expansion coefficient	K^{-1}
c_{spec}	specific heat capacity	$J/(kg \cdot K)$
c_{vol}	volumetric heat capacity	$J/(m^3 \cdot K)$
E	elastic modulus	N/m^2
E_g	bandgap	eV
I	current	A
K	compression modulus	N/m^2
K_0	zero modified bessel function of second kind	
L	Lorenz number	$W\Omega/K^2$
l_{mfp}	mean free path	nm
$\overleftrightarrow{\lambda}$	thermal conductivity	$W/(m \cdot K)$
P	power	W
φ	angle	°
$\vec{\dot{q}}$	heat flux	W/m^2
R	resistance	Ω
rms	root mean square	
ρ	density	kg/m^3
S	Seebeck coefficient	V/K
σ	electrical conductivity	S/m
T	temperature	°C, K
U	voltage	V
v	velocity	m/s
ω	frequency	Hz, kHz
ζ	complex thermal wave number	1/nm

1. Introduction

Perovskites have been re-discovered for optoelectronic device applications in recent years. The number of publications on metal halide perovskites (MHPs) has increased tremendously, making them an integral part of materials science and engineering today. This material class is the first solution processed semiconductor that can compete with conventional semiconductors such as silicon or gallium arsenide in terms of performance and functionality. Due to their solution-process ability, perovskites represent a promising platform for low-cost roll-to-roll manufacturing. The possibility of realizing semi-transparent (opto)electronic components on flexible substrates also opens up a wide range of applications. The efficiency of perovskite-based solar cells on a laboratory scale has already reached 25.7% [1]. In addition, MHP materials, which also possess facile tunability of their band gaps, provide an excellent basis for multi-junction solar cells, that can overcome the fundamental efficiency limitations of single-junction devices [2]. Besides, MHP semiconductors also show impressive breakthroughs in light-emitting diodes (LEDs) and lasers [3–5]. Moreover, this family of materials also holds great promise for thermoelectric generators due to their remarkable low thermal conductivities [6].

However, perovskite-based devices still face challenges in terms of performance and stability. The thermal management of these devices and thus the thermal properties of MHPs play a crucial role here. The crystal structure is significantly influenced by temperature and temperature gradients. High thermal expansion coefficients have a significant effect on the stress [7–10], to which devices are subjected during operation, e.g. in the case of solar cells due to solar radiation [11,12]. More severely, it was found that even in an inert atmosphere, substantial decomposition effects already occur for methylammonium (MA) based perovskites below 100 °C [13]. Phase transition temperatures can easily be reached above room temperature (RT). For example, $MAPbI_3$ has a structural phase transition from tetragonal to cubic at around 52°C [14] and $CsPbCl_3$ is in the tetragonal phase at RT, whereas above 46.9 °C, it becomes cubic [15]. Thus, the crystalline phase and thermal expansion also influence electronic properties, such as carrier dynamics [16].

This thermal management is especially relevant for solar cells, LEDs, and the prospects for electric or continuous-wave perovskite lasers [17,18]. It is important to note that the thermal properties themselves strongly depend on temperature and the phase transitions may cause significant and abrupt changes in the crystalline structure. Therefore, the investigations on

thermal properties as a function of the crystalline phase is crucial, but also interesting for the individual devices. Thermal studies depending on the choice of cations and halide anions are also important for understanding heat transport in versatile MHP semiconductors. In this context, it is worth mentioning that the crystal network of the MHP can also vary, so different polymorphs/dimensions exist. Since these polymorphs are widely used in MHP devices, their thermal properties need to be investigated. In addition to the insights of the thermal conductivity measurements, thermal diffusivity and heat capacity studies are becoming more and more relevant for the heat dissipation design for the dynamic operation of MHP based devices.

Within this thesis, the current state of knowledge on the thermal properties of MHPs is briefly summarized in the next chapter. Besides fundamentals of MHPs, thermally activated processes leading to thermal stress and structural instability will be discussed. The heat transport mechanisms of this material class will be presented in detail to provide a basis for understanding the experimental investigations. The experimental data will be complemented by the results of theoretical works investigated by other groups. An essential component of this thesis is the measurement technique for determining the individual thermal properties, since the ultra-low thermal conductivities, low thermal diffusivities, and low volumetric heat capacities of MHPs pose a particular challenge. Chapter 3 describes the development of an enhanced scanning near-field thermal microscope (SThM) system and its operation to determine topography and thermal properties simultaneously. The fabrication of individual MHP thin films and single crystals will be described in the fourth chapter. Chapter 5 deals with determining the thermal properties of metal halide perovskites, first discussing the dependence on composition and then the dependence on the dimensionality of perovskites. After an introduction of phase transitions in general, Chapter 6 will present studies of the thermal behavior in the different structural phases of perovskites and during the phase transition itself. Chapter 7 summarizes this thesis's results and findings and gives an outlook on future topics.

Note: Parts of this thesis have been published in scientific journal articles or have been presented at conferences.

2. Fundamentals of heat dissipation in metal halide perovskite semiconductors

This chapter introduces the heat transport characteristics of metal halide perovskites (MHPs). The first section presents the structural concept of MHPs, their structural composition, the dimensionality of the perovskite structural networks, and associated optoelectronic properties. Thermo-elastic quantities of perovskites are discussed to motivate the need of heat transport investigations of MHPs performed in this work. In the third part, the heat transport within semiconductors and in particular metal halide perovskites is explained. Based on these explanations, the state of the field is presented with additional explanations of how the heat transport and the associated thermal properties of MHPs are determined. Finally, the most important findings of different research groups are summarized as a basis for the experimental work of this thesis.

2.1. Fundamentals of metal halide perovskite semiconductors

Perovskites were first described by Gustav Rose almost 200 years ago in 1839. The material described consisted of $CaTiO_3$ and was named after the mineralogist Lev Alekseyevich Perovski [19]. First, in general, perovskites gained attention with metal oxide perovskites like $BaTiO_3$, $PbTiO_3$, $SrTiO_3$, and $BiFeO_3$, which are used in ferroelectric, piezoelectric, dielectrics, and/or pyroelectric applications [20–22]. Optoelectronic applications, except for a few limited compositions such as $LiNbO_3$, $PbTiO_3$, and $BiFeO_3$ [20,23,24], do not find promising applications due to their wide bandgap (>2.5eV).

On the other hand, metal halide perovskite semiconductors are opening a vast world that has enabled numerous applications in optoelectronic devices (see **Figure 1**). The efficiency of perovskite-based solar cells has shown an enormous increase over the last few years, which is shown in the extract of the NREL chart [1]. The fact that the bandgap of perovskites is adaptable and can be used as a configurable part for tandem solar cells is another advantage of this material class. A combination of wide bandgap and narrow bandgap subsolar cells, along to cover the solar spectrum and lower thermalization losses, are keys to overcoming the Schockley-Queisser efficiency limit of single-junction solar cells [25].
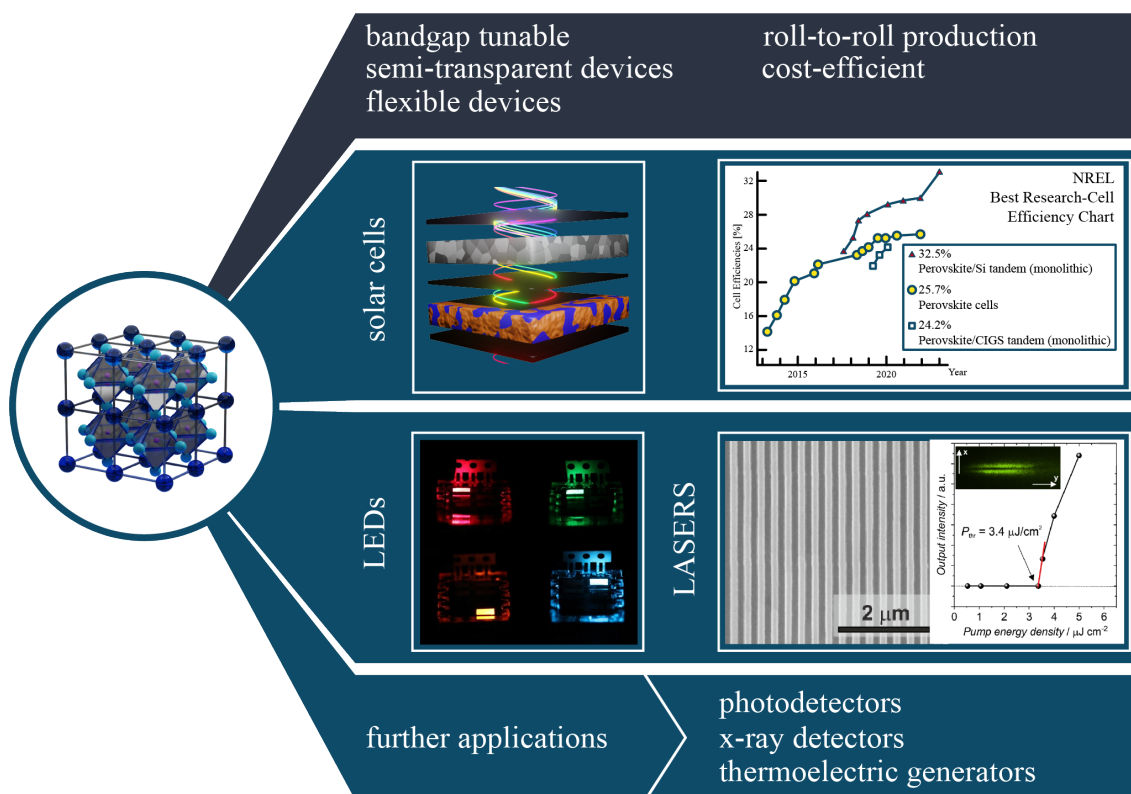
Figure 1: *The graphic shows an overview of the wide range of applications for metal halide perovskites. The focus is on optoelectronic devices, such as solar cells, LEDs, and lasers. Other applications include detectors and thermoelectric devices. Edited and based on* [1,26,27]*.*

Aside from optoelectronic devices, metal-halide perovskite semiconductors have also emerged as an attractive platform for thermoelectric generators [6]. Here, the reported ultra-low thermal conductivities of lead-halide perovskites may be advantageous for the thermoelectric generators. At the same time, for the vast majority of opto-electronic devices heat transfer may be an issue and thermal management requires particular attention.

The well-known representative of the perovskite class is the ABX_3 composition, in which the B-cation is coordinated octahedrally by X-anions and the A-cation fills the cuboctahedral voids, compensating for the negative charge. Metal halide perovskites adopt the structure composed of a three-dimensional network of corner-sharing BX_6 octahedra, where the B atom is typically a group 14 metal cation (typically tin Sn^{2+} or lead Pb^{2+}) and X is chlorine (Cl^-), bromine (Br^-), iodine (I^-), or a mixture of them. On the A-site, cesium (symbol: Cs^+) or organic cations, such as Methylammonium (symbol: $CH_3NH_3^+$ (MA^+)) and formamidinium (symbol: $NH_2HCNH_2^+$ (FA^+)), can be used to balance the total charge and stabilize the lattice [28]. The following **Figure 2** illustrates a typical metal halide perovskite structure.
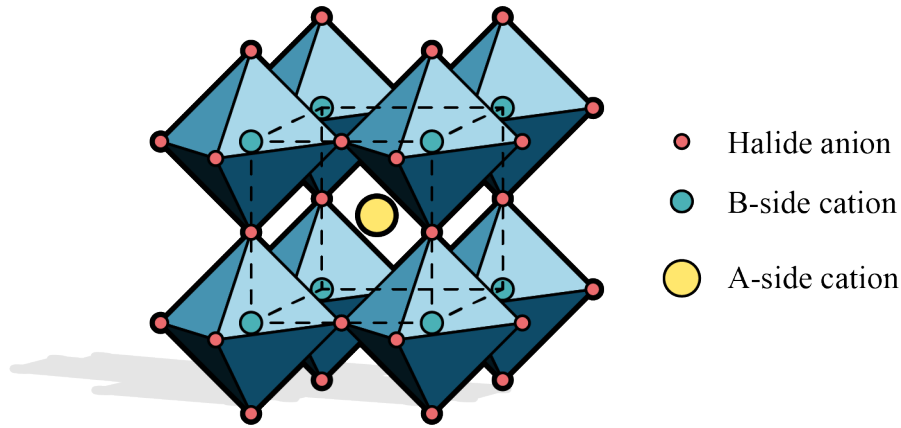
Figure 2: *Schematic illustration of a three-dimensional ABX_3 perovskite structure. Here, the A-site cation (yellow) is surrounded by BX_6 octahedra (B-site cation turquoise and halide anion red). Edited and based on* [29].

The metal halide composition determines the bandgap E_g in the range of approximately 1.2 to 3.6 eV for lead and tin compounds (see **Figure 3**) [30]. This shows a great variability for matching to individual devices. For example, a bandgap of around 1.3 eV is optimal for single absorber solar cells, while larger bandgaps are interesting for tandem-based solar cells to optimize the overlap with the solar spectrum [2,31].
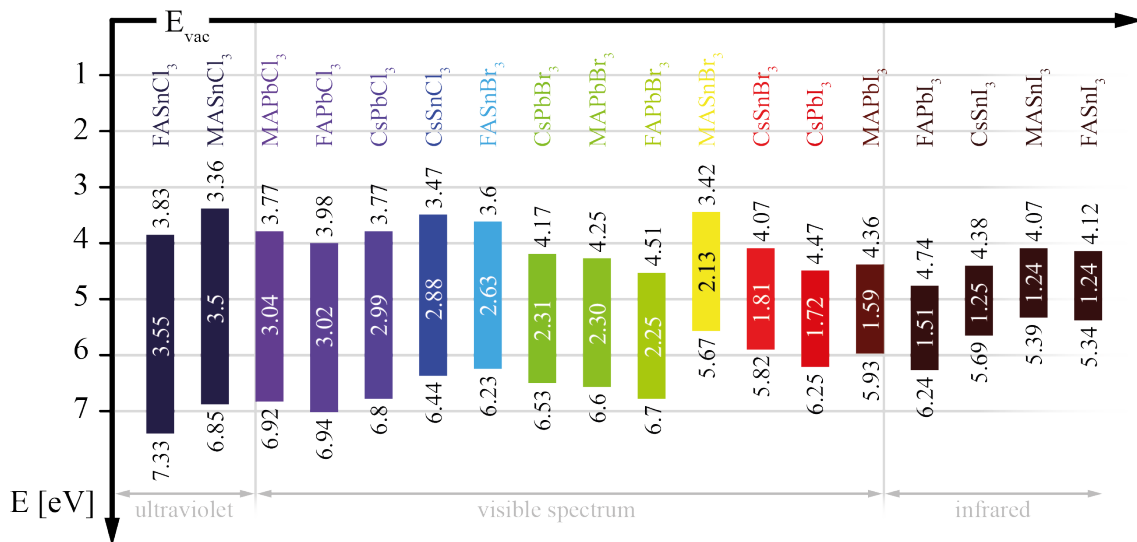
Figure 3: *The graph shows 18 different metal halide perovskite compositions and represents the change in band gap energy and electron affinity. In addition, the colors of the individual perovskites shown indicate the color of the light they emit based on their band gap energy and are sorted in descending order of band gap energy. Edited and based on* [30].

The changes in band gap for ABX_3 compounds are well characterized by Tao et al. [30] and offer the advantage that the metal halide perovskites can vary their band gap energy by composition [28,32,33].

As can be seen from **Figure 3**, it is mainly the halide anion and B-site cations that influence E_g and electron affinity, whereas only a slight change are caused by a variation of the A-site cations. However, the A-site cation affects the structural stability of the metal halide perovskites. Thus, the change from organic A-site cations to inorganic A-site cations such as Cs or even a mixture of a triple cation or quadruple cation has proven to be a promising concept for increasing the structural stability of metal halide perovskites [34–36]. For example, in contrast to organic-inorganic hybrid lead halide perovskites (such as $MAPbX_3$ and $FAPbX_3$), all-inorganic $CsPbX_3$ perovskite semiconductors show better thermal stability, which results in higher temperatures for the onset of thermal decomposition. Regarding commercialization and sustainability aspects, the choice of the B-site cation is also crucial. In addition to Sn-based lead-free metal halide perovskites, the so-called double perovskites $A_2BB'X_6$, heterovalent substitutions of Pb^{2+} by silver Ag^+ and bismuth Bi^{3+}, for example, are also of great interest [37,38]. Note, when preparing a metal halide perovskite with the composition required for a particular application, structural stability should also be considered.

Different polymorphs/dimensionalities of metal halide perovskites are also already used in LEDs, solar cells, lasers, and photodetectors due to their improved optoelectronic properties and stability [39–41]. The two-dimensional (2D) and zero-dimensional (0D) perovskite structures of the form $A_\alpha B_\beta X_\gamma$ (see **Figure 4**) expand and improve the range of applications through their physical and chemical properties [42,43]. For example, Cs_4PbBr_6 exhibits vacancy-assisted photoluminescence [41,44]. Note, these low-dimensional networks share the same compositional elements and PbX_6 octahedra, but show different octahedra connectivity features [41,44,45]. Some amounts of 0D or 2D polymorphs are frequently used to improve the efficiency and stability of perovskite based devices [42,43,46–48].

zero-dimensional (0D)
perovskite structure

two-dimensional (2D)
perovskite structure

three-dimensional (3D)
perovskite structure

A_4BX_6

AB_2X_5

ABX_3
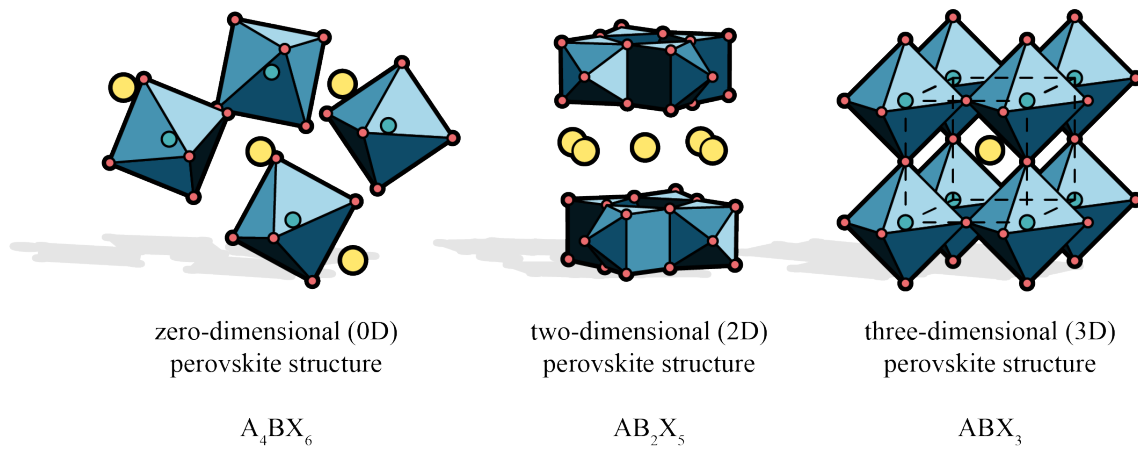
Figure 4: *Schematic representation of different polymorphic structural dimensionalities of perovskite structures. Zero-dimensional, two-dimensional, and three-dimensional perovskite networks with the corresponding chemical structural formulas are shown. Edited and based on* [49,50].

2.2. Thermo-elastic quantities of perovskites

For all polymorphs, performance and operational stability are strongly influenced by thermally activated processes, which are caused, for example, under extreme operating conditions or under intense solar radiation. Since thermal stress and structural instability lead to the degradation of all perovskites [51], the determination of the thermo-elastic quantities of perovskites depending on the temperature is focused on in the following.

The melting temperature of all inorganic $CsPbI_3$ was determined in 1992 from the phase diagram obtained by differential thermal analysis (DTA) experiments to be higher than 480 °C at atmospheric pressure [52]. Somewhat later, subsequent studies of crystal structures exhibited that $CsPbBr_3$ melts at 567 °C and crystallizes from the melt at 514 °C [53]. At the same time, it could be demonstrated that melting points increase with decreasing atomic number of the halide, i.e. for $CsPbCl_3$ up to 615 °C [54]. All these compounds melt congruently as confirmed in these experiments. Hence, large $CsPbBr_3$ crystals could be produced from the melt at high temperatures (600 °C) using the vertical Bridgman method [53]. These single crystals have been proposed as promising candidates for X-ray and gamma-ray detection,[55–57] since the first investigations on these direct semiconductors showed that most of their properties are comparable to, or even exceed, those of commercial state-of-the-art detector materials.

In this context it must be considered that the endothermic DTA peaks for the decomposition pathways of organic-inorganic hybrid $MAPbX_3$ compounds are at low temperatures [58]. However, although various decomposition reactions have been proposed [10,58,59]:

$$MAPbX_3 \rightarrow PbX_2 + MA + HX \quad (1)$$
$$MAPbX_3 \rightarrow PbX_2 + MAX \quad (2)$$

During the thermal decomposition of hybrid perovskites typically solid lead halides remain. In DTA measurements the melting points of hybrid and all-inorganic perovskites are thus quite often linked to that of PbX_2. Note that a distinction must be made between melting and decomposition, which can be depicted more accurately from thermogravimetric analyses; see **Figure 5** for an example [60].
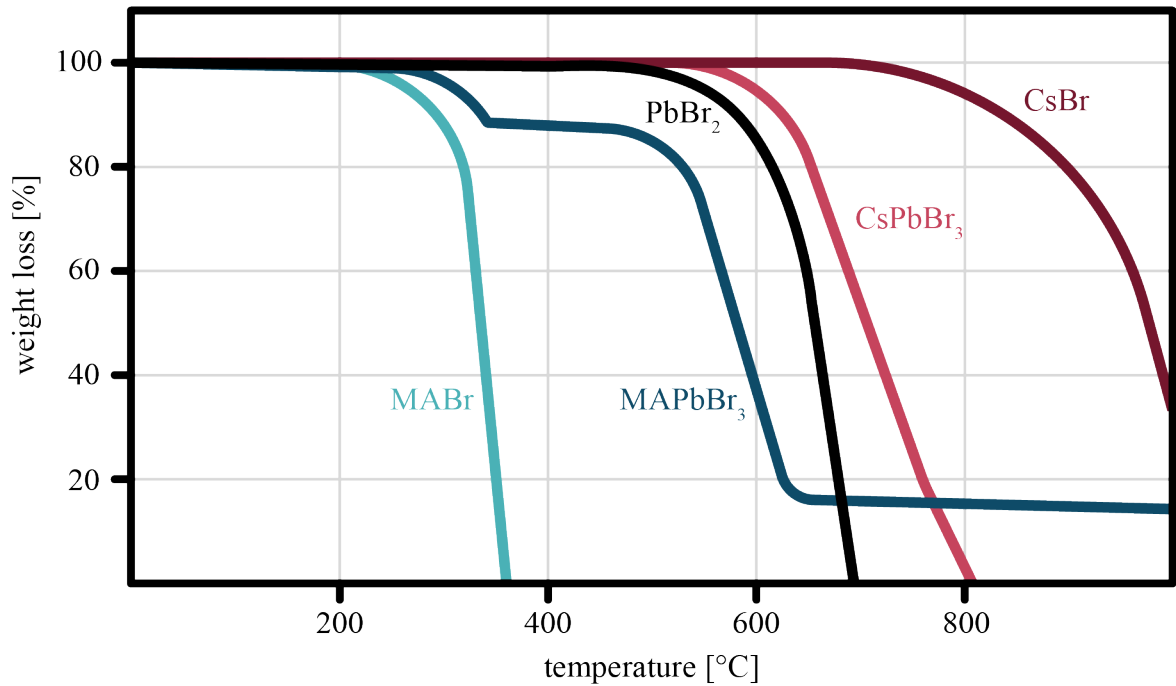
Figure 5: *Thermogravimetric analyses of MABr, MAPbBr₃, PbBr₂, CsPbBr₃, and CsBr, showing the higher thermal stability of the inorganic perovskites compared to the hybrid organic-inorganic perovskites. Edited and based on* [60].

As for the evaporation or decomposition of $CsPbBr_3$, CsBr is more stable than $PbBr_2$, which evaporates first as shown in the **Figure 5**. The small temperature shift between $PbBr_2$ and $CsPbBr_3$ can be explained by the slightly higher stability of the perovskite compound. For hybrid perovskites, it must be considered that all the methylammonium halides evaporates at lower temperatures (for instance MAI: >190 °C [59]). Although methylammonium halides are mostly even reported to be over 200 °C [58] for $MAPbX_3$, it is still a challenge to have long-term stabilities at 85 °C (representing an elevated temperature on a roof on a hot summer day) required according to the International Standards (IEC 61646 climatic chamber tests) of solar cells [13]. Thus, the thermal activation energies (E_a) for the decomposition reactions have to be considered [61]. From DTAs Ea's of 68 ± 2 kJ mol^{-1}, 60 ± 10 kJ mol^{-1}, and 80 ± 20 kJ mol^{-1} have been reported for $MAPbCl_3$, $MAPbBr_3$, and $MAPbI_3$, respectively [58]. Somewhat larger E_a values have been determined by the first mass loss step observed in thermogravimetric analyses [62]. Higher values have been found for lighter halides in MA and FA based compound calculations [63], summarized in following table:

Table 1: *Detected degradation activation energies E_a and thermal expansion coefficients $\alpha(T)$ of common metal halide perovskites above RT.*

Perovskite	E_a [kJ mol^{-1}]	α [x10^{-4} K^{-1}]
MAPbI$_3$	93 ± 8 [62] 83 [63]	$\alpha_{tet.}$ (001): −5.1, $\alpha_{cub.}$ (001): 4.6 [14] $\alpha_{tet.}$ (001): −1.06, $\alpha_{tet.}$ (100): 1.32 $\alpha_{cub.}$ (100): 0.48 [64] $\alpha_{tet.}$ (100): 0.58, $\alpha_{cub.}$ (100): 0.39 [65] $\alpha_{tet.}$: 0.90 [66]
MAPbBr$_3$	98 ± 4 [62] 365 [63]	$\alpha_{cub.}$ (100): 0.33 [67] $\alpha_{cub.}$ (100): 0.32 [65] $\alpha_{cub.}$: 0.67 [66]
MAPbCl$_3$	400 [63]	$\alpha_{cub.}$ (100): 0.29 [65]
CsPbI$_3$	650 ± 90 [62]	$\alpha_{ort.}$: 0.39, $\alpha_{cub.}$: 0.39 [68] $\alpha_{ort.}$ (001): 0.22 $\alpha_{ort.}$ (110): 0.22 $\alpha_{tet.}$ (001): −0.52 $\alpha_{cub.}$ (100): 0.40 [69]
CsPbBr$_3$		$\alpha_{ort.}$: 0.38, $\alpha_{tet.}$: 0.65, $\alpha_{cub.}$: 0.26 [70] $\alpha_{ort.}$ (101): 0.38 [71,72]
CsPbCl$_3$		$\alpha_{mon.}$: 0.56, $\alpha_{ort.}$: 0.50, $\alpha_{tet.}$: 1.27 $\alpha_{cub.}$: 0.30 [12] $\alpha_{cub.}$: 0.22@T = 85 °C [14] $\alpha_{mon.}$: 0.42, $\alpha_{ort.}$: 0.38, $\alpha_{tet.}$: 0.78 $\alpha_{cub.}$: 0.29 [70]
FAPbI$_3$	115 ± 3 [62] 108 [63]	$\alpha_{tet.}$ (100): 0.77 $\alpha_{tet.}$ (010): 0.77 $\alpha_{tet.}$ (001): 0.49 [73] $\alpha_{ort.}$: 0.39 [66]
FAPbBr$_3$	133 ± 1 [62] 332 [63]	$\alpha_{cub.}$: 0.89 [66]

Details of the chemical, structural, morphological, and optical stability of the MHPs and the impact of thermal stress on the charge transport layers of methylammonium lead halide-based perovskites are available elsewhere [51]. Due to the different chemical nature of the cesium and methylammonium cations, the halides CsPbX$_3$ and MAPbX$_3$ exhibit different stabilities. The enthalpy of formation is slightly more negative for CsPbX$_3$ compared to MAPbX$_3$ with respect to the enthalpies of formation of binary halides [74]. Also, it has long been known that perovskites have phase transitions at elevated temperatures up to 85 °C [15,75].

2.3. Thermal mechanical interactions in perovskites

Investigations of the elastic constants and thermal expansion of $CsPbCl_3$ were provided by Hirotsu and Suzuki in 1978 [12]. They found phase transitions for $CsPbCl_3$ single crystals from monoclinic to orthorhombic to tetragonal and finally to cubic [11,76]. A notable discontinuity in the thermal expansion coefficient $\Delta l/l$ of $16.7 \cdot 10^{-4}$ as detected using a conventional dilatometer was attributed to a first order transition from the tetragonal to cubic phase. No signs of discontinuity of $\Delta l/l(T)$ were found at the other phase transitions, indicating that they are second order transitions [12]. On the contrary, an earlier report claimed the transition from monoclinic to orthorhombic to be of first order [11,76]. One year later, some nonlinearities were found for the lattice thermal expansion up to 85°C of $CsPbCl_3$, with $\alpha(T)_{CsPbCl_3}$ being quadratically dependent on T in the cubic phase indicating a second order transition [77]. This is because the thermal expansion is related to the specific heat capacity of the material, which diverges near a second-order phase transition. However, although the change in $\Delta l/l$ was determined to be less than $3.1 \cdot 10^{-4}$ in these experiments from the tetragonal to cubic phases of $CsPbCl_3$, a higher change in $\Delta l/l$ ($5.8 \cdot 10^{-4}$) was found in the case of $CsPbBr_3$ [70].

Large negative thermal expansion coefficients have been observed in the tetragonal phase for yellow and black $CsPbI_3$ (see **Figure 6**). The negative thermal expansion coefficients complicates the application in optoelectronic devices because only the $CsPbI_3$ perovskite black phase is optically active. Due to their huge absolute values of thermal expansion coefficients, perovskite films fabricated by existing methods are strained, and the strain is caused by the different coefficients of thermal expansion of the perovskite and substrate during thermal annealing processes as well as due to the growth process itself. Strain has been shown to accelerate the degradation of perovskite films under illumination, which can be explained by increased ion-migration in these films [78].
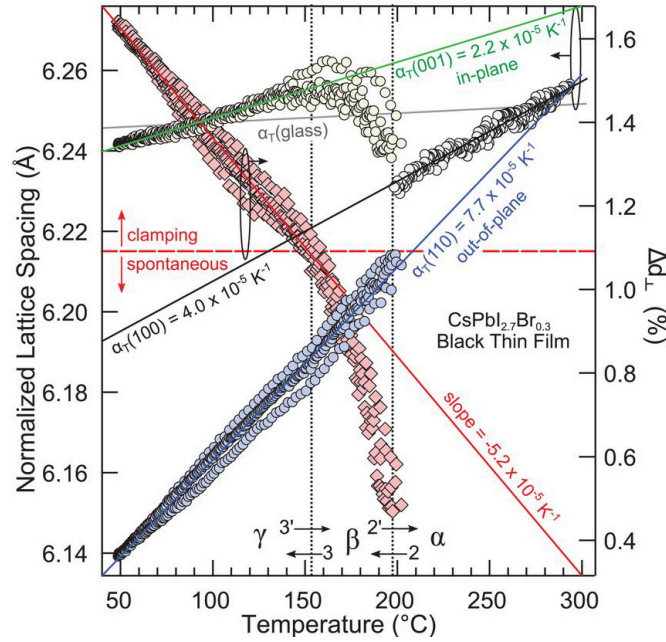
Figure 6: *Structural phase kinetics of strained α-, β-, and γ-CsPbI₃ perovskite thin films* [69].

However, for the sake of completeness, it should also be mentioned that lower coefficients of thermal expansion were measured in thin films compared to single crystals in the (100)-direction, $\alpha_{a-tet.} = 0.58 \cdot 10^{-4} \, K^{-1}$ and $\alpha_{a-cub.} = 0.39 \cdot 10^{-4} \, K^{-1}$ [65]. It could also be demonstrated that the coefficient of thermal expansion of MAPbI₃ is larger than that of MAPbBr₃ and MAPbCl₃ ($0.32 \cdot 10^{-4} \, K^{-1}$ and $0.29 \cdot 10^{-4} \, K^{-1}$, respectively). In addition, the coefficients of thermal expansion of these hybrid perovskites are larger than those of related Cs–Pb based all-inorganic perovskites.
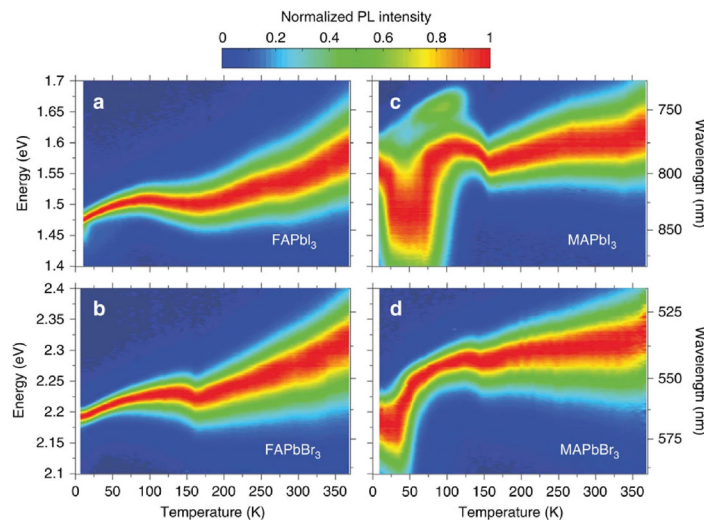
Figure 7: *Temperature dependence of normalized steady-state PL on (a) FAPbI₃, (b) FAPbBr₃, (c) MAPbI₃, and (d) MAPbBr₃* [79].

The first in-depth analysis of charge-carrier–phonon interactions in hybrid lead halide perovskites was carried out on $FAPbI_3$, $FAPbBr_3$, $MAPbI_3$, and $MAPbBr_3$ [79]. For FA-based perovskites it was already found that the Fröhlich interaction between charge carriers and longitudinal optical phonons (LO phonons) is the dominant contribution to the predominantly homogeneous broadening of the PL line at room temperature (see **Figure 7**). The Fröhlich interaction for bromide perovskites is larger than that for iodide perovskites, providing a link between composition and electron–phonon scattering that fundamentally limits the mobilities of the charge carriers. In addition to spectral changes, the lattice strain causes nonradiative losses in halide perovskites [80], which has in addition been attributed to the locally induced crystal misorientation [81]. The remaining nanoscale strain also reduces the stability in cesium lead-bromide perovskites and shifts the local luminescence spectrum [82]. In contradiction to these studies, it has been reported previously that light-induced lattice expansion leads to high-efficiency perovskite solar cells [83]. While the authors of these studies claim to exclude heat-induced lattice expansion, it has been shown that the lattice expansion mechanism matches the heat-induced thermal expansion during illumination [84]. The properties of phonons are crucial for the understanding of not only charge transport in the form of electron–phonon interactions in polar semiconductors such as halide perovskites, but also for heat transport in functional materials. Phonon–phonon scattering plays a decisive role in determining acoustic phonon transport and thus the thermal conductivity of halide perovskites.

In a wide range of these organic–inorganic and all-inorganic perovskite applications, the acquisition of the stability under elevated temperatures and long-term light soaking as well as under real-world operating conditions has become more and more important [85,86]. Since temperature and temperature gradients induce thermal stress and structural instability, the following sections provide an overview of the heat dissipation in metal-halide perovskites and the experimental techniques used so far to assess thermal conductivities, thermal diffusivities, and heat capacities. The experimental data will be complemented by the results of theoretical works.

2.4. Heat dissipation in metal halide perovskite semiconductors

The fundamentals of heat transport of metal halide perovskites are explained in the following section. To this end, the topic is first introduced by explaining general terms and heat transport in solids, followed by a specific discussion of heat transport and the thermal properties of perovskites. Based on this, an overview of the state of field is given with respect to the thermal properties determined by simulations as well as experimental approaches.

2.4.1. Introduction into heat dissipation in metal halide perovskite semiconductors

Heat transport can be divided into four categories, advection, conduction or diffusion, convection, and radiation. In the following discussion, we deal exclusively with conduction/diffusion. Here, an exchange of thermal energy takes place with a gradient from the hotter to the cooler region until thermal equilibrium is reached. The resulting heat flux $\vec{q}(\vec{r}, t)$ is classically described by the Fourier law, where in general $T(\vec{r}, t)$ is a given temperature distribution and $\overleftrightarrow{\lambda}(\vec{r}, t)$ is the tensor of thermal conductivity [87–90]:

$$\vec{q}(\vec{r}, t) = -\overleftrightarrow{\lambda}(\vec{r}, t) \cdot \operatorname{grad} T(\vec{r}, t) \tag{3}$$

Note, material specific parameters like $\overleftrightarrow{\lambda}(\vec{r}, t)$ are also time-dependent since they depend on $T(\vec{r}, t)$. For steady state conditions, the thermal conductivity can be directly determined, if the absorbed heating power in the sample is known. However, in the case of dynamic (transient) heat transports, the volumetric heat capacity $c_{vol.}(\vec{r}, t)$, given by the product of the density ρ and the specific heat c_{spec} of the material, must be considered and the heat flow is described by the general equation of heat conduction:

$$c_{vol.}(\vec{r}, t)\frac{\partial T(\vec{r}, t)}{\partial t} = \frac{\partial}{\partial x}\left(\lambda_x(\vec{r}, t)\frac{T(\vec{r}, t)}{\partial x}\right) + \frac{\partial}{\partial y}\left(\lambda_y(\vec{r}, t)\frac{T(\vec{r}, t)}{\partial y}\right) + \frac{\partial}{\partial z}\left(\lambda_z(\vec{r}, t)\frac{T(\vec{r}, t)}{\partial z}\right) + \dot{q}_E(\vec{r}, t) \tag{4}$$

where $\dot{q}_E(\vec{r}, t)$ indicates the amount of heat generated per unit time and unit volume [90]. For homogeneous and isotropic materials, eq 4 can be simplified to

$$\frac{\partial T(\vec{r},t)}{\partial t} = a(\vec{r},t) \cdot \Delta T(\vec{r},t) \frac{\dot{q}_E(\vec{r},t)}{c_{vol.}(\vec{r},t)} \tag{5}$$

whereby $a(\vec{r},t) = \frac{\lambda(\vec{r},t)}{c_{vol.}(\vec{r},t)}$ denotes the thermal diffusivity of the material, i.e., the ability of a material to conduct thermal energy relative to its ability to store thermal energy. The heat transport based on the free carrier gas model is discussed in the following to describe the thermal conductivity.

Using the Wiedemann-Franz law [91], the thermal conductivity in metals is correlated to the electrical conductivity $\sigma(\vec{r},t)$ due to the heat transport of electrons [92–95]. Thus, the relationship can be explained by:

$$\frac{\lambda(\vec{r},t)}{\sigma(\vec{r},t)} = L \cdot T(\vec{r},t), \tag{6}$$

which coupled and introduces the empirical Lorenz number L [96]. The relationship between $\lambda(\vec{r},t)$ and $\sigma(\vec{r},t)$ shows that the transport mechanism of both electrical transport of electrons and heat is the same and can therefore be described by the electron gas [92,97]. In general, however, heat transport occurs via both electrons and lattice vibrations/phonons, so thermal conductivity can be described as the sum:

$$\lambda(\vec{r},t) = \lambda_{electron}(\vec{r},t) + \lambda_{phonon}(\vec{r},t) \tag{7}$$

In the case of heat transport in perovskite semiconductors, the thermal conductivity depends predominantly on the phonon kinetic gas theory according to Peter Debye [88,98]:

$$\lambda_{phonon}(\vec{r},t) = \frac{1}{3} c_{phonon}(\vec{r},t) \cdot v_{phonon}(\vec{r},t) \cdot l_{mfp-phonon}(\vec{r},t) \tag{8}$$

The thermal conductivity $\lambda_{phonon}(\vec{r},t)$ is given by the volumetric phonon heat capacity $c_{phonon}(\vec{r},t)$, the average group velocity $v_{phonon}(\vec{r},t)$, and the temperature-dependent average phonon mean-free path $l_{mfp-phonon}(\vec{r},t)$ [96,99]. The mean free path of the phonons is determined by scattering processes and interactions within the crystal structure. These include geometric scattering and phonon-phonon interactions. Hence, measurement series and simulations of the thermal conductivity of MHPs, where the composition of the perovskites has been varied, and publications show a similar motif and describe that the ultra-low thermal conductivity of metal halide perovskites is due to the properties of their phonons [95,96,100,101].

Due to the crystalline structure, the lattice vibrations of perovskites have three degrees of freedom, which can be divided into acoustic and optical modes [102]. These modes can be further subdivided into the transverse and longitudinal configurations. In the transverse phonons, the lattice vibration is perpendicular to the direction of propagation. For longitudinal phonons, on the other hand, the oscillation vector is parallel to the direction of propagation.

Theoretical considerations and simulations have indicated that the strong interaction between the rotation of the A-site cation and the low-frequency phonons of the PbX_6 cage may result in ultra-low thermal conductivities for hybrid organic – inorganic MHPs [103]. Specifically, this means that the motions of the cations and the vibrations of the crystal lattice reduce the material's ability to conduct heat. Therefore, MHP materials that have this strong interaction between the rotation of the cations and the phonons of the crystal lattice can have extremely low thermal conductivity. Moreover, in the case of all inorganic metal halide perovskites, the Cs atoms used are located in an oversized cage of the perovskite structure and form a weak chemical bond with the halogen atoms [104]. The weak chemical bonds lead to a dislocation of the inorganic A site cation and, together with the distortion of the octahedra, to a highly dynamic structure in the three-dimensional perovskite structure. This results in a low Debye temperature and a low phonon velocity according to Xie et al.[104]. The Debye temperature is defined as the temperature at which all normal vibrational modes of a crystal are excited simultaneously and reach a characteristic frequency. It is an important quantity in solid state physics and is related to the specific heat capacity and other thermodynamic properties of the crystal. According to the Debye temperature, elastic properties are correlated with thermodynamic properties, such as phonons, thermal expansion, thermal conductivity, and specific heat. In addition, Xie et al. found out, that the Cs atom behaves like a heavy cage rattler and results in a coupling of low-frequency optical phonons and the acoustic phonons. Which results in a low lattice thermal conductivity in the all-inorganic perovskite when phonon resonance scattering occurs on heat-carrying phonons within the perovskite. [104].

In the following the state of the field in the determination of the thermal properties of metal halide perovskites will be presented, divided into two categories: theoretical and experimental methods.

2.4.2. Molecular dynamic calculations of heat dissipation in metal halide perovskite semiconductors

In this section, an overview of the state of the field in molecular dynamic calculations of heat dissipation in metal halide perovskite semiconductors is given, providing and briefly describing the procedure to which this theoretical work relates. Molecular dynamics calculations from our review paper [100] are briefly summarized, as they provide the phonon dispersion which is essential for the description of heat dissipation in the crystalline structure and the dimensionality given by its composition $A_xB_yX_z$ in these perovskite semiconductor types.

For MAPbI$_3$ in all its phases (orthorhombic, tetragonal, cubic), it was found via molecular dynamics simulations by the Lin et al. group that the thermal conductivity λ is 0.31 W $(m\,K)^{-1}$ at room temperature [105]. Such ultra-low thermal conductivity, indicated by a result of the enhanced phonon-phonon scattering from highly overlapped phonon branches, hints to short phonon lifetimes < 100 ps and consequently short phonon mean-free paths < 10 nm. The low elastic stiffness of MAPbI$_3$ also predicts low group velocities [105]. Related to another work, a very low thermal conductivity of 0.59 W $(m\,K)^{-1}$ was found in the tetragonal phase at room temperature of MAPbI$_3$, attributed to the low group velocity of acoustic phonons due to the low elastic stiffness of MAPbI$_3$, whereas a much higher thermal conductivity was predicted for the pseudo-cubic phase (1.80 W $(m\,K)^{-1}$ at 57 °C)[106].

Caddeo et al. studied the influence of the A-site cation on thermal transport and attributed the low thermal conductivity of the lead-based perovskites to the low sound velocity of the PbX lattice [107]. It was found that the thermal conductivity value doubled when the organic A-site cations retained only the translational motion. This contrasts with reports from the group of Hata et al. using molecular dynamics simulations [103]. The study of the phonon band structures indicates that coupled translational and rotational motions of the A-site cation interact with the PbX$_6$ cages, suppressing phonon transport in MHPs. This was also shown by the calculations from [108] and confirms that the scattering between the rotational modes of the MA cation and the low frequency phonon modes is the reason for the low thermal conductivity of hybrid perovskites.

Coupled translational and rotational motions of MA were found to interact with the PbI octahedra and afford couplings between the isolated lattice vibrations, which hampers the phonon transport in MAPbI$_3$.

Further MDS shows that the A-site component of two-dimensional metal halide perovskites induces a reduction of the stiffness and sound velocities along with giving rise to vibrational modes in the 5–15 THz range that are absent in the three-dimensional counterparts [109]. The measured MHP films with weak van der Waals interactions between the organic and inorganic constituents (that confines the inorganic layers in 2D) posses ultra-low thermal conductivities in the range of 0.10 to 0.19 W $(m\,K)^{-1}$ depending on the organic cation arrangement [109].

Thermal transport investigations of perovskite alloys, which have been successfully developed to design various layered structures, [110,111] have been performed rarely [112–114]. The first inspections described in the publications of heat accumulations and gradients in transparent front electrode and back electrode materials are promising for the higher thermal stabilities of these devices since they also take the heat dissipation in air into account.

Note that dynamical heat transport analyses for MHPs have not been carried out so far. Accordingly, their experimental thermal property studies for reliable dynamic device operation will be considered in addition in the following.

2.4.3. Experimental determination of thermal properties in metal halide perovskite semiconductors

The content and the corresponding results from the status of the field are briefly summarized and the individual methods are explained. The measurement methods are fundamentally based on Fourier's law (see equation (3)). In all these methods, the material under investigation is exposed to a heat source either at the surface or in the volume. The heat flux within thin polycrystalline films and single crystal bulk samples is classically described as diffusive transport for a given temperature distribution. The applied measurement techniques used to determine the heat transport of metal halide perovskites can be divided into two categories: steady-state and transient techniques.

The first thermo-mechanical studies on inorganic $CsPbCl_3$ and $CsPbBr_3$ perovskites were performed in the 1970s to understand the phase transitions of these materials [12,76,115,116]. But the corresponding specific heat c_{spec} and thermal diffusivity a values of the different phases were obtained in transient measurements on single crystals much later [117]. In addition, thermal conductivity studies have been carried out for all-inorganic halide perovskite nanowires, $CsPbI_3$ and $CsPbBr_3$ [118,119]. The authors generally concluded that nanostructures or crystal grains with dimensions smaller than 100 nm significantly reduce the thermal conductivity because phonons have a mean-free path on the same order. Thus, somewhat higher thermal conductivities are reported for $CsPbBr_3$ single crystals (0.46 W $(m\,K)^{-1}$) [95] in comparison to nanowires (0.36 W $(m\,K)^{-1}$) [119].

The specific heat capacities of $MAPbX_3$ (X = I, Br, and Cl) perovskites were studied by Onoda-Yamamuro et al. in 1990 to be 19.0 J $(K\,mol)^{-1}$, 8.2 J $(K\,mol)^{-1}$, and 10.0 J $(K\,mol)^{-1}$ at room temperature for X = I, Br, and Cl, respectively [120]. Upon heating the $MAPbI_3$ samples above room temperature, a tetragonal to pseudo-cubic polymorph transition (57 °C) was observed that led to a reduction of c_{spec} to 9.7 J $(K\,mol)^{-1}$.

Pisoni et al. performed the first thermal conductivity measurements of $MAPbI_3$ for temperatures below room temperature [121]. The analysis was performed by a steady state bar technique. The room temperature thermal conductivity λ was determined to be 0.5 W $(m\,K)^{-1}$ and 0.3 W $(m\,K)^{-1}$ for a single crystal and a polycrystalline sample, respectively. The schematic of a thermal resistivity measurement setup in a standard four-point configuration is shown in **Figure 8**. An electrical heater, where the heat flux is equal to the electrical power, is connected to a sample, represented by the red rectangle, using epoxy. The sample is connected to a calibrated

reference material, which is glued to a heat sink for heat dissipation. The given temperature distribution is obtained using differential thermocouples placed on the sample and reference. This common technique was the very first one introduced to determine the thermal conductivity of materials and has been improved successively [122].
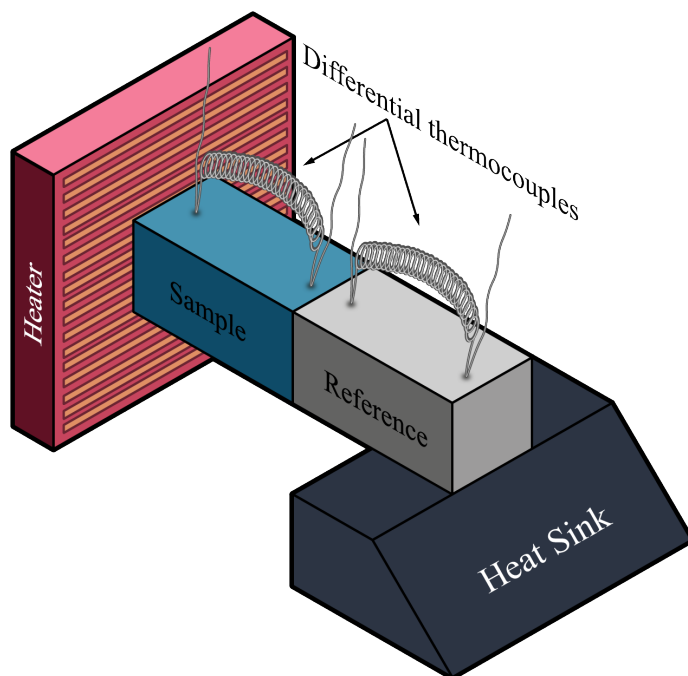
Figure 8: *Schematic of a thermal resistivity measurement setup in a standard four-point configuration. Edited and based on* [121].

The same thermal conductivity, as already published by Pisoni et al. for MAPbI$_3$, was found for a polycrystalline MAPbI$_3$ sample when measuring the effect of the methylammonium ion on phonon scattering by a longitudinal steady state technique in addition to calculations from a Debye model [123]. The low thermal conductivity of the MAPbI$_3$ single crystal was mainly attributed to the rotational motion of the MA cations [103] and has attracted intense attention due to its possible thermoelectric applications [124]. A high Seebeck coefficient S of 0.82 mV $(K)^{-1}$, [125] a decent charge carrier mobility in the range of 5–10 cm^2 $(V\,s)^{-1}$ for electrons and 1–5 cm^2 $(V\,s)^{-1}$ for holes, [126] and a high carrier diffusion length > 1 μm [127] were reported. The thermal conductivity of a MAPbI$_3$ perovskite was also evaluated using laser flash systems. Values of around 0.30–0.42 W $(m\,K)^{-1}$ were observed for a single crystal in the temperature range of room temperature to 150 °C [128]. Similar values were found for films using the time-domain thermo-reflectance (TDTR) method [129]. In striking contrast to all other reports, an unusually high thermal conductivity of densely packed MAPbI$_3$ films of 11.2 ± 0.8 W $(m\,K)^{-1}$ at room temperature was claimed by Chen et al. [130].

A review of other commonly used differential scanning calorimetry techniques is given by Gill et al [131]. A non-contact optical flash method was already established in 1961 [132] ,which is widely used in commercial thermal conductivity measurement systems. Its application to the study of microelectronic materials by the detection of thermal waves through changes in their optical reflectance was primarily demonstrated in 1985 [133]. The initial thermal diffusivity measurements of thin films by means of an AC calorimetric method were performed in the same year [134]. Like these analyses, a modulated thermo-reflectance microscopy technique (shown in **Figure 9**) has recently been successfully applied for measurements of the thermal conductivity and the thermal diffusivity in mixed-cation perovskites [135].
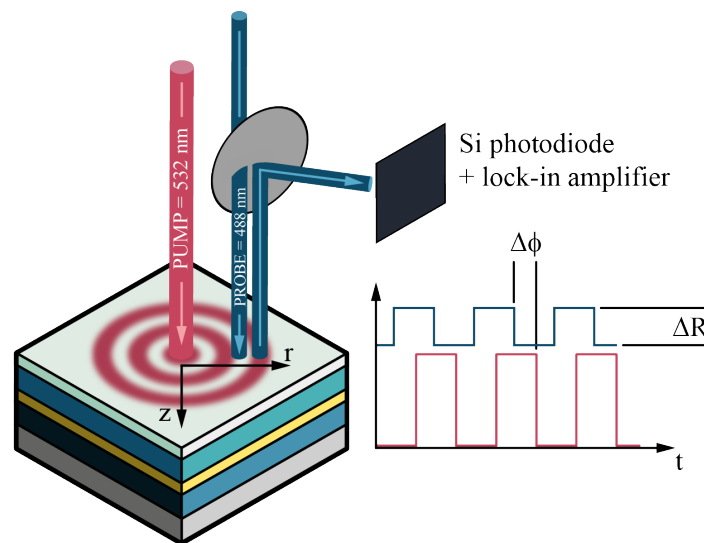
Figure 9: *Principle of a modulated photoreflectance setup. Edited and based on* [135].

A modulated pump beam (532 nm) is focused onto a sample's surface to provide a modulated local heat source in a metallic film deposited on top of the perovskite film. The heat diffuses laterally on the surface (r direction) and perpendicularly to the sample's surface (z direction). A periodic modulation of the surface reflection coefficient ΔR because of the periodically induced surface temperature modulation is sensed by a CW probe beam (488 nm) and a lock-in amplifier. Theoretical thermal models [136] are used which describe the magnitude (ΔR) and the phase (ΔΦ) of the modulated photoreflectance signal measured as a function of the distance to the pump beam. To get access to the thermal conductivity and diffusivity of the perovskite film in the r direction and the z direction (depending on the crystalline orientation of the film) the different layer systems in this example underneath, as it is a device, must be analyzed beforehand. Moreover, photo-induced degradation, [137] slight changes in the optical properties of MAPbI$_3$ perovskite across the tetragonal to cubic transition, [138] and possible degradation under intense optical excitation [139] may affect the result of the experiment.

Studies have been carried out on FAPbBr$_3$, [95] on targeted thermo-electrics such as CsSnI$_3$, [118,140–142] and on lead-free solid-state organic – inorganic halide perovskite solar cells using materials such as MASnI$_3$ [125,143] and (MA)$_3$Bi$_2$I$_9$,[144,145] with which the influences of A- and B-cation substitutions on thermal transports were examined. The obtained thermal conductivity values of 0.28 - 0.74 W $(m\,K)^{-1}$ for CsSnI$_3$ vary significantly for single crystals, nanowires, and polycrystalline films due to the enhanced phonon scattering by defects/vacancies and reduced crystal sizes. Polycrystalline MASnI$_3$ has a thermal conductivity of 0.09 W $(m\,K)^{-1}$, which is very different from the thermal conductivity of MAPbI$_3$. The broad peak observed around 220 K suggests the existence of small structural features that limit phonon mean free path even at high temperatures, as opposed to MAPbI$_3$ where this occurs at 30 K. It appears that thermal conductivity in MASnI3 exhibits a glassy behavior over a wider temperature range, which may be attributed to an effective scattering [125]. Zero-dimensional Bismuth (Bi) based perovskites, for instance, have a lower thermal conductivity of 0.21 W $(m\,K)^{-1}$ than Pb based systems, which is due to their soft phonon dispersion [146].

In the interest of completeness, it should be mentioned that, besides these modulated heating techniques, thermal diffusivity measurements using a pulsed laser heating source for transient picosecond time-domain thermal-reflectance (TDTR) were presented [147]. Although the results of the first TDTR measurements of MAPbI$_3$ thin films [130] significantly differ from other results (TDTR determines a thermal conductivity of MAPbI$_3$ films of 11.2 W $(m\,K)^{-1}$ at room temperature), this method is interesting because a theoretical description for frequency modulated time delay photo-thermal and photo-acoustic wave spectroscopies is given [148]. Note that the optical generation of excess carriers due to laser excitation may affect the thermal conductivity measurements.

The previously only theoretically predicted structural anisotropies in perovskites correlated with direction-dependent variations of the phonon vibrational density of states [105] could be recorded by a differential photo-acoustic method to measure the thermal conductivity of thin films [149]. Details of heat flow analysis in layered structures using a picosecond optical pump-and-probe technique can be found elsewhere [150]. In addition to the space and time domains, thermal properties have been measured in the frequency domain. Nowadays, frequency-domain thermo-reflectance (FDTR) is used besides TDTR to simultaneously measure in-plane and cross-plane thermal properties [151]. This technique can determine the thermal conductivity and heat capacity of a sample at the same time, and it combines the advantages of TDTR with the relative experimental simplicity of modulated photo-thermal methods. Using FDTR, the

thermal conductivities of various single crystal lead halide perovskites were found to be proportional to $C_{a-cubic} \, \bar{v}_s/3$, where $C_{a-cubic}$ is the volumetric heat capacity of acoustic phonons based on a cubic unit cell and $\bar{v}_s$ is the speed of sound [95]. An average acoustic phonon mean-free path $l_{mfp-phonon}$ = 4.3 nm was determined. Thus, it could be shown that this technique is very promising for the determination of thermal properties.

In addition, the groups Liu et al. and Haque et al. [152,153] use the 3ω-method to measure the thermal conductivity of MHPs (see **Table 3**). Finally, this method will be explained in detail, since the measurement technique used in this work is also based on the 3ω-method, albeit in a SThM.

A resistive strip mounted on the sample is heated with a sinusoidal current of the angular frequency ω. Thus, the heating power is composed according to the electrical power and the heating current $I(t) = I_0 \cdot sin(\omega t)$:

$$P(t) = R \cdot I_0{}^2 \cdot \frac{1}{2} \cdot [1 - cos(2\omega t)] \tag{9}$$

Since the heating power is proportional to the square of current, the diffusive thermal wave penetrating the sample has a periodicity of 2ω. Since the heating generation occurs at 2ω, the electrical resistance also changes with the same frequency due to the temperature-coefficient of the heater:

$$\Delta T(t) \propto \Delta R(t) \tag{10}$$

$$\Rightarrow R(t) = R_0 + \Delta R(t) = R_0^* - \frac{dR}{dT} \cdot \Delta \widehat{T} \cdot \frac{1}{2} \cdot [cos(2\omega t + \varphi)] \tag{11}$$

$\frac{dR}{dT}$ is the temperature coefficient of the heater and R_0^* is the mean value of the wire resistance considering self-heating. $\Delta \widehat{T}$ represents the amplitude of the periodic temperature change of the heater and φ the phase angle between $\Delta \widehat{T}$ and the heater power $P(t)$.

The electrical voltage drop across the wire is given by the product of the electrical current and the resistance of the probe by:

$$U(t) = R(t) \cdot I(t) =$$

(12)

$$= (R_0^* \cdot I_0) \cdot sin(\omega t) + I_0 \cdot \frac{dR}{dT} \cdot \frac{\Delta T}{4} sin(\omega t - \varphi) - I_0 \cdot \frac{dR}{dT} \cdot \frac{\Delta T}{4} sin(3\omega t - \varphi)$$

The 3ω-component of the detected signal is independent of the mean value of the electrical resistance of the strip and thus also independent of the temperature of the sample. This is advantageous because thermal properties of the sample can thus be investigated as a function of temperature. The amplitude of temperature changes ΔT within the sample with distance r from the heat source is given by Carslaw and Jaeger [154] as:

$$\Delta T(r) = \frac{P}{l\pi\lambda} \cdot K_0(qr),$$

(13)

where $\frac{P}{l}$ is the amplitude of the injected heat power per length and K_0 is the zeroth ordered modified Bessel function. ζ is defined as a complex thermal wave number according to [155]:

$$\lambda = |\zeta|^{-1} = \sqrt{\frac{a}{2\omega}}$$

(14)

The magnitude of this quantity is the wavelength of the diffusive thermal wave, or according to Cahill the thermal penetration depth. As shown by Cahill [156], the equation (13) of Carslaw and Jaeger can be approximated as follows:

$$\Delta T = \frac{P}{\pi\lambda} \cdot \left[\frac{1}{2} ln\left(\frac{2D}{r^2}\right) - 0.5772 - \frac{j\pi}{r} - ln(\omega) \right]$$

(15)

As can be seen from this approximation (15), the last term depends on the modulation frequency ω. Please note that the logarithmic term is calculated without units and the values corresponds to SI units. Consequently, if ΔT is inserted into the 3ω–component of equation (12) and a difference of the signal is measured at two frequencies, the thermal conductivity can be determined from the slope:

$$\frac{U_{3\omega_1} - U_{3\omega_2}}{ln(\omega_1^*) - ln(\omega_2^*)} = \frac{1}{4} \cdot I_0 \cdot \frac{dR}{dT} \cdot \frac{P}{l\pi\lambda}$$

(16)

2.4.4. Concluding remarks

Within this chapter, the current state of the field has been presented and both experimental results and theoretical findings have been shown. In this regard, a table is provided below (**Table 2**), which presents the results of individual research groups as an overview. The following table shows mean values of heat dissipation quantities at room temperature obtained from molecular dynamics calculations and experimental investigations for most common metal halide perovskites in comparison to other solar cell materials. For this purpose, the results of this work have already been inserted and included in the calculation of the mean values and their summary **Table 3** (highlighted in blue color).

In addition to the disadvantages of the far-field thermal measurement methods presented so far, it is known that heat transport is strongly dependent on the dimensions of the materials and is of increasing interest when the layer thickness is reduced [157,158]. Furthermore, high-resolution measurement methods are required to investigate on thermal properties so that dependencies of polymorphs and grain boundaries can be analyzed. In this work, the heat transport, and the determination of the thermal properties of metal halide perovskite semiconductors are investigated by using a scanning probe microscopy-based technique. The development and operation of scanning thermal microscopy (SThM) is described in the following chapter.

Table 2: *Mean values of heat dissipation quantities at RT obtained from molecular dynamics calculations and experimental investigations (see **Table 3**) for most common perovskites in comparison to other solar cell materials.*

Material	λ $[W\ (m\ K)^{-1}]$	a $[mm^2\ s^{-1}]$	$C_{spec.}$ $[J\ (g\ K)^{-1}]$	$C_{vol.}$ $[J\ (cm^3\ K)^{-1}]$	$\bar{v}_s$ $[m\ s^{-1}]$
MAPbI₃	0.35 ± 0.02	0.28 ± 0.07	0.31 ± 0.08	1.28	1295 ± 134.35
MAPbBr₃	0.39 ± 0.07	0.35 ± 0.08	0.38 ± 0.09	1.45	1717^{+79}_{-126}
MAPbCl₃	0.51 ± 0.11	0.45 ± 0.09	0.51 ± 0.13	1.62	2194^{+71}_{-108}
CsPbI₃	0.45 ± 0.05	-	-	-	-
CsPbBr₃	0.43 ± 0.06	0.40 ± 0.07	0.28 ± 0.04	1.29 ± 0.14	1361^{+74}_{-96}
CsPbCl₃	0.53 ± 0.03	0.49 ± 0.01	0.27 ± 0.03	1.12 ± 0.13	-
Si	156 [159]	78	0.7 [160]	1.6	8500
GaAs	45 [159]	26	0.33 [161]	1.7	5300
CZTS	4.72 [162]	20 [162]	0.05 [162]	0.24	-
CZTSe	4.26 [162]	20 [162]	0.04 [162]	0.21	-
Organic	0.3 [163]	0.15	1.7	2 [164]	-

Table 3: Thermal quantities obtained from molecular dynamics calculations and experimental investigations

compound	SC /PC	λ [Wm⁻¹K⁻¹]	c_{spec} [Jkg⁻¹K⁻¹]	c_{vol} [MJm⁻³K⁻¹]	a [mm²s⁻¹]	measurement technique	Seebeck Coefficient [µV K⁻¹]	expansion coefficient [10⁻⁴K⁻¹]	direction	density [kgm⁻³]	$\bar{v}_s$ [ms⁻¹]	measured @ [K]	crystal phase	perovskite manufacturing	year	ref.
MAPbI₃	SC	0.5				Steady-state method						RT	tetragonal	ITC	2014	[121]
MAPbI₃	SC	0.31 or <1 for all phases				MDS						RT	orthorhombic, tetragonal, cubic		2016	[105]
MAPbI₃	SC	0.30-0.42 (i)				Laser flash	920 ±91					298-425	tetragonal - cubic	ITC/vapor diffusion	2017	[128]
MAPbI₃	SC	0.34 ±0.12				SThM / 3ω method		−5.1 ±0.4 AFM				RT-313	tetragonal	ITC	2017	[14]
MAPbI₃	SC	0.14 ±0.02				Micro-photoluminescene						RT	tetragonal	two-step CVD grown	2017	[259]
MAPbI₃	SC	0.34 ±0.08	310.755 calculated	1.28 [260]	0.28 calculated	FDTR				4119	1390^{+43}_{-66}	RT	tetragonal	vapor diffusion	2017	[95]
MAPbI₃	SC	0.59				MDS						160-330	tetragonal		2016	[106]
MAPbI₃	SC	1.8				MDS						>330	pseudocubic		2016	[106]
MAPbI₃	SC	0.30				Laser flash		58.2 × 10−6 K-1	110	4184		RT	tetragonal	ITC	2018	[65]
MAPbI₃	SC - NW	0.22				Microbridge - Device						RT	tetragonal	[261]	2018	[119]
MAPbI₃	PC	0.6				longitudinal steady state technique						RT	tetragonal	vacuum quenching	2017	[123]
MAPbI₃	PC	0.33 ±0.12				SThM / 3ω method						RT-318	tetragonal	Spincoating/PHP	2017	[14]
MAPbI₃	PC	0.3				Steady-state method						RT	tetragonal	ITC/glueing	2014	[121]
MAPbI₃	PC	11.2 ±0.8				Time-domain thermal reflectance						RT	tetragonal	[262]	2016	[130]
MAPbI₃	PC	0.38				Laser flash	-1350 ±50					300K-450K	Tetragonal cubic	mechanical alloying via high energy ball milling	2019	[145]

compound	SC/PC	λ [Wm⁻¹K⁻¹]	c_spec [Jkg⁻¹K⁻¹]	c_vol [MJm⁻³K⁻¹]	a [mm²s⁻¹]	measurement technique	Seebeck Coefficient [µV K⁻¹]	expansion coefficient [10⁻⁴K⁻¹]	direction	density [kgm⁻³]	v̄_s [ms⁻¹]	measured @ [K]	crystal phase	perovskite manufactoring	year	ref.
MAPbI₃	PC	0.36±0.01				Laser flash						300K	tetragonal	-	2019	[146]
MAPbI₃	PC	0.32 ± 0.03				3ω method	-6500/5500					RT	tetragonal	two-step sequential vacuum deposition (SVD)	2019	[153]
MAPbI₃	PC	0.31±0.03 for film thicknesses of 65±3 nm				3ω method						RT		coevaporation	2019	[152]
MAPbI₃	PC	0.44±0.03 for film thicknesses of 80±5 nm				3ω method						RT		coevaporation	2019	[152]
MAPbI₃	PC	0.59±0.04 W/(m K) for film thicknesses of 100±12 nm				3ω method						RT		coevaporation	2019	[152]
MAPbI₃	PC						820(Dark) 540(Light)							ITC	2015	[125]
MAPbI₃	PC	average 0.4				TDTR					1.2 ± 0.3 × 10^3 m/s	RT		Spincoating	2016	[129]
MAPbBr₃	SC	0.44 ± 0.08				SThM / 3ω method						RT		ITC	2017	[14]
MAPbBr₃	SC	0.51 ± 0.12	378.2 calculated	1.45 [260]	0.352 calculated	FDTR				3834	1717⁺⁷⁹₋₁₂₆	RT	cubic	vapor diffusion	2017	[95]
MAPbBr₃	SC	0.37				Laser flash		32.0 × 10⁻6 K⁻1	100	3863		RT	cubic	ITC	2018	[65]
MAPbBr₃	SC - NW	0.32				Microbridge - Device						RT	cubic	[261]	2018	[119]
MAPbBr₃	PC	0.39 ± 0.05				SThM / 3ω method						RT		Spincoating/PHP	2017	[14]

compound	SC/PC	λ [Wm^{-1}K^{-1}]	c_{spec} [Jkg^{-1}K^{-1}]	c_{vol} [MJm^{-3}K^{-1}]	a [mm^{2}s^{-1}]	measurement technique	Seebeck Coefficient [μV K^{-1}]	expansion coefficient [10^{-4}K^{-1}]	direction	density [kgm^{-3}]	$\bar{v}_s$ [ms^{-1}]	measured @ [K]	crystal phase	perovskite manufactoring	year	ref.
MAPbI₃	SC	0.73 ± 0.18	510.88 calculated	1.62 [260]	0.451 calculated	FDTR				3171	2194^{+71}_{-108}	RT	cubic	vapor diffusion	2017	[95]
MAPbI₃	SC	0.50 ± 0.05				SThM / 3ω method						RT		ITC	2017	[14]
MAPbI₃	SC	0.52				Laser flash		$29.6 \times 10{-}6 \ \text{K}{-}1$	100	3158		RT	cubic	ITC	2018	[65]
MAPbI₃	PC	0.50 ± 0.12				SThM / 3ω method						RT		Spincoating/PHP	2017	[14]
CsPbI₃	SC - NW	0.45 ± 0.05 (κl)				NW thermometry technique						RT		x	2017	[118]
CsPbBr₃	PC	0.43 ± 0.03	290 ± 90 calculated	1.3±0.4	0.3 ± 0.1	SThM / 3ω method				4550		RT	orthorhombic	Spincoating/PHP	2019	[179]
CsPbBr₃	SC	0.46 ± 0.12	219.3 calculated	1.06	0.434 calculated	FDTR				4834	1361^{+74}_{-96}	RT	orthorhombic	vapor diffusion	2017	[95]
CsPbBr₃	SC	0.514	280	1.29 calculated	0.399	Pulse transient method				4604		37°C			2008	[224]
CsPbBr₃	SC - NW	0.36				Microbridge - Device						RT	orthorhombic	[261]	2018	[119]
CsPbBr₃	SC - NW	0.42 ± 0.04 (κl)				NW thermometry technique						RT		x	2017	[118]
CsPbCl₃	SC	0.530	272	1.12 calculated	0.475	Pulse transient method				4102		25°C		[223]	2008	[224]
CsPbCl₃	SC	0.55±0.03	272.10±7.35	1.143 calculated	0.485 ± 0.02	Pulse transient method				4200		50°C		[223]	2000	[117]
CsPbCl₃	PC	0.49±0.04	220±70 calculated	0.9±0.1	0.5±0.1	SThM / 3ω method						RT	monoclinic	Spincoating/PHP	2020	[101]

compound	SC /PC	λ [Wm⁻¹ K⁻¹]	c_{spec} [Jkg⁻¹K⁻¹]	c_{vol} [MJm⁻³K⁻¹]	a [mm²s⁻¹]	measurement technique	Seebeck Coefficient [µV K⁻¹]	expansion coefficient [10⁻⁴K⁻¹]	direction	density [kgm⁻³]	$\bar{v}_s$ [ms⁻¹]	measured @ [K]	crystal phase	perovskite manufactoring	year	ref.
FAPbBr₃	SC	0.49 ± 0.12	443.92 calculated	1.69	0.29 calculated	FDTR				3807	1333^{+51}_{-73}	RT	cubic	vapor diffusion	2017	[95]
MASnI₃	PC	0.09				Steady state method	-720							ITC	2015	[125]
CsSnI₃	SC - NW	0.38 ± 0.04 (⊥)				NW thermometry technique						RT		x	2017	[118]
CsSnI₃	SC-NW	0.57				NW thermometry technique	79					300K		x	2017	[118]
CsSnI₃	PC	0.36				3ω method	115					RT		Spincoating	2020	[140]
CsPb₂Br₅	PC	0.33 ± 0.02	180 ± 60 calculated	1.1±0.3	0.3 ± 0.1	SThM / 3ω method				5850		RT		Spincoating/PHP	2019	[179]
Cs₄PbCl₆	PC	0.30±0.03	150±80 calculated	0.5±0.2	0.5±0.1	SThM / 3ω method						RT		Spincoating/PHP	2020	[101]
(MA)₃Bi₂I₉	PC	0.21				Laser flash	2600 ± 200					300K-450K		mechanical alloying via high energy ball milling, followed by hot pressing	2019	[145]
(MA)₃Bi₂I₉	PC	0.23± 0.02				Laser flash						300K		-	2019	[146]

3. Simultaneous mapping of thermal properties of metal halide perovskites

Since stationary and dynamic heat transport is of interest in many interdisciplinary fields of research, a variety of thermal measurement methods have been developed, which enable the simultaneous detection of thermal conductivity and thermal diffusivity [165–167]. However, these are all macroscopic methods, that are not suitable to measure thermal properties with a high spatial resolution and on thin films. For layers with a thickness below 100 nm, ballistic heat transport and phonon scattering at the interfaces significantly influence the diffusive heat flow [168–170]. So, the scanning near-field thermal microscope (SThM) is particularly suited to assess the thermal transport even in thin films [168]. In the following chapter, an introduction into the near-field technique of scanning thermal microscopy (SThM) for the nanoscopic determination of thermal properties is presented. In the second section, an extended SThM technique is developed, which for the first time allows simultaneous mapping of thermal conductivity, thermal diffusivity, and volumetric heat capacity. This technique is validated in selected case studies that are demonstrated in the third paragraph of this chapter.

3.1. Introduction into scanning near-field thermal microscopy

By measuring the difference in contact potentials caused by heating the SThM tip or sample, Nonnenmacher and Wickramasinghe invented the first method to determine the local thermal conductivity [171]. By using resistive thermal probes, where the heat source and temperature sensor are combined in one element, local heat transport within electronic materials and devices was qualitatively mapped with high spatial resolution in 1994 [172,173].

The 3ω- technique (see 2.4.3.) was applied 1999 by Fiege et al. [155] to SThM expanding quantitative thermal conductivity measurements to atomic force microscopes (AFMs) by means of a modulated heating source. The combination of SThM and the 3ω-technique allows the quantitative determination of the thermal conductivity with high spatial resolution. When using the scanning thermal microscope, the measuring strip, that is commonly used for the 3ω method and which also serves as a heating element, is now replaced by a resistive thermal tip. The measuring tip used in this thesis is the commercially available VITA-HE-GLA-1 tip from Bruker [174]. This resistive measuring tip is heated with a sinusoidal current with angular

frequency ω and it is brought into contact with the sample surface via the AFM distance control. The contact force is kept constant. Thus, the 3ω-technique can be applied (see **Figure 10**) measuring the resulting amplitudes of the temperature oscillations ΔT of the thermal resistive probe at 3ω_{min} and 3ω_{max}, the lower frequency limit ω_{min} and the upper frequency limit ω_{max} given by the thermal probe.

The thermal probe of the SThM is always electrically dynamically powered by $\widehat{P}_{el.} = 128\mu W \pm 3\,\mu W$. Knowing the differential thermal coefficient of the probe $\frac{dR}{dT}$, $\widehat{T}_{probe}$ can be measured from the in-phase component of the voltage drop at the thermal resistive probe using lock-in amplification with a sensitivity of 80 $\frac{mK}{\sqrt{Hz}} \pm 8\, \frac{mK}{\sqrt{Hz}}$, limited by the internal resistance of the probe. Since the temperature oscillation depends on the local heat flux $\dot{Q}_s(\vec{r})$ into the sample, on its local thermal conductivity $\lambda(\vec{r})$ and thermal diffusivity $a(\vec{r})$, as well as the applied frequency ω one may approximate [155,156]:

$$\widehat{T}_{probe}(\vec{r}) = \frac{\dot{Q}_s(\vec{r})}{\lambda(\vec{r})} \cdot \left(\frac{1}{2}\ln\left(\frac{a(\vec{r})}{(50nm)^2}\right) - \frac{1}{2}\ln(\omega) + ln(2) - 0.5772 \right) \tag{17}$$

For samples with low thermal conductivity (<10 W/(m·K)), the heat dissipation into the supply lines of the thermal probe must be considered in SThM [169,175,176]. Since the local heat flux into the sample depends quadratically on $\lambda(\vec{r})$ for those samples with a low thermal conductivity and only 13.5% ± 3.5% of the heat flow dissipates from the used thermal probe into a glass substrate (λ_{glass} = 1.2 W/(m·K)), the local heat flux into the perovskite sample is given by $\dot{Q}_s(\vec{r}) = \frac{13.5\%}{100nm \cdot \pi \cdot \lambda_{glass}^2} \cdot \widehat{P}_{el.} \cdot \lambda(\vec{r})^2$ according to [177,178]. It is important to note, that the SThM in the present work is installed in the analysis chamber of a scanning electron microscope, thus our SThM measurements are carried out under vacuum (5 × 10^{-6} mbar). Effects of thermal transport due to convection and related to ambient gases can therefore be excluded. A constant low force between SThM probe and sample was applied during these measurements to guarantee a constant thermal contact resistance while at the same time avoiding mechanical influences/damages to the perovskite films. It should be noted that when analyzing the thermal properties of perovskites, the grain boundaries should not be disregarded. Suppose the measuring tip moves over the grain boundary of two neighboring perovskite grains. In that case, the measuring tip has more contact, and an increased heat flow is a consequence, so an increase in thermal conductivity can be seen in the measurement result. Thus, topography

and the measurement of thermal conductivity must be compared to consider the influence of the topography.
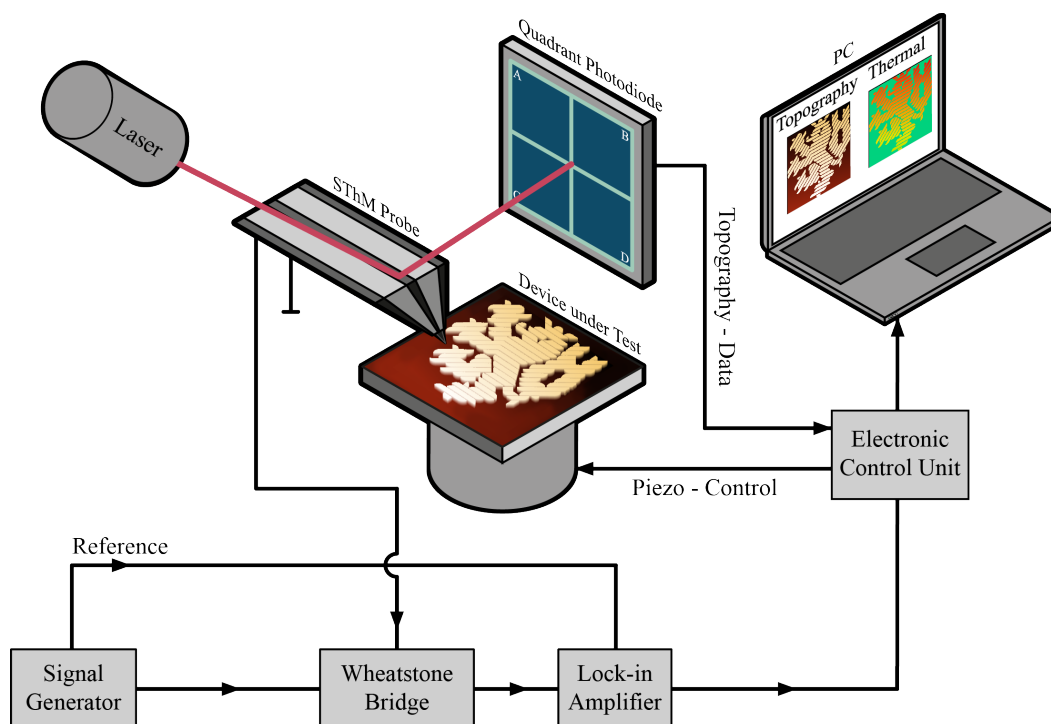
Figure 10: *Schematic illustration of the setup of the scanning thermal microscope (SThM).*

For example the average thermal conductivities of 0.36 ± 0.08 W $(m\,K)^{-1}$ and 0.44 ± 0.02 W $(m\,K)^{-1}$ in CsPbBr$_3$ perovskite films and single crystals, respectively, were determined within an area of 10×10 μm^2 for signal to noise improvement using glass as a reference (see **Figure 11**). While the thermal conductivity of single crystals can be determined quantitatively with a low uncertainty, that of thin layers is greater, presumably due to inhomogeneities in this film.

Thus, thermal properties should be recorded locally. It should be noted, local measurements at two different frequencies cannot be done consecutively, because the design of the SThM tip and its frequency dependent thermal form factor would lead to a shift in the recorded area.
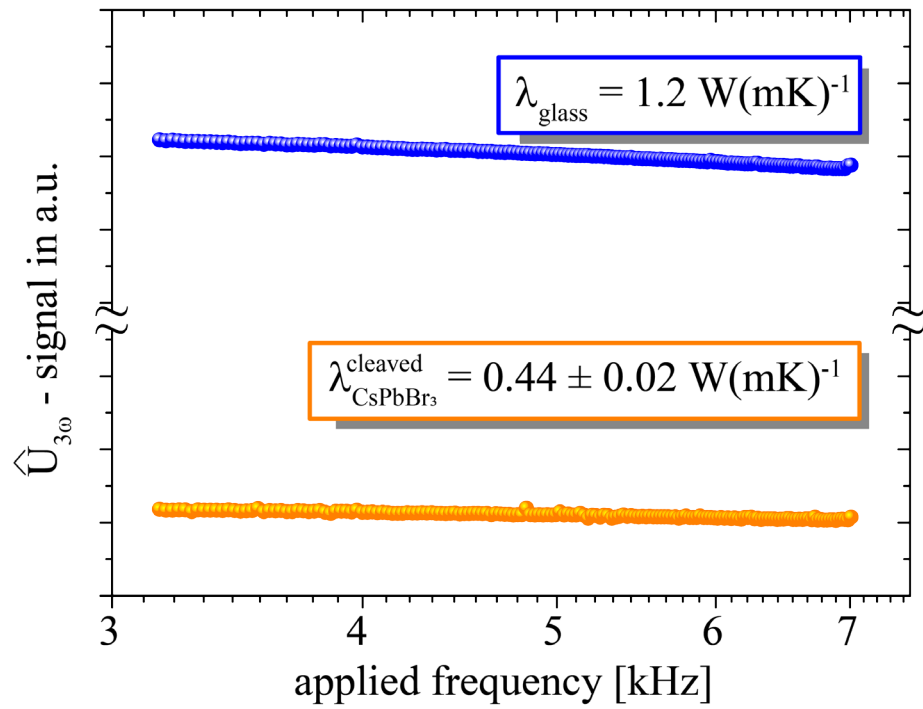
Figure 11: *Thermal conductivity of a CsPbBr₃ single crystal by the 3ω -technique using glass as reference* [179].

3.2. Development of a measurement technique for simultaneous mapping of thermal conductivity, thermal diffusivity, and volumetric heat capacity

In this work, we developed the SThM based measurement method in the frequency domain to detect simultaneously a mapping of the thermal conductivity, thermal diffusivity, volumetric heat capacity, and topography of perovskite thin films with a high spatial resolution for the first time [179]. In the following the development of the 3ω-technique in the SThM will be presented. The idea of the development was to use an adder for the measurement of thermal conductivity based on the 3ω-technique. We detected simultaneously the local temperature oscillations of the thermal SThM probe at the lower frequency limit ω_{min} and the upper frequency limit ω_{max} from the third harmonic Wheatstone bridge output signals, as shown in shown in **Figure 12**.
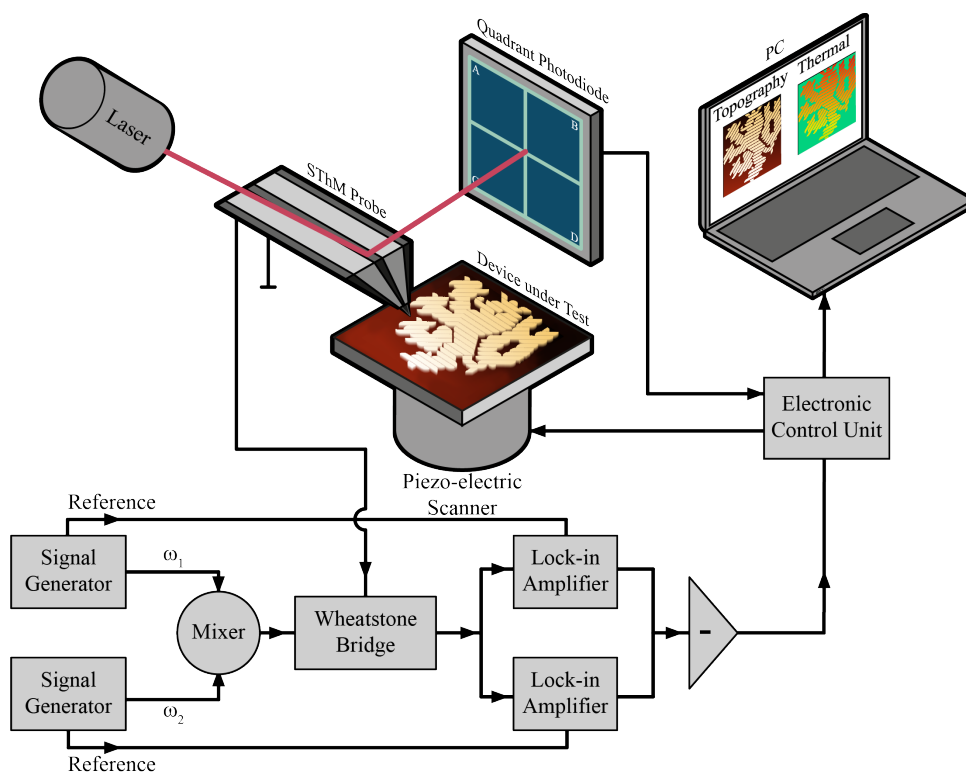
Figure 12: *Schematic illustration of extended quantitative thermal conductivity measurements by SThM applying the 3ω - measuring technique in the frequency domain.*

The resistive thermal probe of the SThM is powered by a mixed signal of two sinusoidal currents $I_{0,1}sin(\omega_1 t)$ and $I_{0,2}sin(\omega_2 t)$ with angular frequencies ω_1 and ω_2. To improve the signal to noise ratio, ω_1 and ω_2 are chosen as the lower frequency limit ω_{min} (3kHz) and the upper frequency limit ω_{max} (7kHz) of the thermal probe[174], respectively. If, on the other hand, a multiplier is used instead of an adder, ω_1 and ω_2 are chosen to fulfill the following equations: $\omega_2 - \omega_1 = \omega_{min}$ and $\omega_1 + \omega_2 = \omega_{max}$. In this case the electrical coupling factor of the mixer must be considered carefully since the maximum current, which may be applied to the SThM probe, is limited. The resulting amplitudes of the temperature oscillations $\hat{T}_{probe}$ of the thermal probe at $3\omega_{min}$ and $3\omega_{max}$, which according to Cahill and Fiege et al. are used for quantitative thermal conductivity measurements [155,156], can be measured simultaneously. Furthermore, $\hat{T}_{probe}$ is detectable independently of the ambient temperature by using the output signals of a Wheatstone bridge resulting at $(2\omega_{min} - \omega_{max})$, $(2\omega_{min} + \omega_{max})$, $(2\omega_{max} - \omega_{min})$, and $(2\omega_{max} + \omega_{max})$ in the frequency domain.

To determine the low thermal conductivity in perovskite thin films with high spatial resolution using the 3ω- technique, we subtracted the local temperature variations $\hat{T}_{probe}(\vec{r})\big|_{7kHz}$ from $\hat{T}_{probe}(\vec{r})\big|_{3kHz}$ according to equation (16). This technique allows the mapping of the thermal conductivity of our perovskite films in the frequency domain.

Aside from the thermal conductivity, the local thermal diffusivity $a(\vec{r}) = \frac{\lambda(\vec{r})}{\rho(\vec{r})c(\vec{r})}$ is of great importance. The thermal diffusivity is determined from $\hat{T}_{probe}(\vec{r})\big|_{3kHz}$ and the corresponding thermal conductivities using equation (17). In particular, the local heat capacity is of interest, since it ultimately tells the ability to store the supplied heat and local variations can even lead to discontinuous temperature gradients in dynamically operated devices [180]. Until today, experimental data of specific heat for lead halide perovskite thin films are hardly available. So far, the heat capacity was measured only once for methylammonium lead halide (MAPbX$_3$, X=I, Br, Cl) single crystals.[181] The local volumetric heat capacity of the corresponding film, which is given by the product of the local density and the local specific heat, can be directly determined from Equation (5) using our SThM data.

3.3. Validating the advanced nanoscopic thermal measurement technique on a selected demonstrator

This section discusses the validation of the advanced measurement setup of the SThM in the frequency domain. The functionality of the system is demonstrated by measurements on a selected demonstrator. In this case, a 400 nm thick aluminum oxide (Al_2O_3) film is used, that is deposited by atomic layer deposition (ALD) on a borofloat glass substrate and patterned by a lift-off process [182].Thus, the thermal properties of both the Al_2O_3 and the glass are mapped near the edge. The simultaneously recorded measured data is illustrated in **Figure 13**.
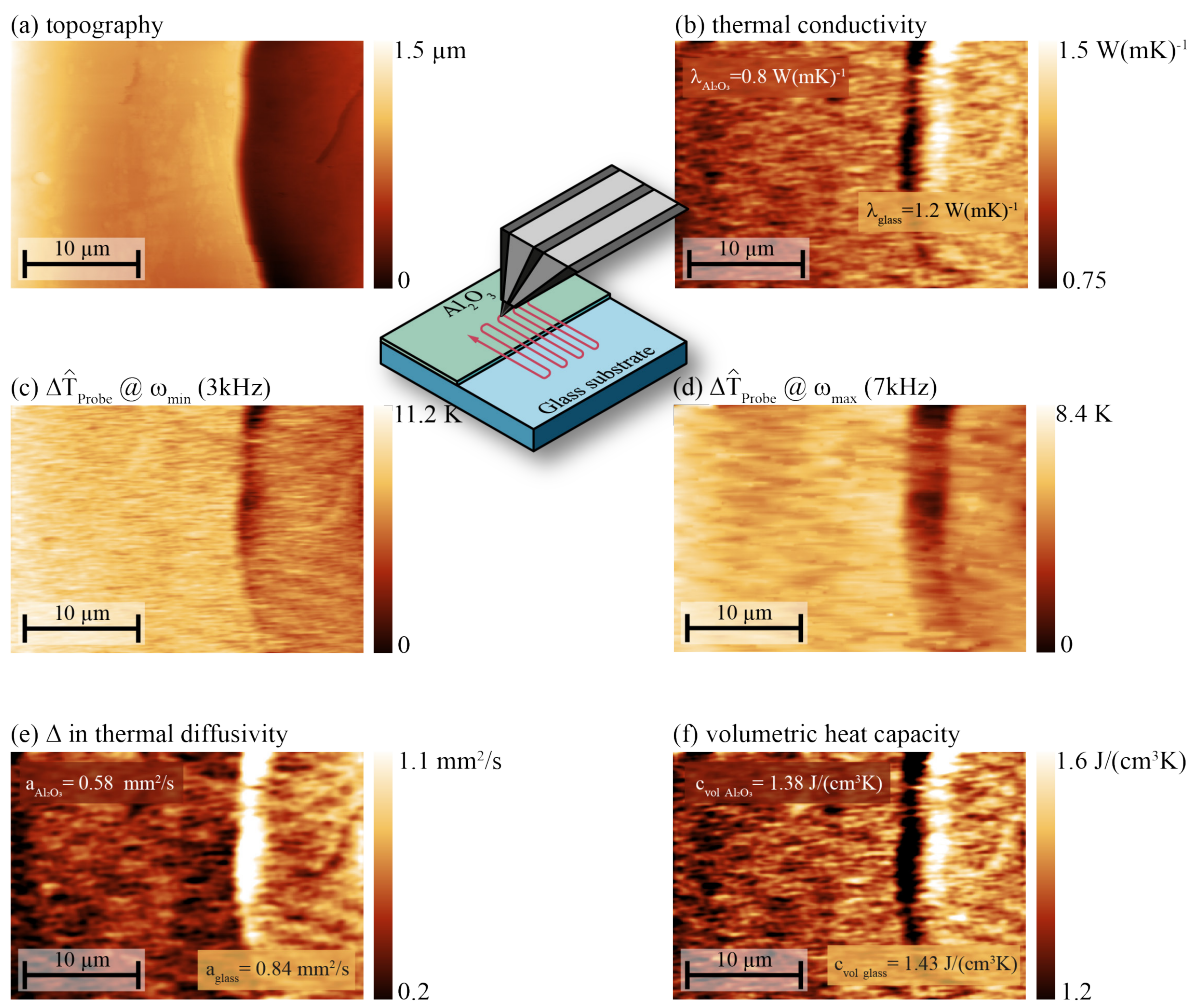
Figure 13: *(a) Topography and resulting mapping of thermal conductivity (b) from the measured corresponding differences in temperature oscillations at (c) lower frequency limit ω_{min} (3kHz) and (d) the upper frequency limit ω_{max} (7kHz) [183].(e) shows the measured thermal diffusivity and (f) the calculated volumetric heat capacity from (b) and (e).*

With the known thermal conductivity value of the glass of 1.2 $W (m\,K)^{-1}$, the thermal conductivity of Al_2O_3 is calculated to be 0.8 $W (m\,K)^{-1}$, which fits nicely to literature values [168,184]. The Al_2O_3 layer deposited by using ALD is homogeneous both in the topography and in its thermal conductivity, only at the edge towards the glass, the thermal conductivity seemingly varies. This variation is due to an increased contact area, which adds more thermal energy to the sample and the resulting temperature oscillation. Thus, changes, the simultaneous recording of the topography is also beneficial here.

In addition, the thermal diffusivity was measured and combined with the thermal conductivity, the volumetric heat capacity was determined. Here, **Table 4** gives an overview of the averaged values from the image data in comparison to literature data. c_{vol} from literature was calculated from the reported c_{spec} and the reported density.

Table 4: *Overview of the measured thermal properties of Al_2O_3 and glass in comparison with literature values.*

	λ $[W (m\,K)^{-1}]$		a $[mm^2 s^{-1}]$		c_{vol} $[J cm^{-3} K^{-1}]$		c_{spec} $[J g^{-1} K^{-1}]$		ρ $[g cm^{-3}]$
	measured	literature	measured	calc. from literature	calculated	calc. from literature	calculated	literature	literature
Al₂O₃	0.8 ± 0.08	0.9 [185]	0.58 ± 0.1	0.4	1.38 ± 0.3	2.03	0.53 ± 0.3	0.784 [186]	2.6 [187,188]
glass		1.2 [182]	0.84 ± 0.1	0.64	1.43 ± 0.3	1.87	0.64 ± 0.3	0.84 [182]	2.23 [182]

Finally, the application of this measurement technique allows the investigation of local heat quantities in metal halide perovskites with a high spatial resolution. By using this scanning probe microscope technique, in addition to the simultaneously recorded topography, it is also possible to determine locally how the thermal properties of metal halide perovskites vary with respect to crystal size, near grain boundaries or due to altered stoichiometry. To eliminate topographic artifacts in SThM measurements, the following chapter deals with the preparation of smooth metal halide perovskite thin films and single crystals.

4. Fabrication of metal halide perovskite semiconductor thin films and single crystals

In the following, the sample preparation of the investigated metal halide perovskite semiconductors and their polymorphs is presented. Since thermal properties can depend on the crystal size, nanocrystalline films, large crystalline thin layers, and single crystals were investigated in this thesis. Thus, first, the conventional wet chemical deposition via spin coating of nano-polycrystalline perovskite pristine thin films is shown. Spin coating is the most widely used solution-based deposition method for thin films. Next, a planar hot pressing (PHP) imprinting technique to improve the layers with respect to grain size, roughness, orientational order, and their overall opto-electronic properties is summarized. Specifically, for poorly soluble precursor materials, a deposition technique via an advanced thermal evaporation in combination with PHP is developed and is explained in the third section of this chapter [189]. Finally, the preparation of perovskite single crystals is presented.

4.1. Solution based deposition of polycrystalline metal halide perovskite semiconductor thin films

There are different approaches how exactly the spin-coating deposition of perovskites takes place, whereby a crucial and at the same time critical aspect being the crystallization of the perovskite. Without supporting crystallization methods, the crystallization mechanism is determined by the evaporation rate of the solvent used [178] and thus indirectly by mixing ratio, post annealing parameters and the environment. The following is a summary of the processes used to prepare metal halide perovskite thin films by spin-coating. Since many developments in the preparation and further processing of these samples have been empirically determined, the reader is referred to the following publications for more specific details [26,190,191].

For the perovskite films deposited in this work, substrates were indium tin oxide (ITO) coated glass, silicon, and glass [182].
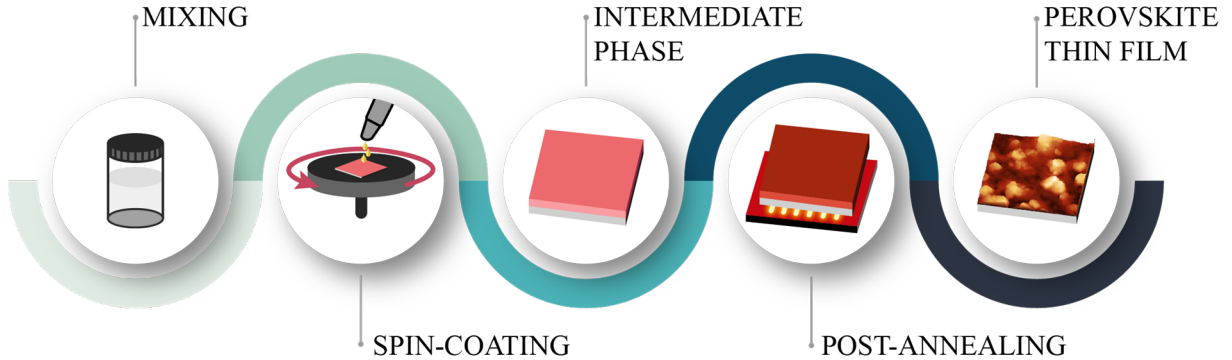
Figure 14: Schematic diagram of the spin coating procedure. For the liquid-processed deposition method to produce a perovskite thin film, the solution is mixed in a first step and then spun on. During the intermediate phase, while the perovskite layer is nucleating, quenching methods can be used. After the post - annealing step, the pristine perovskite thin film is obtained.

The solution for the liquid-processed deposition method to produce a perovskite thin film, is mixed in a first step and then spun on the substrate, as illustrated in **Figure 14**. Two precursor salts are dissolved in a solution and then spin coated in filtered form. The individual recipes for the preparation of the metal halide perovskite thin films, which were spin coated, are published in [14,26,189,190]. The ratio of the mixed salt solutions determines the extent to which both three-dimensional perovskites as well as their two-dimensional and zero-dimensional polymorphs and mixtures thereof occur. Note, that during the spin-coating process techniques like solvent engineering or gas – quenching [175–177] can be used to introduce a supersaturated state in order to improve the control over the crystallization of MHPs. In general, our perovskite films are post-annealed (60 – 150 °C on a hotplate for 30 – 60 minutes) to remove residual solvents from the intermediate adduct and to aid the crystallization process.

4.2. Preparation of highly oriented large crystalline metal halide perovskite semiconductor thin films by planar hot pressing

Using the method of thermal imprinting, Pourdavoud et al. succeeded in constructing distributed feedback lasers based on $MAPbI_3$ and $MAPbBr_3$ [26,190,192]. Lasing was also achieved in the case of all-inorganic $CsPbBr_3$ at room temperature with thresholds below 10 $\mu J/cm^2$ using PHP [190]. For a detailed description and the mechanisms behind thermal imprinting, please refer to [189,192,193]. The following is a summary of the most important aspects and is intended to illustrate the PHP process.

PHP experiments were performed in a parallel plate-based imprint system (press) [194]. During heat up of the press to the recrystallization processing temperature (from RT up to 185°C, which depends on the choice of the chosen MHP), the pressure of 100 bar was applied. When the imprint recrystallization temperature is reached the pressure is kept constant for 30 minutes in the case of hybrid MHPs and for 5 min in the case of all-inorganic MHPs. For this purpose, the described press system is loaded with a stack to start the pressing process as shown in **Figure 15**. Typically, a sample to be pressed is placed on a stamp, which has been coated with an anti-adhesion layer (fluorinated trichlorosilane, Sigma-Aldrich) [195]. This sample-stamp combination is wrapped in heat conducting foil (KU-CG30/R, Kunze GmbH) and aluminum foil (30 µm thickness) as described in [193,196].
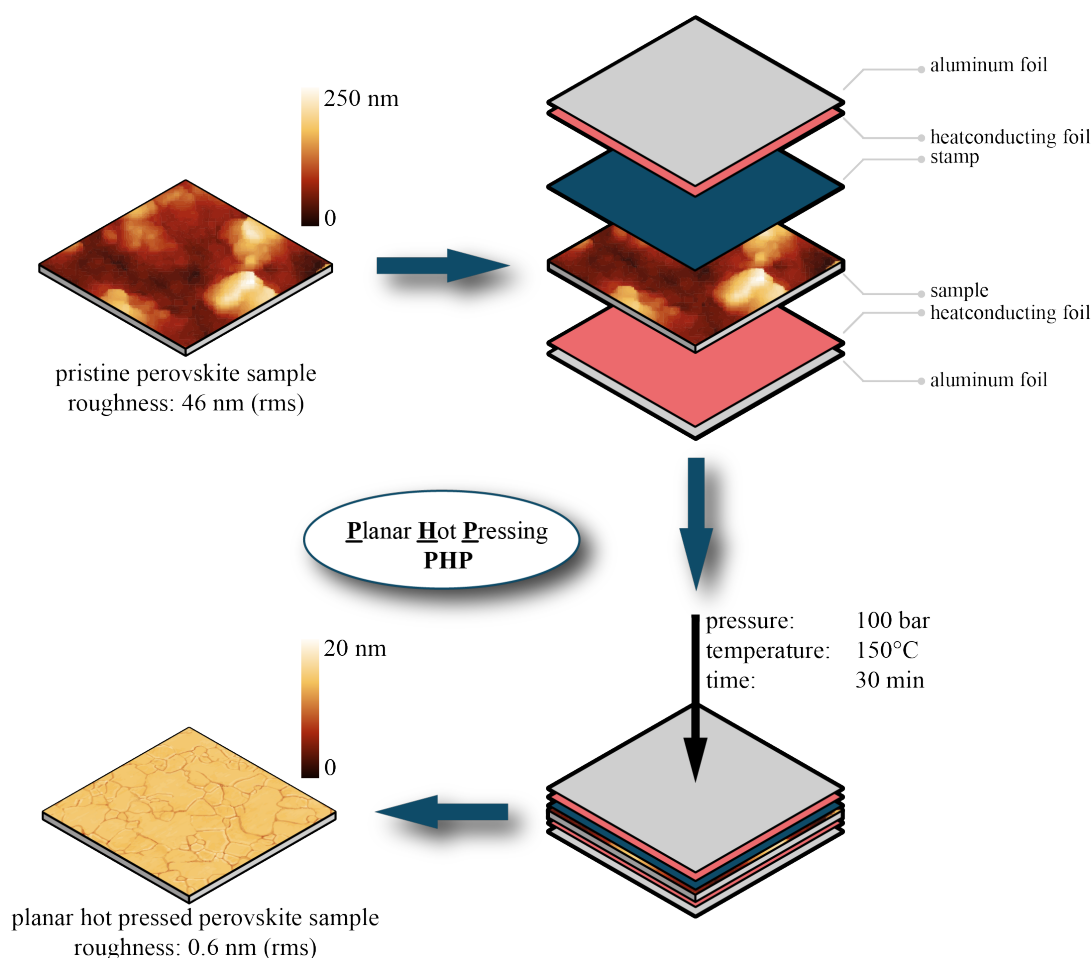
Figure 15: *Schematically shown is the planar hot pressing (PHP) recrystallization process for optimizing the pristine metal halide perovskite output layers in terms of roughness, larger grains, and in terms of their opto-electronic properties. by merging a pristine perovskite layer with an anti-adhesion coated stamp and then packaging with heat conducting foil and aluminum foil. Using a press, 100 bar pressure and a perovskite layer specific temperature is applied to this stack, resulting in a recrystallized highly oriented crystalline perovskite thin layer after an empirically defined time. This PHP process also reduces the roughness from several nm to less than 1 nm and is thus optimally suited for SThM. Here, within this illustration, CsPbBr$_3$ is added as an example where a reduction in roughness from 46 nm to <1 nm (rms) has been determined.*

In the case of the metal halide perovskites investigated in this work, the pressing parameters, pressure, temperature, and time, are adapted to the respective perovskite composition. Here, the MA-based perovskite thin films were pressed at 100 bar for 5 minutes. MAPbX$_3$ (X=Br, Cl) was recrystallized at a temperature of 150 °C. The MAPbI$_3$ perovskite thin films at 100 °C. The Cs-based perovskite thin films were pressed at 100 bar for 30 min at 150 °C. All perovskite films used for this work were loaded cold into the press and were heated to the target temperature only after the pressure of 100 bar was reached. The target temperature is the

temperature required for the recrystallization of the perovskite and differs with the composition of the perovskite. Once the temperature was reached, the pressure was maintained for the specified time and finally abruptly cooled while still maintaining the pressure. For further information the reader is referred to [26,189–191].

PHP affords flattened thin films with a roughness typically below 1 nm and crystallites with increased lateral extension compared to the pristine layer. At the same time, the optoelectronic properties are improved, so that the recrystallization by thermal imprinting enabled lasing at room temperature. Thus, the films produced for heat transport studies in metal halide perovskite semiconductors were also used for research projects on the production of lasers. [26,189,190,192]. For better understanding, only the results of the complementary electron backscattering diffraction (EBSD) investigations are briefly presented below.

The presence of the two-dimensional and three-dimensional phases in the PHP pressed cesium lead bromide-based layers was demonstrated by SEM studies and EBSD (see **Figure 16**) [190].
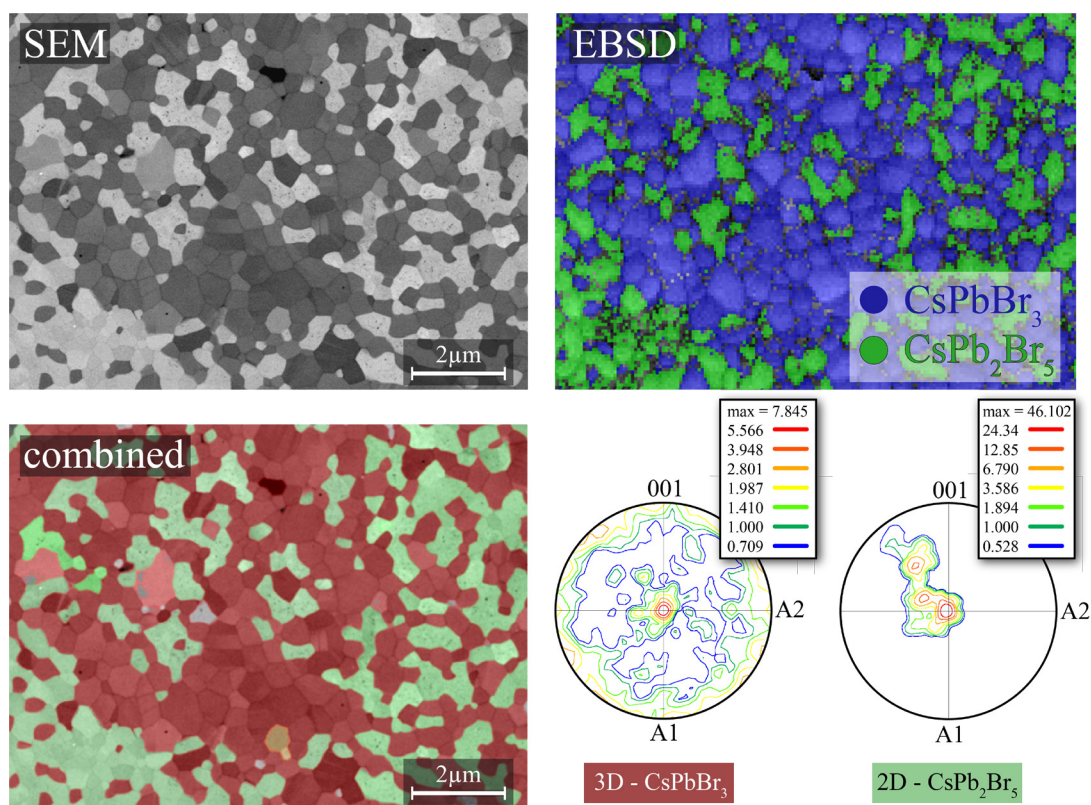
Figure 16: *Images obtained by scanning electron microscopy (SEM) by detecting backscatter electrons, as well as electron backscattering diffraction (EBSD) of a pressed/recrystallized cesium lead bromide-based layer* [190]. *Pole figures of the two relevant phases, with the compression direction in the center of the pole figure. The directions A1 and A2 are randomly selected. The measurements were performed by Dr. Stefan Zaefferer (Max Planck Institute for Iron Research GmbH).*

The SEM image acquired with backscattered electrons shows a clear contrast between bright and dark crystals, which cannot be explained by topography. Complementary EBSD shows that the crystals appearing dark in the SEM are $CsPbBr_3$ (3D), while the crystals appearing bright are $CsPb_2Br_5$ (2D). In this case, the higher lead content in the two-dimensional phase of the Cs_2PbBr_5 perovskite leads to a stronger backscattering of electrons. Note, to reduce the formation of $CsPb_2Br_5$, the CsBr concentration in the initial solution was increased, so that from an original 1:1 molar ratio of $CsBr:PbBr_2$, a 2.75:1 solution has been empirically determined, which leads to a pure three-dimensional $CsPbBr_3$ perovskite thin film after. There were three crystallographic phases used for pattern indexing: cubic $CsPbBr_3$, ICSD-ID 29073, space group 221 with lattice constants 0.5874 nm, orthorhombic $CsPbBr_3$, ICSD-ID 97851, space group 62 with lattice constants a = 0.8207 nm, b = 0.8255 nm, and c = 1.1759 nm, and the tetragonal $CsPb_2Br_5$, space group 140, lattice constants a = 0.846 nm and c = 1.595 nm. As a result of pattern indexing, two fractions of grains were identified. The tetragonal phase $CsPb_2Br_5$ is indexed for one fraction. The SEM image shows these grains as bright grains. Both the orthorhombic and cubic phases of $CsPbBr_3$ can be indexed for the other fraction. However, cubic phases fit the data significantly better: not only is the angular deviation between experimental and theoretical recalculated patterns smaller for cubic phases, but cubic phases also result in unique crystal orientations per grain, while orthorhombic phases result in many pseudosymmetric solutions for many grains. As a consequence, it is impossible to determine whether it is the cubic or orthorhombic phase with certainty, due to the low pattern quality. In both cubic and orthorhombic structures, the plane normal points in the direction of compression (CD). The left pole figure shows the (001) for the cubic phase. The right pole figure shows a very strong (001) || CD fiber texture in the tetragonal phase.

Via the EBSD measurements and the simultaneous SEM measurements, the thermal measurements can be assigned to the individual polymorphs/dimensions via the contrast difference of the grains present since the SThM is built into a SEM as a hybrid system.

4.3. Thin film deposition of poorly soluble precursor materials by thermal evaporation

Due to the limited concomitant solubility of some precursor salts, not all MHP semiconductors can be produced using the previously described wet chemical deposition method. For example, in the case of $CsPbCl_3$, attempts were made to dissolve CsCl and $PbCl_2$ in various solvents (see **Table 5**). It turned out that CsCl is well soluble in formamide and $PbCl_2$ in DMF, but not vice versa. NMF was found to provide at least some concomitant, albeit overall poor solubility.

Table 5: Demonstration of the non-existent/poor solubility of the two precursor salts CsCl and $PbCl_2$ to form $CsPbCl_3$.

solvent	CsCl solubility (20mg ml^{-1})	PbCl$_2$ solubility (20mg ml^{-1})
Acetonitrile	-	-
Pyridine	-	-
Formamide	+	-
butanol, 2-	-	-
Dimethylformamide (DMF)	-	+
Dimethyl sulfoxide (DMSO)	-	-
propanol, 2-	-	-
Chloroform	-	-
Gamma-butyrolactone (GBL)	-	-
2-Pyrrolidinone	-	-
n-methylformamide (NMF)	-o	-o
n-methyl-2-pyrrolidone (NMP)	-	-
Dimethylacetamide (DMA)	-	-
Dichloromethane (DCM)	-	-
polypropylene carbonate (PPC)	-	-
Water	+	-

As can be seen in **Figure 17**, the deposition from solution of CsCl and $PbCl_2$ in NMF affords only highly discontinuous structures which are not useful for device applications. Therefore, liquid processing has not been followed any further for this material.
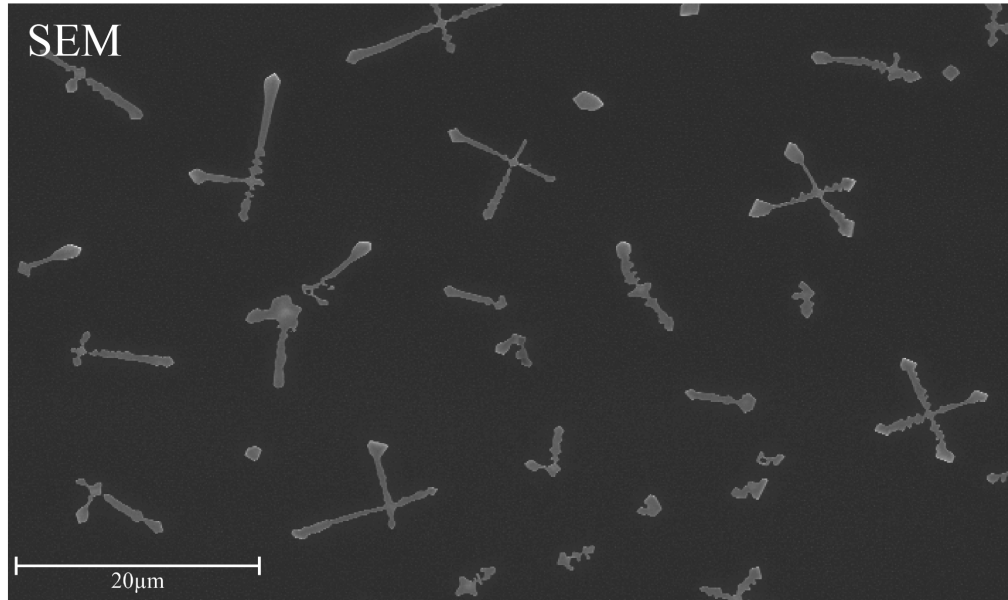
Figure 17: *SEM image capture of an attempt to liquid process $CsPbCl_3$ using the most promising solution (NMF).*

Instead, thermal evaporation, which is a physical vapor deposition (PVD) process, has been resorted to. Thermal evaporation has previously been used for the deposition of halide perovskites, e.g. for large-area solar cells [197].

For the deposition of $CsPbCl_3$, CsCl and $PbCl_2$ were loaded into separately heated crucibles, that are located in a high vacuum chamber (10^{-6} mbar). The deposition rates were monitored by a quartz crystal microbalance (QCMs). However, since only one QCM is built in, it was decided to deposit the precursor materials sequentially in a layer by layer fashion. Additionally, this layered sample design results in the opportunity to gain a better understanding of perovskite formation. To match the appropriate stoichiometry of the three-dimensional $CsPbCl_3$ perovskite, preliminary experiments were carried out.

First, a thick $PbCl_2$ layer of 50 nm was deposited, and then a varying layer thickness of CsCl from 1 nm to 200 nm was added. This experimental setup was chosen to answer two questions: whether a $CsPbCl_3$ perovskite layer can form at all and at what layer thickness of CsCl a self-limitation occurs. The individual layers were examined for their PL intensity as illustrated in **Figure 18**.
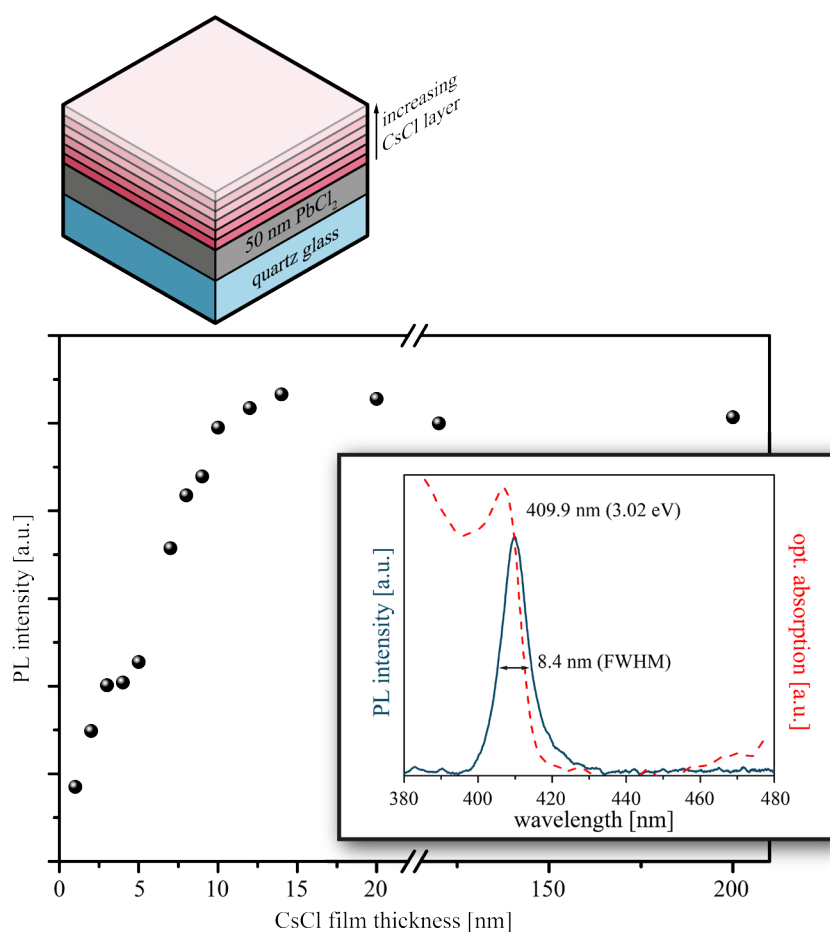
Figure 18: *Shown is the photoluminescence intensity versus a rising CsCl layer on 50 nm PbCl₂. Also shown is the photoluminescence spectrum of the fabricated CsPbCl₃ perovskite thin films, which is comparable from its band gap to those reported in the literature* [198].

As can be seen from the graph, the PL intensity saturates for a CsCl layer thickness ≥ 9 nm. Now, to determine how much $PbCl_2$ would be needed to form a 3D $CsPbCl_3$ perovskite from 9 nm CsCl, Rutherford backscattering (RBS) was used to determine the density of the vapor-deposited films and to calibrate the QCMs using the RBS measurements.

Here samples are irradiated with helium ions from a particle accelerator. The backscattered ions are recorded for their energy to obtain quantitative results with depth information [199]. For this purpose, 100 nm of $PbCl_2$ and 100 nm of CsCl were evaporated separately for each of the RBS measurements using thermal evaporation. The RBS results are shown below in **Table 6**.

Table 6: *RBS data obtained and calculated densities on 100 nm CsCl and 100 nm PbCl$_2$ evaporated films. It should be noted that the measured density of the thermally deposited layers deviates significantly from the values reported for the respective bulk materials* [200,201].

	[Cs] [mol/cm^3]	[Pb] [mol/cm^3]	[Cl] [mol/cm^3]	density [g/cm^3]	literature density [g/cm^3]
CsCl	0.0076	-	0.0079	1.32	3.99
PbCl$_2$	-	0.0136	0.0276	3.79	5.85

From the RBS data, evaporated PbCl$_2$ has a density of 3.79 g/cm^2, which is only ~ 65% of that reported for bulk material [201]. For evaporated CsCl, the measured density was 1.32 g/cm^2, which represents a deviation from literature value of ~ 33% [200]. The reason for the reduced density of our vapor-deposited coatings can be misordering, inclusions, and possible lattice defects. Looking now at the ratio of [Pb] and [Cs], a factor of 1.79 results, which means that for a 9 nm CsCl layer, 5 nm PbCl$_2$ are sufficient to stoichiometrically form a three-dimensional CsPbCl$_3$ perovskite. Therefore, the PbCl$_2$ layer thickness was reduced to 5 nm and the PL experiment was repeated with a varied CsCl layer thickness (see **Figure 19**).
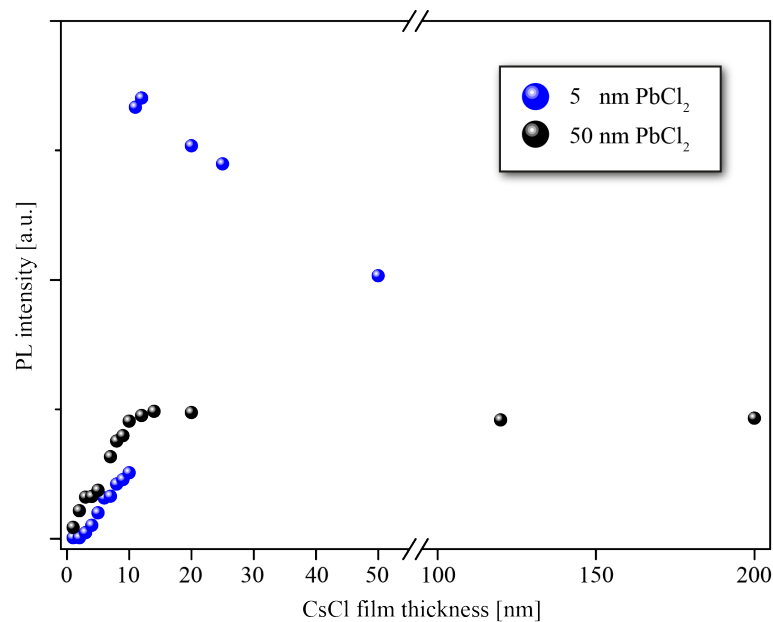
Figure 19: *Shown in blue are the measured PL intensities of the 5 nm PbCl$_2$ samples with increasing CsCl layer thickness. For comparison, the PL intensities of the 50 nm PbCl$_2$ samples are also shown (black dots).*

Again, perovskite formation appears but, a deposition of slightly more than 10 nm CsCl results in a sharp increase of the PL. This can be explained by passivating defects. According to Ye et al. [202], treatment with metal halides significantly improved the photoluminescence quantum

yield (PLQY) of weekly emissive $CsPbCl_3$ nanocrystals (NC). Because $CsPbCl_3$ NCs form deep traps and are highly intolerant of Cl vacancies, which would render them weekly emissive. The PLQY of $CsPbCl_3$ NCs is significantly improved when the defective $PbCl_6$ octahedral coordination is recovered by metal chloride treatment. Thus, although the self-limiting perovskite formation persists up to about 10 nm of CsCl, the further evaporated CsCl is used to passivate the defects present deep in the bandgap of the $CsPbCl_3$ perovskite, which has also been reported in various publications [203–205]. This effect is not seen in the layers evaporated on the 50 nm $PbCl_2$, since here the excess $PbCl_2$ might lead to a higher amount of Cl – vacancies resulting in a possible path for non-radiative recombination [202,206].

Hence, complementary to the photoluminescence studies, Grazing-Incidence Wide-Angle X-ray Scattering (GIWAXS) studies were conducted. Here, the beam of x-rays strikes the layer at a very small angle probing essentially the surface for the sample. It is possible to control the sampling depth by changing the angle of incidence so that the signal from the surface is enhanced at very shallow angles (typically less than 1°). The GIWAXS results of different bilayers from a fixed $PbCl_2$ layer of 5 nm and an increasing CsCl layer are summarized in the following graph (see **Figure 20**).
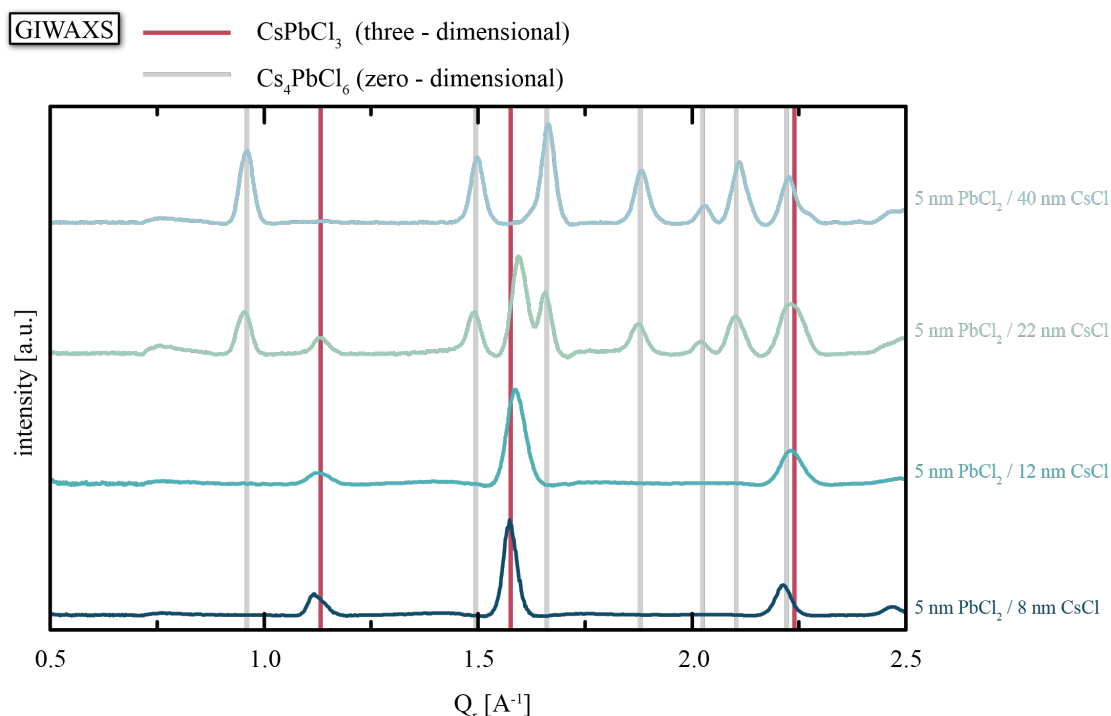
Figure 20: *GIWAXS measurement data of different bilayers from a fixed PbCl₂ layer of 5 nm and a rising CsCl layer to trace the formation or saturation or even transformation of a perovskite layer.*

The GIWAXS measurement on the 5 nm $PbCl_2$ / 8 nm CsCl bilayer shows peaks that are characteristic for a three-dimensional $CsPbCl_3$. To explore the strongly increased photoluminescence intensity with increasing CsCl layer thickness and to track the possible formation of a zero - dimensional Cs_4PbCl_6 perovskite, layers with increased CsCl thickness were analyzed. Pure three - dimensional $CsPbCl_3$ peaks are still exclusively evident for the 5 nm $PbCl_2$ / 12 nm CsCl layer and only a slight increase in intensity compared to the 5 nm $PbCl_2$ / 8 nm CsCl can be seen. On the other hand, if the CsCl layer thickness is further increased to 22 nm and 40 nm, a zero-dimensional Cs_4PbCl_6 perovskite forms and ultimately consumes the previously formed three-dimensional $CsPbCl_3$ perovskite, which explains the decrease in PL intensity (Cs_4PbCl_6 is a wide-gap material with an indirect bandgap). Based on the GIWAXS results, we can assume that the formation of the zero-dimensional Cs_4PbCl_6 perovskite may already have started below 22 nm of CsCl, but its overall thickness was too low to give rise to a notable signal. In any event the cap formed by the wide gap Cs_4PbCl_6 likely affords the passivation of surface defects of the $CsPbCl_3$ and substantially reduce non-radiative recombination, which is then reflected in the dramatic increase of PL intensity for a CsCl thickness > 10 nm.

Based on these results and the understanding of how different $CsCl/PbCl_2$ layer stacks interact as a kind of self-limiting superlattice, the evaporated layers were pressed for recrystallization using the described PHP technique to obtain large crystalline and as flat as possible samples (see **Figure 21**). As in the case of the liquid-processed $CsPbBr_3$ perovskite thin films, low dimensional polymorphs of the chloride-based perovskite were also formed. By varying the thickness of the respective sub-layers, it was possible to produce both zero dimensional and two-dimensional layers. Thus, different multilayer combinations were prepared by thermal evaporation and subsequently recrystallized by planar hot pressing.
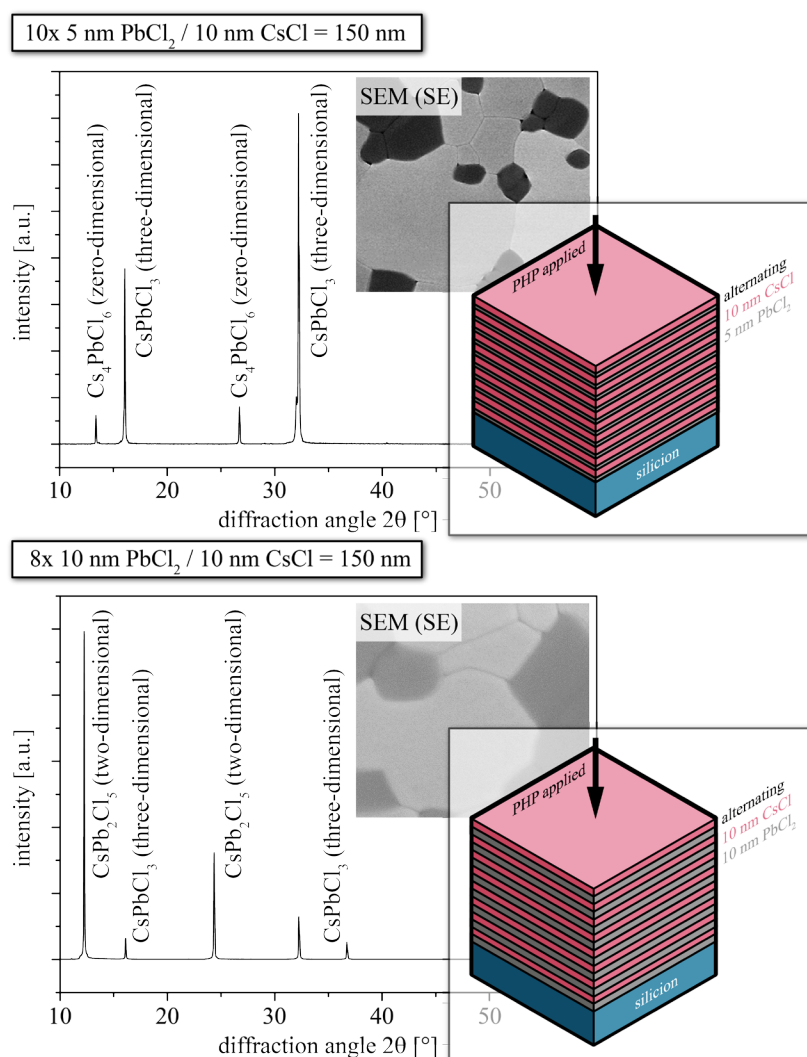
Figure 21: *XRD diffractograms and SEM images of two different multi stacks of thermally evaporated PbCl₂ / CsCl combinations are shown. In the upper part of the figure, the multi stack with the combination of 10x 5 nm PbCl₂ / 10 nm CsCl can be seen, which was subsequently pressed by PHP process. The resulting layer consists of three-dimensional (CsPbBr₃) and zero-dimensional (Cs₄PbCl₆) perovskite due to a CsCl excess. This is also evident from the contrast of the SEM image. The lower combination of 8x 10nm PbCl₂ / 10 nm CsCl, on the other hand, shows both three-dimensional (CsPbBr₃) and two-dimensional (CsPb₂Br₅) perovskite due to the PbCl₂ excess, which can also be distinguished by SEM.*

4.4. Crystal growth of metal halide perovskite semiconductor single crystals

Studies of perovskite single crystals enables to study these materials in a limiting case, which is a step closer to classical semiconductors, which are typically used as single crystals (c.f. Silicon, GaAs). Major activities in this field are focused on single-crystal-based x-ray-detectors [207] and photodetectors [208,209], which show promising performance in terms of sensitivity, response speed, and lowest detectable dose rate. In the future, large-area single crystalline wafers with controlled thickness are expected to become available. Therefore, it is essential to grow high-quality single crystals with the lowest structural and chemical defect densities.

In this regard, the following two fabrication methods are particularly important for the preparation of metal halide perovskite single crystals within this work: the inverse temperature crystallization (ITC) [210] and the antisolvent vapor-assistant crystallization (AVC) [211].

For inverse temperature crystallization (see **Figure 22**) a one-molar PbX_2 salt and AX salt solution is prepared at room temperature, followed by filtering the perovskite solution through a polytetrafluorethylene (PTFE) filter with 0.2 μm pore size into a vial. Keeping the vial in an oil bath, the temperature was slowly increased with 10°C/h from room temperature up to a certain temperature, resulting in a decrease of the solubility of the mixture causing a supersaturated solution and leading to the spontaneous precipitation of crystalline nuclei, that act as seeds for the formation of larger single crystals. Using this ITC method mm-sized single crystals of$MAPbCl_3$, $MAPbBr_3$, and $MAPbI_3$, were produced. The single crystals grown in this way can be harvested from the solution and can also be used as seeds to obtain even larger single crystals.
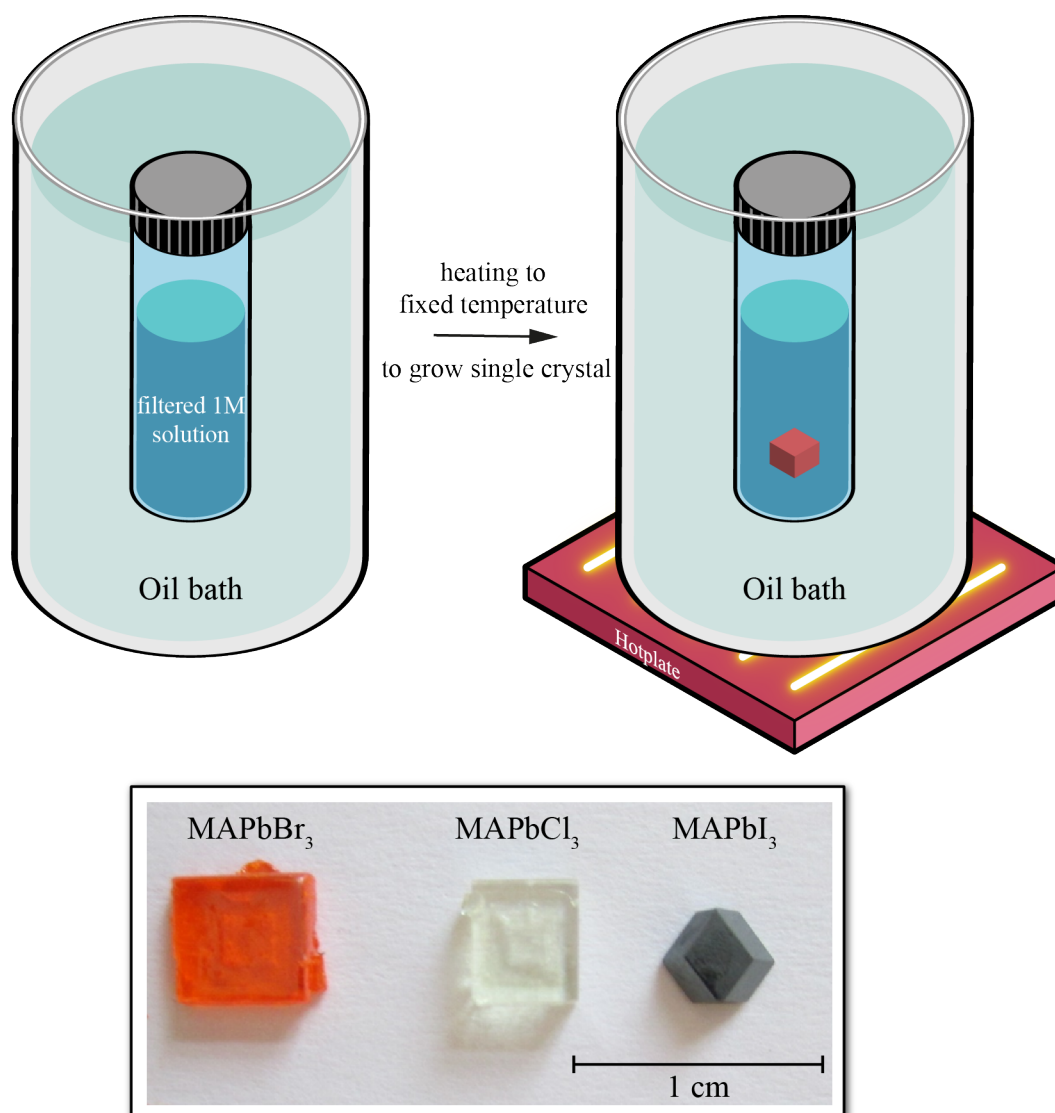
Figure 22: *Single crystal growth process of hybrid metal halide perovskites. Figure showing the crystallization vial immersed in a heating bath as part of the ITC setup. If the solution is heated and held at an elevated temperature for a period of time, crystallization will begin. Edited and based on [210].*

According to the reported antisolvent vapor-assisted crystallization (AVC) method, all-inorganic perovskite single crystals $CsPbBr_3$ and $CsPb_2Br_5$ were prepared (see **Figure 23**) [212]. Here, the decreased solubility of perovskites in the solution mixture results from slow diffusion of the antisolvent into the solution containing the precursor salts. Crystals of $CsPbBr_3$ are grown in methyl alcohol (> 99.5%) and dimethyl sulfoxide (DMSO, > 99.5%) solvents, using CsBr and $PbBr_2$ as precursors. These clear solutions were placed in the inner container, and an antisolvent (MeOH) was placed in the outer container. To form pure $CsPbBr_3$ crystals,

the molar ratios of $PbBr_2$ and CsBr must be between 1 and 1.5. Afterwards the final single crystals were washed with dimethylformamide (DMF) solution. To form pure two-dimensional $CsPb_2Br_5$ single crystals the three-dimensional single crystals are kept longer in the AVC vials. The orange $CsPbBr_3$ perovskite single crystals slowly convert to transparent $CsPb_2Br_5$ perovskite single crystals. According to [50], the excessive amount of $PbBr_2$ results from the low solubility of CsBr in DMSO, which decreases continuously during the MeOH antisolvent diffusion.
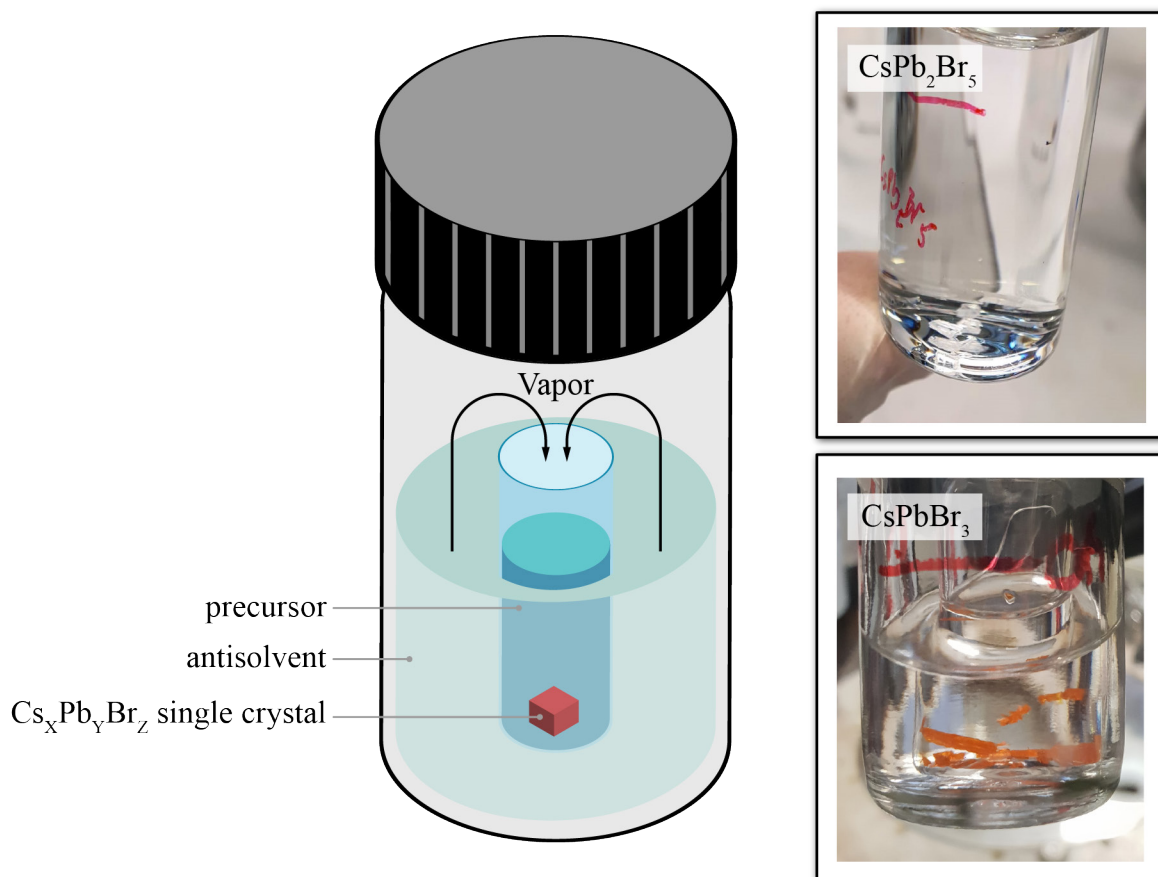
Figure 23: *Shown is the schematic illustration of antisolvent vapor-assisted crystallization. Directly adjacent are the respective products, with the upper transparent/white crystals being the two-dimensional $CsPb_2Br_5$ single crystals and the lower orange single crystals being the three-dimensional $CsPbBr_3$ perovskite crystals [50,213].*

5. Heat transport in metal halide perovskite semiconductors

This chapter deals with the heat transport of metal halide perovskite semiconductors, both in the form of thin films and single crystals. First, the chemical components of 3D metal halide perovskite semiconductors were varied to analyze their influence on the thermal conductivity and to better understand heat transport in metal halide perovskites. In addition, the thermal conductivity, the thermal diffusivity, and the volumetric heat capacity are mapped simultaneously, as all these parameters are of considerable importance in dynamically operated perovskite-based devices. Furthermore, the heat transport of different polymorphs of the perovskite thin films is studied. At the end of the chapter, the results are summarized and discussed.

5.1. Compositional dependence of the thermal conductivity in 3D-polymorph metal halide perovskite semiconductors

At the beginning of this chapter, thermal conductivity measurements of hybrid halide perovskites MAPbX$_3$ (X= I, Br, and Cl) single crystals and their thin-film analogues obtained by the conventional 3ω-SThM technique are presented. The thermal properties were determined on freshly cleaved MAPbX$_3$ single crystals to prevent surface artifacts. The measurements are averaged over a scan area of 5 μm × 5 μm. The investigated planar hot pressed films consist of large crystallites with lateral dimensions on the order of up to 12 μm and a thickness of ~200 nm. Performing SThM within a scan area similar to the area of the large crystallites in the layers, the influence of grain boundaries is negligible. Since the SThM is builtin a SEM, the SThM probe was placed on the cleaved single crystal surface or large single crystallites by using the SEM with low electron beam irradiation doses < 1 μC/cm^2. Measurements, showing the influence of the SEM electron beam on the topography and the thermal conductivity, can be found at the end of this section.

The thermal conductivity of MAPbI$_3$ single crystals was evaluated to be $\lambda_{MAPbI_3}^{cleaved} = 0.34 \pm 0.12\ W\ (m\ K)^{-1}$ at room temperature. The measurement of the average thermal conductivity on the freshly cleaved surface is in good agreement with experimental and theoretical data of around $0.30 - 0.42\ W\ (m\ K)^{-1}$, reported in [105,128]. On the contrary, the thermal conductivity determined for MAPbBr$_3$ single crystals $\lambda_{MAPbBr_3}^{cleaved} = 0.44\ W\ \pm 0.08\ W\ (m\ K)^{-1}$

is higher as that of MAPbI$_3$ (**Figure 24**). The thermal conductivity of the MAPbCl$_3$ single crystal $\lambda_{MAPbCl_3}^{cleaved} = 0.50 \pm 0.05$ W $(m\,K)^{-1}$ is higher compared to that of the Br- and I-based analogues. In this context it should be noted that the determined standard deviations are not due to a limited signal-to-noise ratio of the detecting system but rather due to inhomogeneities of the samples morphology.
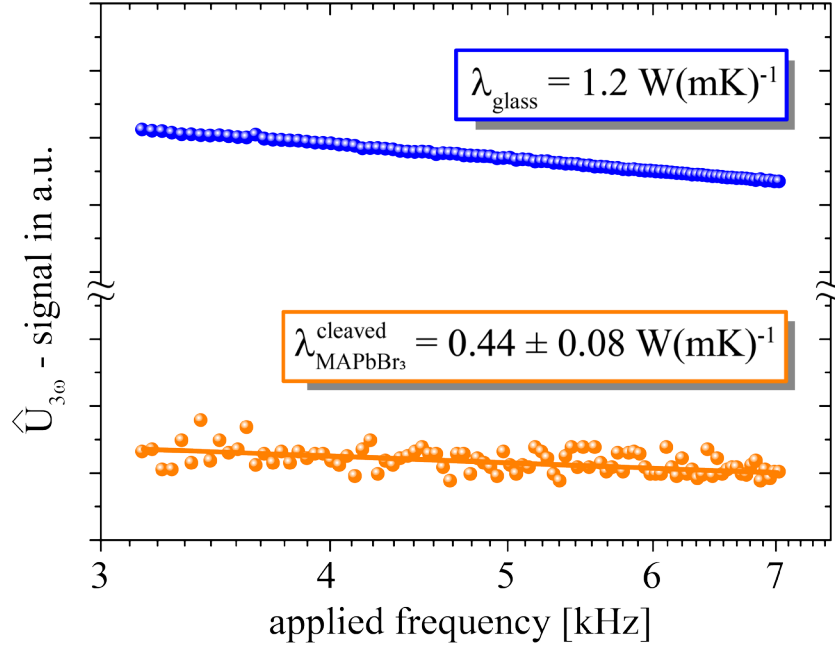
Figure 24: *Determination of the thermal conductivity of a freshly cleaved MAPbBr$_3$ single crystal using glass as reference material. The measured slope of the resulting 3ω component of the voltage drop across the SThM probe Û$_{3ω}$ versus the logarithm of the applied frequency is proportional to the thermal conductivity* [14].

Since most electrical devices are based on thin films, thermal studies were also performed on thin PHP MAPbX$_3$ films. The thermal conductivity of the thin films was found to be $\lambda_{MAPbI_3} = 0.33 \pm 0.12$ W $(m\,K)^{-1}$, $\lambda_{MAPbBr_3} = 0.39 \pm 0.05$ W $(m\,K)^{-1}$, and $\lambda_{MAPbCl_3} = 0.50 \pm 0.12$ W $(m\,K)^{-1}$ [14]. Note, the thermal conductivity is similar to that found in the corresponding freshly cleaved single crystals within its error bars.

Aside from changing the halide anion, the A-site cation of 3D metal halide perovskite semiconductors was varied to analyze their influence on the thermal conductivity and to understand how the heat transport for metal halide perovskites works. Finally, the thermal conductivities obtained for hybrid and all-inorganic perovskites at room temperature are summarized in **Figure 25**.
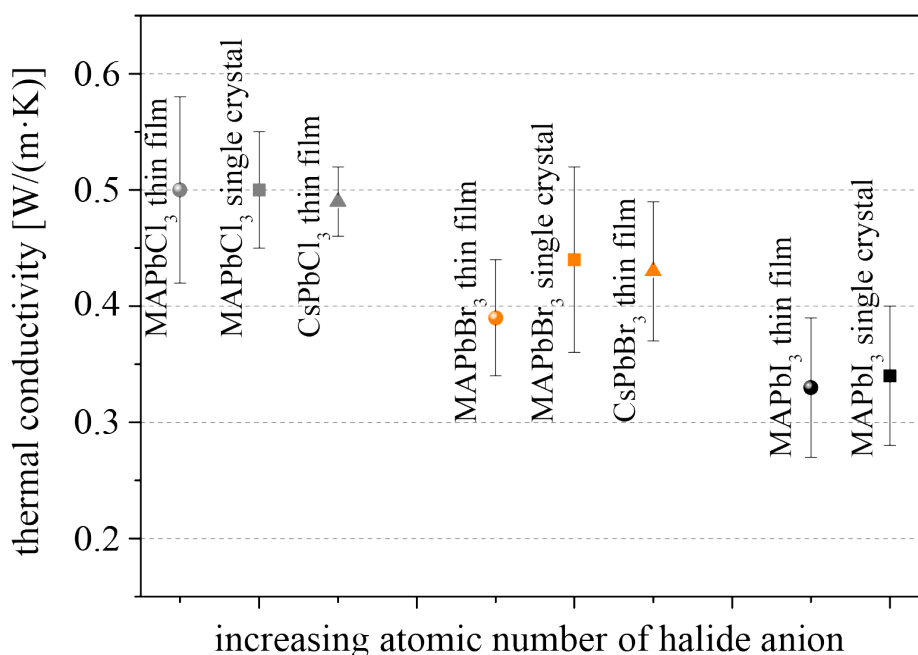
Figure 25: *Thermal conductivities of metal halide perovskite thin films and single crystals found within this work.*

No significant influence of A-site cations on the thermal conductivity is seen, when switching from the hybrid MA-based metal halide perovskites to all-inorganic Cs-based perovskites. On the other hand, there is a dependence between the choice of the halide anion and the heat conduction. The average thermal conductivity of $APbX_3$ increases slightly with decreasing atomic number of the halide. The extent to which the halide anion has an influence on the thermal conductivity will be discussed in the following.

It has already been described that the heat conduction in this material class of metal halide perovskites occurs predominantly via phonons (see 2.4.1. Introduction into heat dissipation in metal halide perovskite semiconductors). The heat capacity c_{phonon}, the mean free path $l_{mfp-phonon}$, and the group velocity (v_{phonon}) of phonons are the key factors contributing to thermal conductivity λ according to the kinetic phonon gas model (see equation 8). Thus, the individual quantities and their influence on the thermal conductivity of the metal halide perovskites are discussed.
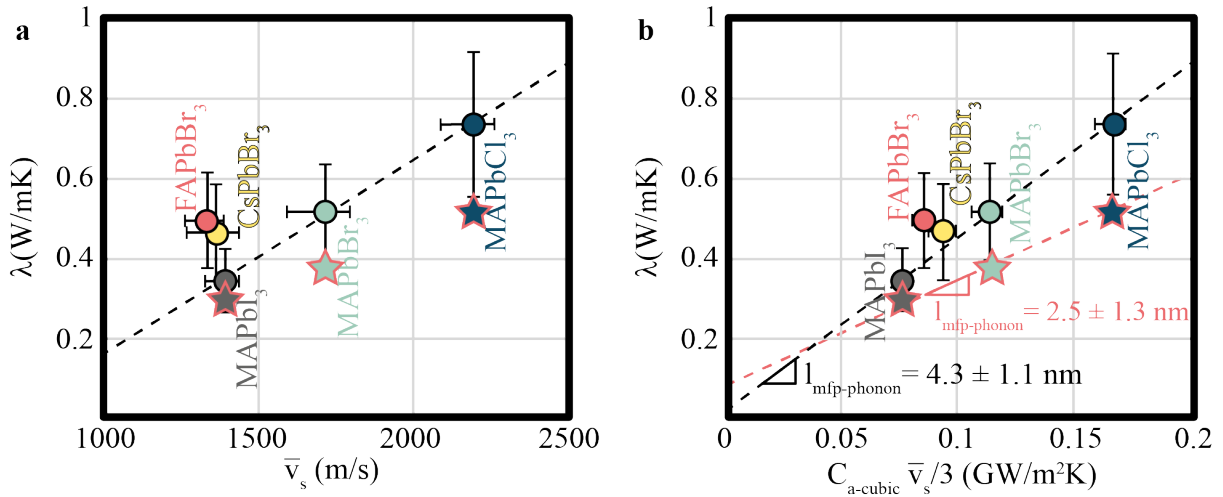
Figure 26: *Figure a) shows the thermal conductivity as a function of sound speed, with a linear dependence for the MA-based metal halide perovskites. Figure b) also shows the thermal conductivity but as a function of $c_{a-cubic} \cdot v_s/3$. The plotted fit also shows a linear dependence, and the slope indicates the mean free path length of the phonons with a length of 4.3 ± 1.1 nm. Both figures and the caption are taken from [95] and have only been adapted to the graphic design of this work. The stars outlined in red show the thermal conductivities measured in this work and are plotted with in this graph and shows by the red dashed line a mean free path length of phonons of 2.5 ± 1.3 nm for the MHPs.*

The group velocity of the acoustic phonons can be approximated by the speed of sound v_s, which in turn depends on the density ρ and the compression modulus K according to

$v_s = \sqrt{\frac{K}{\rho}}$ [88,95,214]. Elbaz et al. showed that the thermal conductivity λ scales linearly with

v_s (see **Figure 26** a)). It is assumed that the increase of the sound velocity happens by an increase of the compression modulus. A decrease in the halide's ionic radius leads to an increase in its electronegativity, resulting in a higher packing density of the perovskite lattice, and stronger Pb-X bonds. Sun et al. [215] examined the mechanical properties of MAPbX$_3$ (X=Cl, Br, I) perovskites using nanoindentation. They found three chemical factors that influence the elastic moduli of MAPbX$_3$: the strength of Pb–X bonds, the relative packing density, and the hydrogen bond interactions. Since hydrogen bonding correlates with electronegativity, they found that

Young's modulus E, which is connected to the stiffness K via the shear modulus, increases with anion electronegativity in the sequence $E_I < E_{Br} < E_{Cl}$. Therefore, a higher K indicates a stiffer perovskite with stronger interatomic bonding, which results in a higher thermal conductivity. The following **Figure 27** is intended to illustrate the increasing stiffness by exchanging the halide anion and should also show the lattice vibration and the associated increase in thermal conductivity based on the ionic radii (see **Table 7**).

increasing stiffness

increasing thermal conductivity

| MAPbX$_3$ | I | Br | Cl |
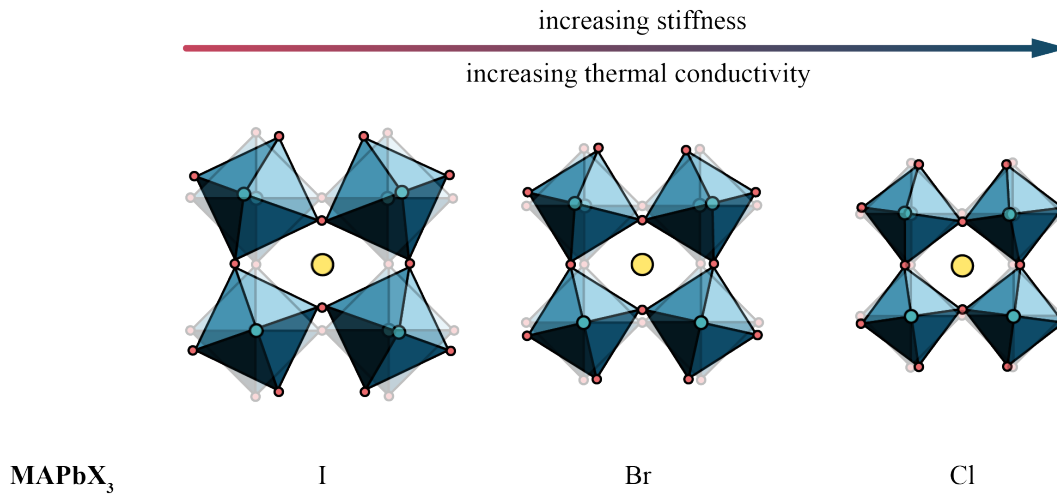
Figure 27: Schematic displacements of octahedras and associated thermal conductivity as a function of halide anions stiffness.

Table 7: Ionic, atomic, and van der Waals radii of I, Br, and Cl [216].

halide atom name	ionic radius [Å]	atomic radius [Å]	van der Waals radius [Å]
I	2.06	1.15	1.98
Br	1.82	0.94	1.85
Cl	1.67	0.79	1.75

The plot of the thermal conductivity versus the product $c_{phonon} \cdot v_{phonon}/3$ shows a linear relationship with a $l_{mfp-phonon}$ of 4.3 ± 1.1 nm (see **Figure 26** b)). The group of Elbaz et al. demonstrated by MDS and thermal conductivity analyses that the mean free path lengths of the phonons in the investigated different metal halide perovskites barely differ [95]. Accordingly, the difference in the measured thermal conductivities is mainly due to the different sound velocities and heat capacities.

A large portion of the phonons responsible for thermal conduction have a mean free path of less than 100 nm, according to theoretical analysis [95,105]. The fact that the scattering at the grain boundary does not affect the thermal conductivity of thin films and single crystals larger than about 100 nm is also shown by the experimentally determined values of the thermal conductivities in **Figure 25**. Introducing nanostructures or crystallites with lateral dimensions below 100 nm is expected to give rise to substantial phonon scattering.

Methylammonium lead halide perovskites are frequently inspected by scanning electron microscopy (SEM) and other techniques based on electron irradiation, e.g. cathodoluminescence (CL) [217–219]. Thus, the thermal conductivity of the freshly cleaved MAPbBr$_3$ single crystal was inspected after irradiating the sample with varied electron beam irradiation doses. We have found that electron beam induced degradation leads to significantly higher thermal conductivity than ambient degradation, where the perovskite decomposes [129].

In the first measurement, the sample was selectively exposed to an electron beam with a dose of 15 µC/cm² at an acceleration voltage of 20 kV. An increase of the thermal conductivity to $\lambda_{MAPbBr_3}^{15\,\mu C/cm^2} = 0.7 \pm 0.3\ W(m\,K)^{-1}$ is found after electron beam irradiation. The thermal conductivity further increased up to $\lambda_{MAPbBr_3}^{144\,\mu C/cm^2} = 7.6 \pm 1.2\ W(m\,K)^{-1}$, which is $>$ 17 times larger than that of the freshly cleaved sample, by increasing the irradiation dose up to 144 µC/cm². The resulting changes in the thermal conductivities of MAPbCl$_3$ and MAPbI$_3$ after electron beam irradiation were evaluated to be $\lambda_{MAPbCl_3}^{144\,\mu C/cm^2} = 8.3 \pm 0.2\ W(m\,K)^{-1}$ and $\lambda_{MAPbI_3}^{144\,\mu C/cm^2} = 3.7 \pm 0.2\ W(m\,K)^{-1}$ of the same order of magnitude at room temperature. Higher deviations due to inhomogeneities of the thermal conductivity of a electron beam induced degraded sample are detected as can been seen in the following **Figure 28**. A similar effect was found for samples stored in air for several hours [139].

To better understand the impact of electron irradiation, complementary energy dispersive x- ray (EDX) analyses were carried out. In EDX measurements the atomic relation of Br:Pb decreased exponentially during the measurement from 3:1 down to 2.1:1, leaving more Pb behind and resulting in increased thermal conductivity. It has been shown that it is even possible to evaporate part of the perovskite by electron beam bombardment [10].
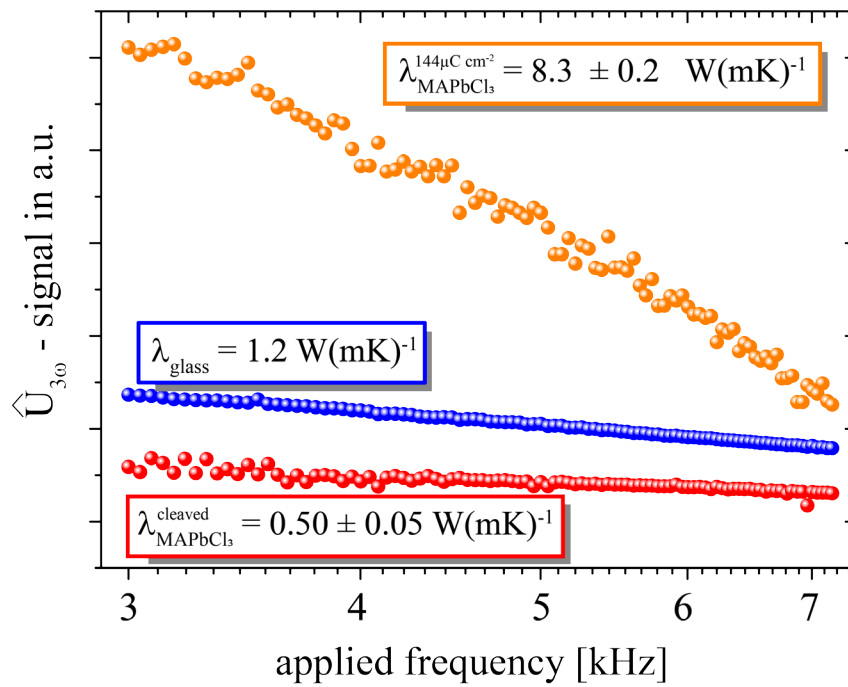
Figure 28: *Increase of the thermal conductivity on a MAPbCl₃ single crystal before and after electron beam irradiation. The thermal conductivity of glass is used here as a reference measurement.*

5.2. Simultaneous mapping of thermal conductivity, thermal diffusivity, and volumetric heat capacity in metal halide perovskite semiconductors

Aside from the measurement of thermal conductivity studies of thermal diffusivity and heat capacity on halide perovskite films were entirely missing, as can be seen in **Table 3**. Thus, using the advanced SThM for this set of experiments (see 3.2. Development of a measurement technique for simultaneous mapping of thermal conductivity, thermal diffusivity, and volumetric heat capacity), the local temperature oscillations $\hat{T}_{probe}(\vec{r})|_{7kHz}$ and $\hat{T}_{probe}(\vec{r})|_{3kHz}$ were detected simultaneously. This technique allows the mapping of the thermal conductivity of our perovskite films in the frequency domain (**Figure 29**).
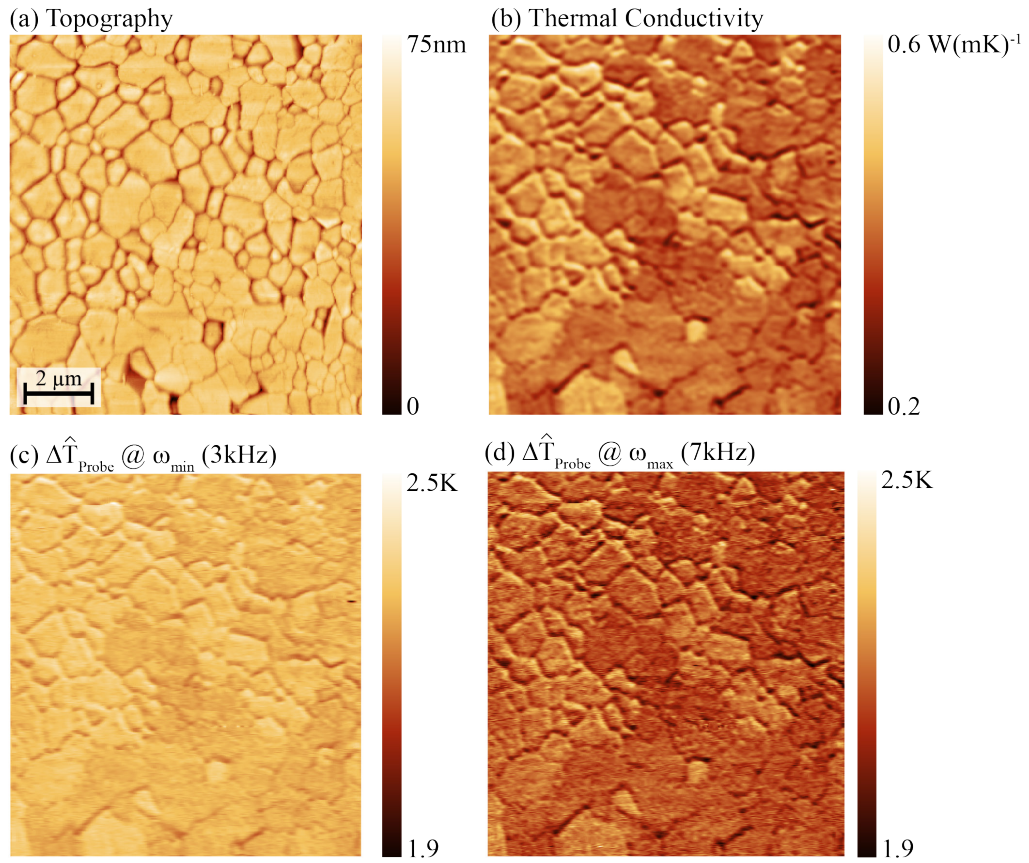
Figure 29: *(a) Topography, corresponding temperature oscillations (c, d) and resulting mapping of the thermal conductivity (b) of recrystallized planar hot pressed $Cs_XPb_YBr_Z$ perovskite thin film.*

From these measurements, which are independent of the local film temperature, the absolute value of $\widehat{T}_{probe}$ is between 1.9 and 2.5 K, because only a small amount of heat is released to the film. Slight variations of $\widehat{T}_{probe}$ at 3 kHz and at 7 kHz result in a contrast between the different grains in these images. Since $\widehat{P}_{el.}$ is constant and the AFM control keeps the thermal contact consistent, these variations are explainable either by a different thermal conductivity or by changes in thermal diffusivity between the grains. To determine the low thermal conductivity in perovskite thin films with high spatial resolution using the 3ω- technique, we subtracted the local temperature variations $\widehat{T}_{probe}(\vec{r})\big|_{7kHz}$ from $\widehat{T}_{probe}(\vec{r})\big|_{3kHz}$. This technique allows the mapping of the thermal conductivity of our perovskite films in the frequency domain since the resulting difference is independent of $a(\vec{r})$.

Correlating our SThM data with the insights gained from SEM/EBSD, one can attribute thermal conductivities of 0.43 ± 0.03 W $(m\,K)^{-1}$ and 0.33 ± 0.02 W $(m\,K)^{-1}$ to the 3D phase (CsPbBr$_3$) and the 2D phase (CsPb$_2$Br$_5$), respectively. Aside from the thermal conductivity, the local thermal diffusivity $a = \dfrac{\lambda}{C_{vol}} = \dfrac{\lambda}{\rho \cdot C_{spec}}$ is of great importance. A thermal diffusivity of 0.3 mm²/s was determined as an average for the cesium lead bromide layers. The uncertainty in the absolute value of about ± 0.1 mm²/s is high, since $a(\vec{r})$ depends exponentially on $\widehat{T}_{probe}$ as well as on $1/\lambda(\vec{r})$. Nevertheless, even slight differences in $\Delta a(\vec{r})$ of 0.02 ± 0.01 mm²/s can be detected from the differences in the temperature oscillation $\Delta\widehat{T}_{probe}(\vec{r})\big|_{3kHz}$ and the variations of the thermal conductivity $\Delta\lambda(\vec{r})$, as illustrated in **Figure 30**.
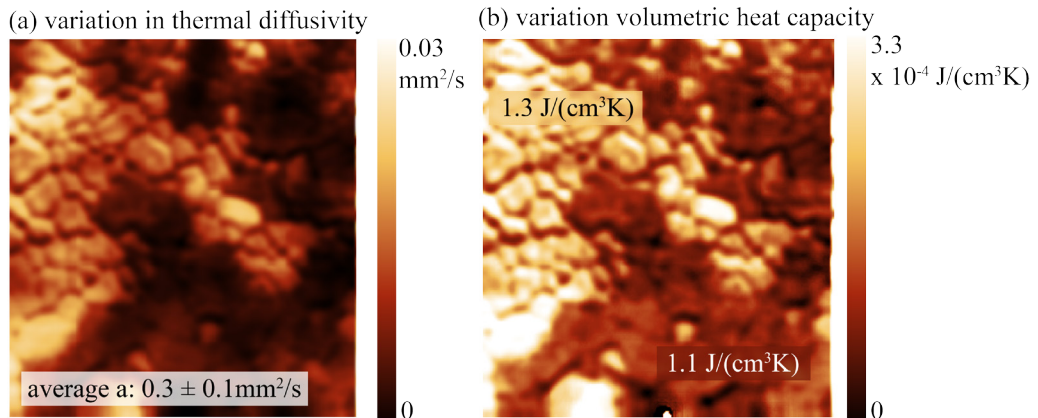
Figure 30: (a) shows the variation of the thermal diffusivity over the measured area. In average the thermal diffusivity of 0.3 ± 0.1 mm²/s is detected for the Cs$_X$Pb$_Y$Br$_Z$ perovskite thin film. Only slight differences are detected. (b) Local variations of the volumetric heat capacity of the perovskite thin film.

In particular, the local heat capacity is of interest, since it ultimately tells the ability to store the supplied heat, and local variations can even lead to discontinuous temperature gradients in

dynamically operated electrical systems [175]. Since the crystal structure of $CsPbBr_3$ is isotropic, the local volumetric heat capacity of the corresponding film, which is given by the product of the local density ρ_{CsPbBr_3} and the local specific heat c_{CsPbBr_3}, can be directly determined from the SThM data. An average volumetric heat capacity of $c_{vol}^{CsPbBr_3} = 1.3 \pm 0.4\,J(cm^3 \cdot K)^{-1}$ resulted for the 3D regions of the $CsPbBr_3$ perovskite film. Since only slight differences are found in the local thermal diffusivity $a(\vec{r})$ of 2D and 3D cesium lead bromide, variations in $\rho(\vec{r}) \cdot c(\vec{r})$ are mainly due to the local variation of the thermal conductivity $\lambda(\vec{r})$. Accordingly, the volumetric heat capacity for the 2D regions of the perovskite film was determined to be $c_{vol}^{CsPb_2Br_5} = 1.1 \pm 0.3\,J(cm^3 \cdot K)^{-1}$. The corresponding specific heat capacities $c_{spec}^{CsPbBr_3} = 0.29 \pm 0.9\,J(g \cdot K)^{-1}$ and $c_{spec}^{CsPb_2Br_5} = 0.18 \pm 0.6\,J(g \cdot K)^{-1}$ were calculated by taking the mass densities $\rho_{CsPbBr_3} = 4.55\,g \cdot cm^{-3}$ and $\rho_{CsPb_2Br_5} = 5.85\,g \cdot cm^{-3}$ into account [213,220]. The revealed ultralow heat capacities for Cs-based perovskites, which are on the same level as those of typical metals, are of the same order of magnitude as the previously reported values for MA-based single crystals determined by calorimetric techniques [120].

Figure 31 shows the simultaneously measured thermal properties, thermal conductivity $\lambda(\vec{r})$, thermal diffusivity $a(\vec{r})$ and volumetric heat capacity $c_{vol}(\vec{r})$ of a $Cs_xPb_yCl_z$ perovskite thin film. In addition, a secondary electron image from the scanning electron microscope is included to map the 0D- and 3D-polymorphs Cs_4PbCl_6 and $CsPbCl_3$ present here. Correlating our SThM data with the insights gained from XRD/SEM, one can attribute the thermal conductivities of $\lambda_{CsPbCl_3} = 0.49 \pm 0.04\,W\,(m\,K)^{-1}$ and $\lambda_{Cs_4PbCl_6} = 0.30 \pm 0.03\,W\,(m\,K)^{-1}$ to the 3D phase ($CsPbCl_3$) and the 0D phase (Cs_4PbCl_6), respectively. The thermal conductivity of $CsPbCl_3$ is found to be very similar to that found for $MAPbCl_3$ ($0.50\,W\,(m\,K)^{-1}$) at room temperature [14]. On the other hand, the significantly lower thermal conductivity found for Cs_4PbCl_6 agrees well with the findings obtained from phonon band structure calculations on 0D perovskites [221], which reveal low group velocities and localization of vibrational energy in these grains.

Aside from the thermal conductivity, an average thermal diffusivity of $0.5 \pm 0.1\,mm^2 s^{-1}$ was determined for the cesium lead chloride layers using the measured $\Delta\hat{T}_{probe}(\vec{r})\big|_{3kHz}$ and the determined thermal conductivity $\lambda(\vec{r})$ [179] for the whole film. This value for $a(\vec{r})$ is in good agreement to the results obtained for $CsPbCl_3$ single crystals using transient methods [117]. Again, the uncertainty in the absolute value is relatively high because $a(\vec{r})$ depends

exponentially on $\Delta\hat{T}_{probe}(\vec{r})\big|_{3kHz}$ as well as on $\frac{1}{\lambda(\vec{r})}$. Nevertheless, only minor local variations of $a(\vec{r})$ (i.e. $\Delta a(\vec{r})$) of about 0.05 ± 0.01 mm$^2 s^{-1}$ occur. Note, the thermal diffusivity for CsPbCl$_3$ and large Cs$_4$PbCl$_6$ crystallites is also found to be very similar. Moreover, only a small contrast appears at the grain boundaries as well as in smaller grains of Cs$_4$PbCl$_6$ perovskites, which might be explained by a higher density of structural defects. In this context, it must be noted that, experimental studies of thermal properties on 0D Cs$_4$PbCl$_6$ perovskites were not reported in the literature before.

(a) SEM - Image

(b) Topography

75 nm

2 µm

2 µm

0

(c) Thermal Conductivity

0.6 W(mK)$^{-1}$

0.30 W(mK)$^{-1}$

0.49 W(mK)$^{-1}$

0.2

(d) Δ in thermal Diffusivity

0.06 mm^{2}s^{-1}

0

(e) Volumetric heat capacity

1.1 J(cm^{3}K)$^{-1}$

0.5 J(cm^{3}K)$^{-1}$

0.9 J(cm^{3}K)$^{-1}$

0.3

(f) Δ in volumetric heat capacity

3.4 x10^{-4} J(cm^{3}K)$^{-1}$

0
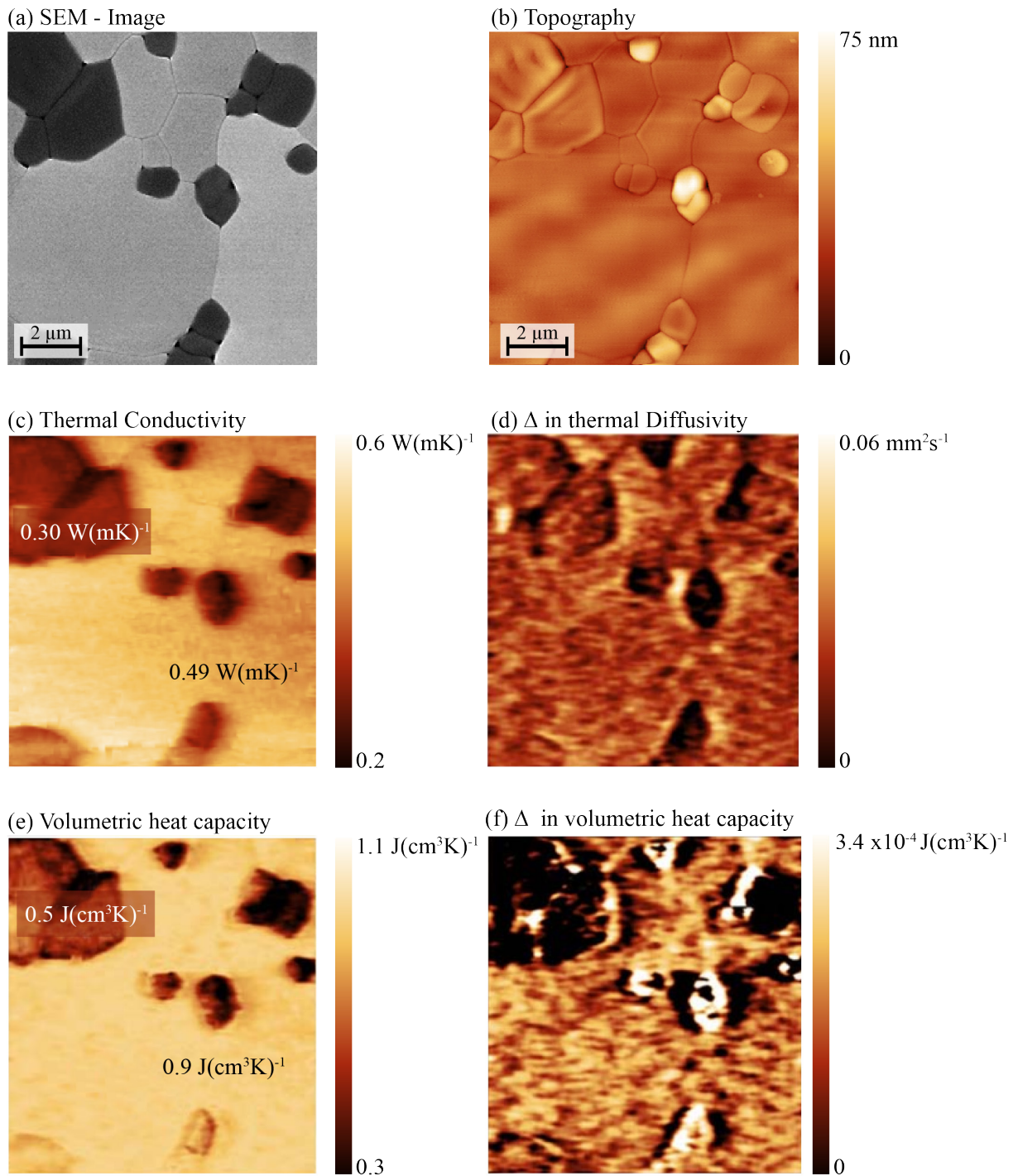
Figure 31: *Backscattered scanning electron microscope image (a) with corresponding topography image (b), and thermal conductivity (c) distribution obtained on a Cs$_x$Pb$_y$Cl$_z$ perovskite thin film. Microscopy images are 10 × 10 µm^2. Only slight differences in the variation of the thermal diffusivity are detected for CsPbCl$_3$ and Cs$_4$PbCl$_6$ in (d). The image (e) shows the local variations of the volumetric heat capacity. The deviation of the volumetric heat capacity in (f) varies significantly within Cs$_4$PbCl$_6$ grains and at their boundaries.*

Assuming isotropic heat transport as the most simple approximation, an average volumetric heat capacity of $c_{vol}^{CsPbCl_3} = 0.9 \pm 0.1\,J(cm^3 \cdot K)^{-1}$ and $c_{vol}^{Cs_4PbCl_6} = 0.5 \pm 0.2\,J(cm^3 \cdot K)^{-1}$ results for the 3D and 0D regions of the perovskite film, respectively. The corresponding specific heat capacities $c_{spec}^{CsPbCl_3} = 0.22 \pm 0.07\,J(g \cdot K)^{-1}$ and $c_{spec}^{Cs_4PbCl_6} = 0.15 \pm 0.08\,J(g \cdot K)^{-1}$ were determined by taking the mass densities of $\rho_{CsPbCl_3} = 4.24\,g \cdot cm^{-3}$ [222] and $\rho_{Cs_4PbCl_6} = 3.28\,g \cdot cm^{-3}$ [223] into account. Note, earlier studies using a pulse transient technique found significantly higher values of $c_{spec}^{CsPbCl_3} = 0.27\,J(g \cdot K)^{-1}$ to $> 0.35\,J(g \cdot K)^{-1}$ [117,224]. The specific heat capacity of CsPbCl$_3$ in the monoclinic phase is smaller than that of CsPbBr$_3$ thin films in the orthorhombic structure due to the increased stiffness, whose thermal studies in terms of thermal diffusivity and heat capacity are presented in the chapter 6.

It is important to note, that both the density and the heat capacity may significantly differ due to local internal stress. Hence, the local variation of the volumetric heat capacity $\Delta c_{vol}(\vec{r}) = \Delta\lambda(\vec{r})/\Delta a(\vec{r})$ is evaluated to clarify inhomogeneities within the grains. As can be seen from **Figure 31**, $\Delta c_{vol}(\vec{r})$ is four orders of magnitude less than $c_{vol}(\vec{r})$ in the films, indicating that effects like stress etc. are negligible. However, the highest variations are found at the grain boundaries as well as for small grains of 0D, while the contrast and thus $\Delta c_{vol}(\vec{r})$ is low in the larger 0D regions. A possible explanation for the local deviation of the volumetric heat capacity near the grain boundaries may be lattice defects.

5.3. 0D- and 2D-polymorphs of all-inorganic metal halide perovskites

As predicted in the review article by Cao et al., low-dimensional metal-halide perovskites may be useful for a wide range of applications, such as LEDs, solar cells, lasers, photodetectors and stimuli-responsive devices [41]. The incorporation of these low-dimensional perovskites has been shown to improve the optical properties and stability of devices, such as all-inorganic 0D/3D mixed dimensional perovskite solar cells [39,40]. Although the thermal properties of these 0D and 2D perovskites can differ significantly from their 3D analogues, as of yet, only a few studies have been carried out to assess heat transport in low-dimensional perovskites (including this work) [101,109,179,221]. An ultralow thermal conductivity of $0.15 \, W \, (m \, K)^{-1}$ was discovered in 0D hybrid lead-free $[Mn(C_2H_6OS)_6]I_4$ single crystals at room temperature; it was further decreased by introducing disorder into the system [221]. Furthermore, the thermal conductivities of 2D hybrid perovskites could be varied in a range from 0.10 to $0.19 \, W \, (m \, K)^{-1}$ depending on the molecular structure of the bulky cation [109]. The extremely low thermal conductivities can be attributed to the crystalline substructure of these perovskites. In a similar sense, substantially reduced thermal conductivities have been discussed for layered, 2D thermoelectric materials [225]. The reduced thermal conductivity has been explained by increasingly glass-like properties, which hamper phonon propagation. It was found that the thermal conductivities of these perovskite films, due to the anisotropy of the crystalline structure, are significantly dictated by their relative orientation (see **Figure 32**). For our thermal investigations, we assumed random oriented 2D perovskite with isotropic thermal conductivities as approximation to get further insights into the heat transport in MHPs. The results presented so far suggest that organic based low-dimensional perovskites provide a unique opportunity to achieve ultralow thermal conductivity, which would be beneficial for thermo-electric applications.
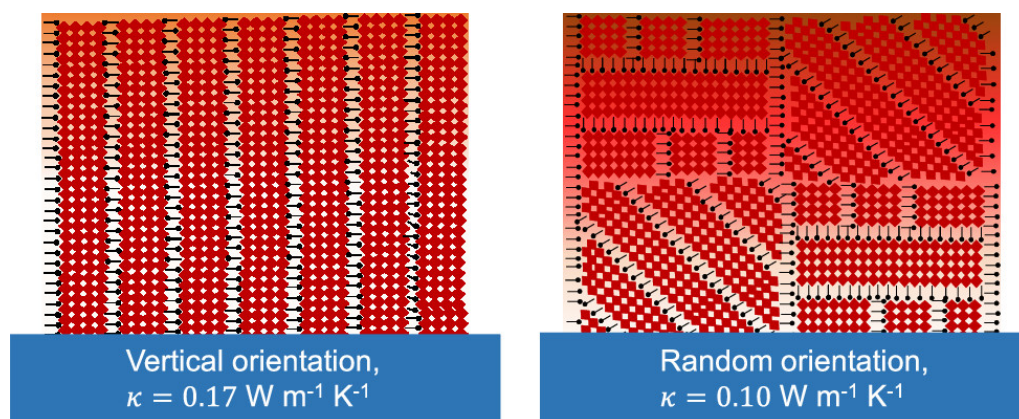
Figure 32: *Schematic illustrations of vertically and randomly oriented $BA_2MA_3Pb_4I_{13}$ crystal orientations that lead to different thermal conductivities* [109].

For all-inorganic perovskites, such as cesium lead chloride, it was found that the thermal conductivities as well as volumetric heat capacities become smaller with reduced dimensionality [179,226]. Note, that the thermal diffusivities, which are responsible for the dynamic heat transfer in devices, remain almost constant within the measurement uncertainties. In another example, 2D phase $CsPb_2Br_5$ films show a low thermal conductivity which are drastically lower than those of their 3D counterparts, which is shown in **Figure 33** with a high resolution.
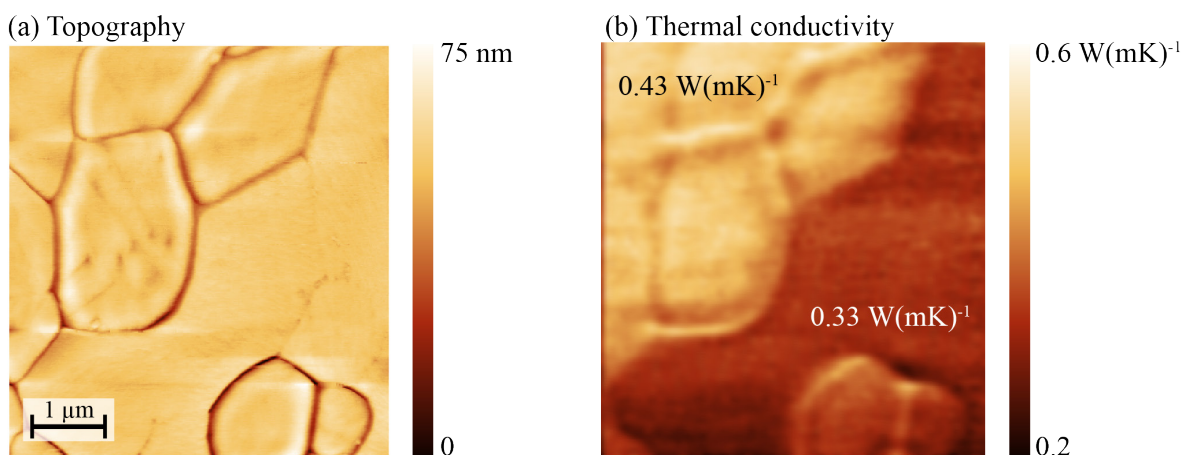
Figure 33: *High laterally resolved thermal conductivity mapping on a flattend $Cs_XPb_YBr_Z$ film indicating a higher thermal conductivity of 3D-polymorph ($CsPbBr_3$) and lower thermal conductivity of 2D-polymorph ($CsPb_2Br_5$).*

Importantly, as a result of correlating EBSD and scanning electron microscopy (SEM) (as shown in **Figure 16**), we confirm that the 2D phase appears substantially brighter in SEM compared to the 3D phase. And since the SThM is a hybrid system and is built into an SEM, the tip and accompanying thermal measurements can be correlated with the contrast-rich SEM images (**Figure 34**).
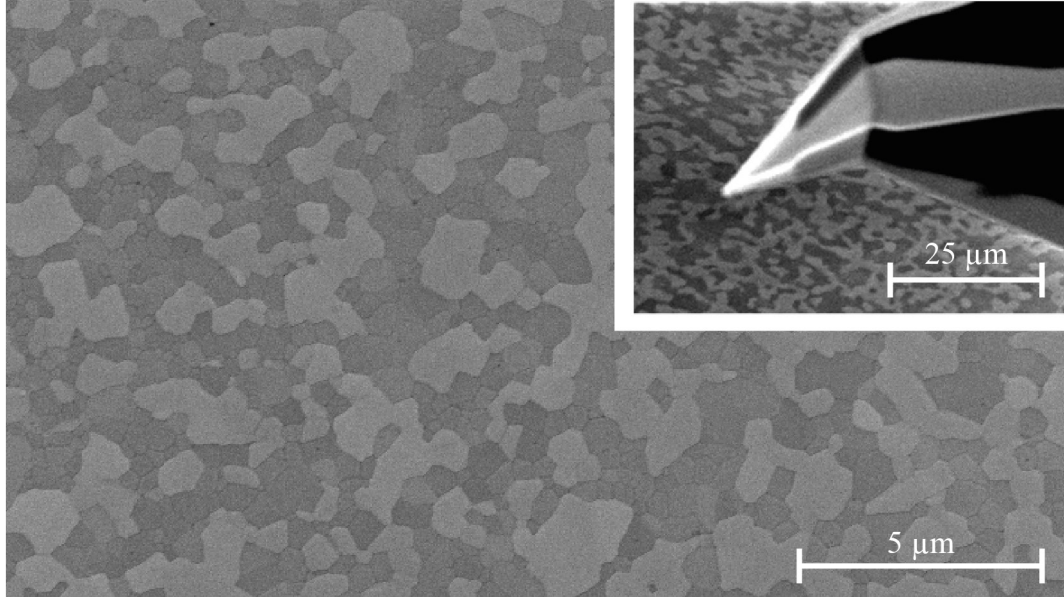
Figure 34: *SEM Image of CsxPbyBrz and additional with the SThM tip.*

In addition, via the fabrication method of the CsPbCl$_3$ thin films, the stoichometry was adjusted so that the two-dimensional polymorphs of the inorganic Cl-based thin films could also be fabricated and examined for their thermal properties. Thus, for the two-dimensional polymorphic perovskite structure CsPb$_2$Cl$_5$, a value of $\lambda_{\text{CsPb}_2\text{Cl}_5} = 0.40 \pm 0.02 \, \text{W} \, (m \, K)^{-1}$ for the thermal conductivity, a value of $a_{\text{CsPb}_2\text{Cl}_5} = 0.6 \pm 0.1 \, \text{mm}^2 s^{-1}$ for the thermal diffusivity and a value of $c_{vol}^{\text{CsPb}_2\text{Cl}_5} = 0.7 \pm 0.2 \, J(cm^3 \cdot K)^{-1}$ for the volumetric heat capacity were determined.

5.4. Concluding remarks with strategies to enhance the thermal properties in perovskite devices

The thermal conductivities as well as volumetric heat capacities become smaller, the lower the dimensionality of the respective polymorph. The following table shows the measured MHPs as an overview.

Table 8: *Summary of the measured thermal properties of the metal halide perovskites in the form of thin films and single crystals.*

metal halide perovskite thin film	λ [W $(m\ K)^{-1}$]	a [$mm^2 s^{-1}$]	c_{vol} [$J(cm^3 \cdot K)^{-1}$]	metal halide perovskite single crystal	λ [W $(m\ K)^{-1}$]
MAPbI$_3$	0.33 ± 0.12			**MAPbI$_3$**	0.34 ± 0.12
MAPbBr$_3$	0.39 ± 0.05			**MAPbBr$_3$**	0.44 ± 0.08
MAPbCl$_3$	0.50 ± 0.12			**MAPbCl$_3$**	0.50 ± 0.05
Cs$_x$Pb$_y$Cl$_z$					
3D-polymorph CsPbCl$_3$	0.49 ± 0.04	0.5 ± 0.1	0.9 ± 0.1		
2D-polymorph CsPb$_2$Cl$_5$	0.40 ± 0.04	0.6 ± 0.1	0.7 ± 0.1		
0D-polymorph Cs$_4$PbCl$_6$	0.30 ± 0.03	0.5 ± 0.1	0.5 ± 0.1		
Cs$_x$Pb$_y$Br$_z$					
3D-polymorph CsPbBr$_3$	0.43 ± 0.03	0.3 ± 0.1	1.3 ± 0.4	**3D-polymorph CsPbBr$_3$**	0.44 ± 0.02
2D-polymorph CsPb$_2$Br$_5$	0.33 ± 0.02	0.3 ± 0.1	1.1 ± 0.3	**2D-polymorph CsPb$_2$Br$_5$**	0.32 ± 0.01

In this thesis, only the influence of the A site cation and halide anion has been considered. Changing the B-site metal has only been examined in a limited number of thermal conductivity studies, so more work is needed to clarify its influence. However, MASnI$_3$ exhibits a very low thermal conductivity at room temperature below 0.09 W $(m\ K)^{-1}$ in experimental work [125]. A first principle calculation of the double perovskites Cs$_2$AgBiCl$_6$ and Cs$_2$AgBiBr$_6$ also yielded very low λ for these materials, 0.078 and 0.065 W $(m\ K)^{-1}$, respectively [227]. However, these double perovskites have so far only been calculated and no experimental investigations have been carried out [228]. Double perovskite materials are expected to have high total thermal conductivity (50–70 W $(m\ K)^{-1}$ at 300 K) due to their electronic contribution. They are also predicted to have high electrical conductivity because of their high λ value. However, recent experiments have shown that Cs$_2$AgBiBr$_6$ has unexpectedly low electrical conductivity and is highly resistive [229]. Further computational and experimental investigations are needed to clarify the nature of this large discrepancy. As a result of its high intrinsic anharmonicity and low group velocity, the simulated thermal conductivity for double halide perovskites, Cs$_2$InAgCl$_6$, was 0.2 W $(m\ K)^{-1}$ at room temperature [230].

A dimensionality-controlled surface passivation for enhancing the performance and stability of perovskite solar cells has been pointed out recently [231]. Note that in metal-halide perovskites the thermal properties of 0D and 2D materials differ significantly from those of the bulk (3D). To combine charge transport and chemical protection in one, great efforts have also been made to produce functional layers with optimized optical, electrical and permeation barrier properties [232]. Brinkmann et al. demonstrated that introducing a bi-layered electron-extraction interlayer consisting of aluminum-doped zinc oxide nano-particles and tin oxide, grown by low temperature atomic layer deposition (ALD), can significantly mitigate the decomposition of the perovskite in inverted perovskite solar cells even at elevated temperatures [233,234]. It should be noted that in this example the ALD-grown tin oxide formed an outstandingly dense permeation barrier. The reduction of thermally induced stress and strain in films is also an important issue that should be addressed for the reliability of perovskite devices. Unfortunately, only a few studies have been carried out so far. Rolston et al. studied mechanical stresses that develop during the fabrication of perovskite films and a direct relationship between film stress and stability in both perovskite films and solar cells was determined [235]. They developed simple strategies to reduce the stress and to improve the inherent moisture and thermal stability of perovskite films, e.g., by using low process temperatures, using polymeric substrates with thermal expansion coefficients that are closer to those of the perovskites, and pre-straining the substrate during perovskite processing. Otherwise highly textured morphologies are created by popular anti-solvent conversion methods due to in-plane compressive stress [236]. The energy release leads to wrinkling during the intermediate phase of film formation, in which the substrate constrains the film from expanding. Ultra- smooth films can be obtained by slowing the rate of film formation since the extent of wrinkling is correlated with the rate of film conversion. The regulation of strain in perovskite thin films by suitable selection of charge transport layers (CTLs) was also reported (**Figure 35**) [237]. Tensile strains in perovskite films were compensated for by transport layers with high thermal expansion coefficients and by elevating the processing temperature. Note that thermal effects can also impact other functional layers in perovskite devices, such as CTLs and electrodes.
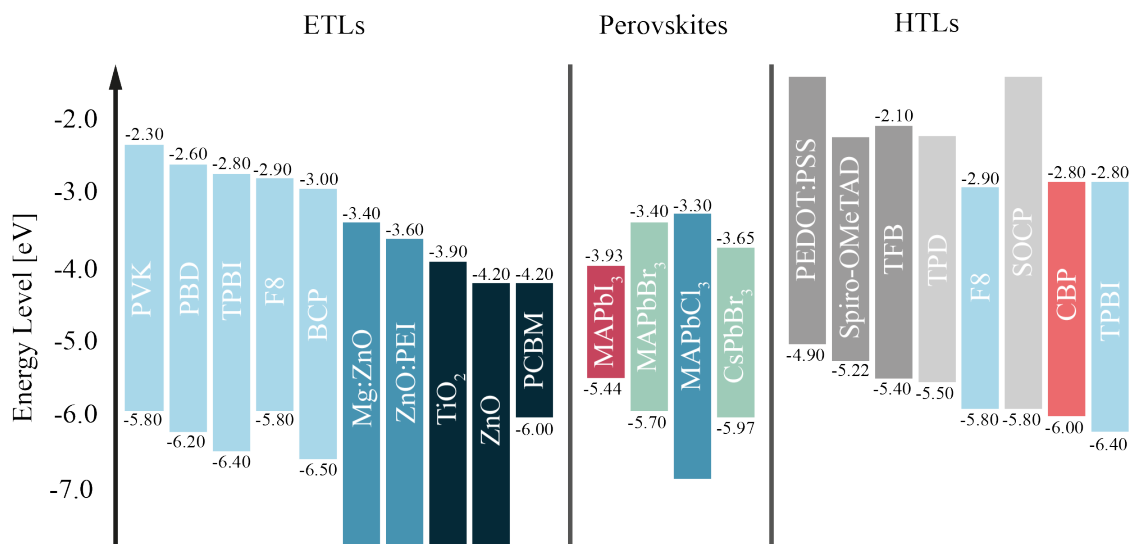
Figure 35: *Energy level alignment of various materials used as ETLs and HTLs in perovskite devices. Based on and edited from* [238].

The extensive studies on their thermally enhanced chemical decompositions and strategies for their stabilization are reviewed in the article by Ava et al. [51]. For example, metal electrodes, which might contribute to thermal management, can be degraded by the corrosive decomposition products of the perovskite. These layers must therefore also be protected. This is even the more problematic for some semi-transparent solar cells, in which the semi-transparent electrodes are based on ultrathin metal films. Thus, a self-encapsulating thermostable and air-resilient electrically conductive permeation barrier was realized by ultrathin Ag layer between SnO_x grown by low-temperature atomic layer deposition [239]. These additional layers further complicate the design of components in terms of mechanical stability. The efforts to increase the energy of fracture of perovskite solar cells were compiled by Boyd et al. [240].

Although recent review articles discuss factors affecting the chemical and mechanical stability of perovskite solar cells as well as current issues and new strategies to improve material and device stability [241,242], concepts for improved heat management in perovskite devices are still in their infancy. It must be ensured that the other important layers within the devices can dissipate the heat because perovskites have a very low thermal conductivity. For example, in addition to a low coefficient of thermal expansion of $5 \cdot 10^{-6} K^{-1}$, glass has likewise a very low thermal conductivity of approximately $1\ W \cdot (m\ K)^{-1}$ and a very low specific heat capacity in the range of $0.8\ J\ (g\ K)^{-1}$. Thus, in the case where glass is used as a substrate, heat

dissipation into the substrate is hampered [243]. The commonly used transparent electrode material indium tin oxide (ITO) is degenerately doped (carrier density $> 1 \cdot 10^{-20} cm^{-3}$) and behaves like a metal [244]. Nevertheless, the resulting in-plane heat transport in the ITO layer is strongly limited by its $\lambda_{ITO} = 6\, W \cdot (m\, K)^{-1}$ and a typically small film thickness of around 150 nm. In addition, it must also be noted that organic-based ETLs and HTLs, which are depicted in Fig. 11, have likewise ultra-low thermal conductivities ($\lambda_{PCBM} = 0.031\, W \cdot (m\, K)^{-1}$), and are highly anisotropic for the in-plane and out-of-plane directions ($\lambda_{PEDOT:PSS\parallel} = 1\, W \cdot (m\, K)^{-1}$ and $\lambda_{PEDOT:PSS\perp} = 0.3\, W \cdot (m\, K)^{-1}$, respectively) [164,245,246]. Thus, instead of organic-based charge transport layers, metal-oxide-based compounds, which have significantly higher thermal conductivities, could be used for improved thermal management. Polycrystalline Al-doped ZnO films, for instance, have more than one order higher thermal conductivities in the range of $\lambda_{ZnO} = 6\, W \cdot (m\, K)^{-1}$ at RT and are therefore ideal for additional heat dissipation in ETLs [247]. The same applies to TiO$_2$ layers with $\lambda_{TiO_2\parallel} = 12.6\, W \cdot (m\, K)^{-1}$ and $\lambda_{TiO_2\perp} = 8.8\, W \cdot (m\, K)^{-1}$ [248]. Metal-oxides have also evolved as a powerful class of materials on the anode side [249]. Transition metal oxides like MoO$_3$, WO$_3$, and V$_2$O$_5$ have successfully been introduced in organic and perovskite solar cells, which should enable enhanced thermal transport in HTLs [250]. Charge transport layers based on graphene or silver nanowires are further potential candidates with respect to heat management and have also been studied in recent years [251,252].

Note that, in general, many strategies, that have been proposed for the thermal management in organic devices, can likewise be used in the field of perovskites [163]. In addition to the absolute values of thermal conductivities for the respective materials, it must be considered that heat transport in the perovskites is due to phonons, while in the electrodes it is mostly associated with electrons. Therefore, it must be ensured that the heat transport at this interface is not limited by its thermal impedance. To guarantee an optimized heat flux, an enhancement of the thermal boundary conductance of such a system has recently been demonstrated by nm sized additional adhesion layers, either titanium or nickel [253]. In this context it should likewise be mentioned that very thin layers can be considered as thermally transparent depending on their mean-free phonon and electron path lengths [168,169]. This means that additional thin functional layers that do not impair the heat flow can be used in the design of metal-halide devices. Although the effectiveness of heat spreading concepts is often directly related to the thermal conductivity of the materials used, alternative passive means of cooling should be considered, as well [254]. One is to use CTLs with an elevated specific heat, which can absorb the heat generated during

dynamic device operation. A different procedure is to effectively store heat dissipated from the electronic components, which is periodic in nature or suddenly temporary, using high latent heat materials (see chapter 6). The use of materials with solid and liquid organic phase changes has previously been proposed regarding the thermal management of mobile phones [255] and the practical applications of liquid-phase-exfoliated graphene as filler material in phase change materials have been outlined [256]. A review of the thermal properties of graphene, few-layer graphene and graphene nanoribbons has also been provided therein along with a discussion of practical applications of graphene in thermal management and energy storage.

6. Determination of the heat transport in metal halide perovskite semiconductors at phase transitions

This chapter deals with the thermal properties of MHPs near and across their phase transitions. For this purpose, initially an introduction to the phase transitions of perovskites is given. In this context, the classification of the phase transitions according to their physical properties is also explained. The determination of the thermal conductivity and the thermal expansion coefficient of $MAPbI_3$ at phase transitions is presented afterwards. Then studies on the thermal conductivity, thermal diffusivity, and heat capacity characteristics in all-inorganic MHPs, $CsPbBr_3$ and $CsPbCl_3$, at phase transitions are given. The characteristics of phase transitions are investigated on micro-crystalline films and single crystals. Highly oriented large crystalline thin films are studied with respect to their film thickness.

6.1. Introduction to structural phases of metal halide perovskite semiconductors

Even though phase transitions have a significant impact on various physical properties, only a few studies have been carried out to assess the thermal properties of metal-halide perovskites in the vicinity of phase transitions [101]. This information is of particular interest if devices are operated in the respective temperature regime. **Figure 36** provides an overview of the crystal phase vs. temperature for some selected hybrid and all-inorganic perovskite representatives. In addition to variations of the dielectric constant and the band structure, which consequently alter the band gap, the optical absorption properties, the carrier dynamics (charge carrier mobilities), etc., discontinuities in the thermo-mechanical properties were reported, as discussed above. Besides, changes in thermal conductivity and heat capacity at first and second transitions are of particular interest since they significantly influence the heat diffusivity and thus the heat management of perovskite devices.
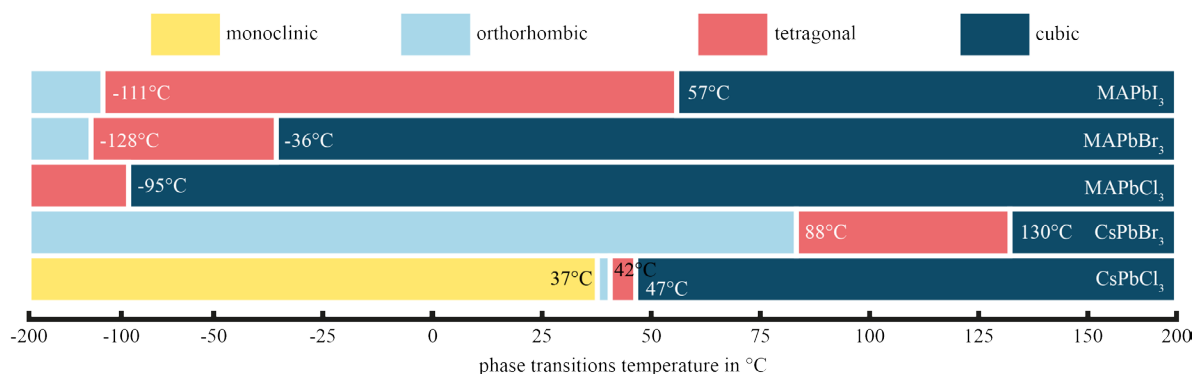
Figure 36: *Representation of the phase transitions of hybrid and all-inorganic perovskites.*

6.2. Classification of phase transitions

Basically, phase transitions are divided into different orders according to the Ehrenfest classification [88]. Therefore, in the following chapter, a basis for the experimental part will be created by dealing with the thermal properties as a function of the structural phase. A short introduction to the terminology as well as the physical basics of phase transitions and their classification will be given. For this purpose, thermodynamic quantities such as volume, enthalpy and entropy are considered as a function of temperature and pressure.

Briefly summarized from [88,257], the enthalpy H is a parameter for describing a thermodynamic system. As a state variable, it describes how much energy is present in a closed system. It is the sum of the internal energy U of the system and the product of the volume V and the pressure p of the described system, $H = U + p \cdot V$. The entropy S as a state variable is a measure for the degree of order of a system. A system always strives for the maximum degree of disorder. A state of maximum disorder is the most probable of all states in a closed system. In this context, the concept of order or disorder is not fully defined, so entropy is not a measure of the symmetry of the system, but merely indicates the number of microscopically achievable states. The entropy is a thermodynamic quantity with which the heat transfer and irreversible processes in thermodynamic processes can be calculated and graphically represented (e.g. T-S diagram to visualize changes to temperature and specific entropy during a thermodynamic process).

The cause of phase transitions lies in the minimization of the Gibbs free energy G according to $G = H - T \cdot S$ by the second law of thermodynamics, in that a closed system reaches an equilibrium state that has the highest entropy for a given internal energy. When the absolute temperature is small, the entropy term is negligible and H determines the equilibrium state. At a high temperature, the term of S dominates and thus determines the state.
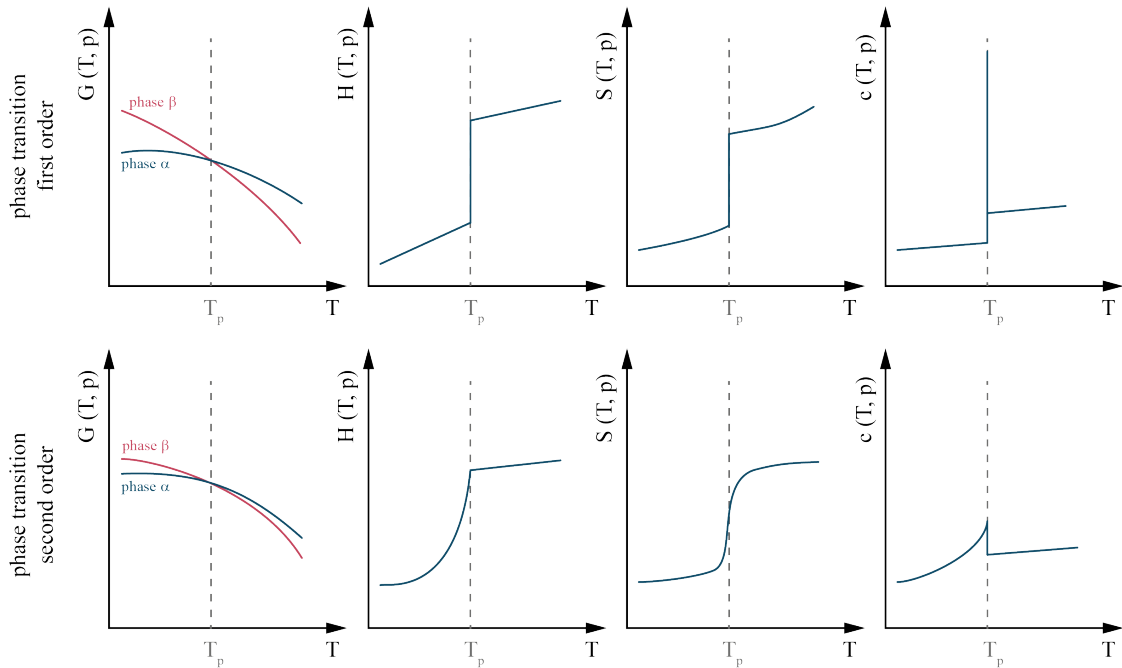
Figure 37: *Behavior of the Gibbs free enthalpy G at the phase transition phase α - phase β, as well as the illustration of the thermodynamic classification of phase transformations according to Ehrenfest.*

According to Ehrenfest's classification, the order of a phase transition is traced back to the behavior of the Gibbs free enthalpy G and its derivatives according to their natural variables p and T. The most commonly cited and distinguished classification is between first and second order phase transitions.

The following conditions apply to define a first order phase transition from phase α to phase β: The free enthalpy $G\,(p,T)$ is continuous, whereas the first derivatives of the free enthalpy $G(T,p)$, the entropy $S = -\left(\frac{\partial G}{\partial T}\right)_p$ and the volume $V = -\left(\frac{\partial G}{\partial p}\right)_T$ are discontinuous. When phase α and phase β coexist at the phase transition temperature T_p with different entropy S_α and S_β,

6. Determination of the heat transport in metal halide perovskite semiconductors at phase transitions

the system must absorb or release energy inferentially according to the formula $\Delta Q_{latent} = T_p \left(S_\beta - S_\alpha \right)$, which is called latent heat and is an characteristic of a first order phase transition.

On the other hand, for the classification of a second order phase transition, the free enthalpy $G\,(p,T)$ is also continuous, as are the first derivatives $S = -\left(\frac{\partial G}{\partial T} \right)_p$ and the volume $V = -\left(\frac{\partial G}{\partial p} \right)_T$.

However, the second derivatives of the free enthalpy $G\,(p,T)$ are discontinuous, such as the heat capacity $C = T \left(\frac{\partial G}{\partial T} \right)_P = -T \left(\frac{\partial^2 G}{\partial T^2} \right)_P$. The heat capacity exhibits discontinuity at the transition but does not become singular and does not exhibit latent heat.

6.3. Determination of the heat transport in MAPbI₃ at phase transitions

In the case of MAPbI3, elevated temperatures can give rise to a phase transition from the tetragonal to the cubic phase. Thus, thermal conductivity measurements were carried out at varied temperature on freshly cleaved I-based single crystals. For each temperature the perovskite crystal has been cleaved freshly to avoid degradation of the surface during the very time-consuming heating and cooling phase between each temperature step. The results are shown in **Figure 38**.
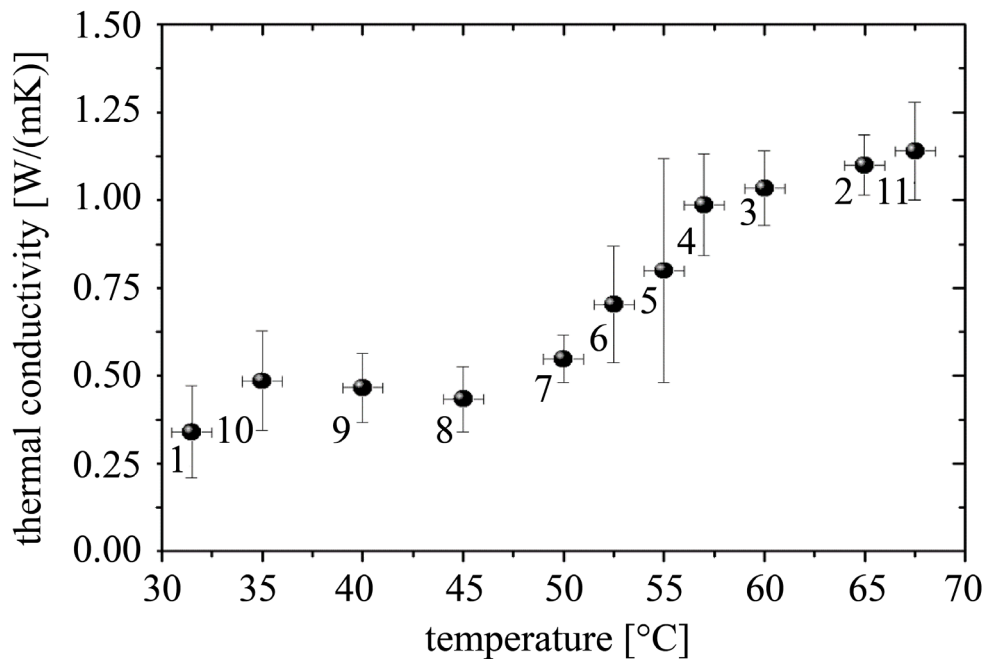
Figure 38: *Temperature-dependent thermal conductivity of a cleaved MAPbI₃ single crystal. The measurement sequence (1⋯11) is indicated by the respective numbers for each data point.*

Following the determination of the thermal conductivity at 32 °C (1), $\lambda_{MAPbI_3}^{cleaved}(T)$ was measured at T = 65 °C (2). Afterward the sample was cooled to 35 °C (steps 3 to 10). The last heat transport investigation (11) was carried out at 67.5 °C. Only minor changes of the average thermal conductivity appear for temperatures between room temperature and 45 °C, where the crystal is in its tetragonal phase. On the contrary, an increase in $\lambda_{MAPbI_3}^{cleaved}(T)$ for T > 50 °C could

be clearly detected. This behavior has been predicted theoretically [106], but it has not been evidenced experimentally, so far. Moreover, it should be noted that the error bars (±40%) are maximum at 55 °C, indicating higher local thermal conductivity variations within the investigated area at this temperature. However, these variations are attributed to local fluctuations as a result of a second order phase transition from the tetragonal to the cubic phase, where no abrupt changes in entropy are present. Finally, the thermal conductivity saturates at $(1.1 \pm 0.1) \, W \cdot (mK)^{-1}$ for T > 57 °C attributed to higher group velocities of acoustic phonons in the pseudocubic phase compared to the tetragonal phase, as previously predicted [106].

In addition, the thermal expansion coefficient has been measured simultaneously by AFM within the same range of temperatures (see **Figure 39**). The resulting negative linear thermal expansion coefficients are $\alpha_{c-tet} = (-5.1 \pm 0.4) \cdot 10^{-4} K^{-1}$(c-axis) and $\alpha_{a-cub} = (4.6 \pm 0.4) \cdot 10^{-4} K^{-1}$ (a-axis) for the tetragonal and pseudocubic phase, respectively.
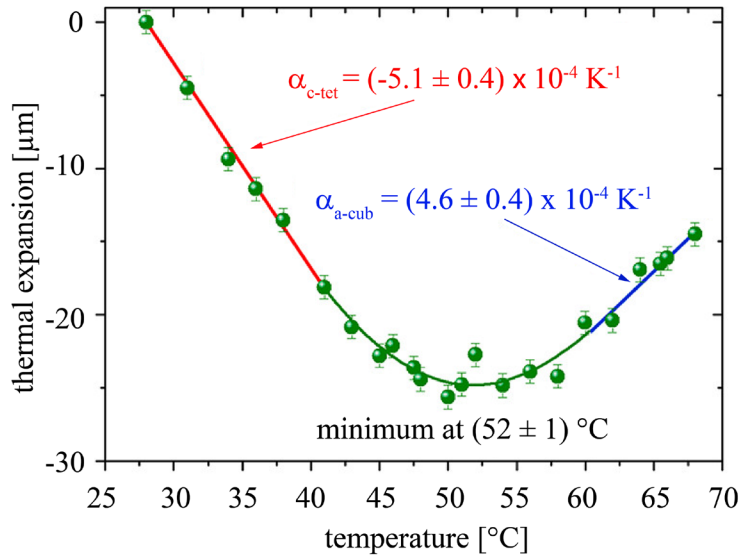
Figure 39: *Determination of linear thermal expansion coefficients and the temperature-induced phase transition from a 2 mm thick MAPbI$_3$ single crystal.*

While α_{c-tet}, determined for T < 42 °C, is on the same order as previously reported values [64], however, α_{a-cub}, determined for T > 60 °C, is one order of magnitude higher in our single crystals compared to numbers determined for thin films. The phase transition occurs at (52 ± 1) °C and agrees well with previous reports of (54 ± 1) °C [64]. A somewhat higher temperature for the phase transition of (57 ± 1) °C has been determined from calorimetric and IR analysis [120] as well as from using equilibrium molecular dynamics simulations [106]. In addition to the phase transition, thermal expansion reveals another aspect of the MAPbI$_3$ perovskite that requires thermal management for MHP-based devices.

6.4. Determination of the heat transport in all-inorganic metal halide perovskite semiconductors at phase transitions

The thermal properties of $CsPbX_3$ perovskites at phase transitions have rarely been studied. Early on, Hirotsu et al. also described the phase transitions in $CsPbCl_3$ and $CsPbBr_3$ single crystals using the neutron diffraction method. The following table shows the results, that were reported in their study. They also categorized the phase transitions according to Ehrenfest [115].

Table 9: *Transition temperatures and order of transitions of $CsPbCl_3$ and $CsPbBr_3$ by the group of Hirotsu et al.* [115].

perovskite	phase	T [°C]	order
	cubic		
		47	first
	tetragonal		
CsPbCl₃		42	second
	orthorhombic		
		37	first
	monoclinic		
	cubic		
		130	first
CsPbBr₃	tetragonal		
		88	second
	orthorhombic		

For $CsPbBr_3$ and $CsPbCl_3$ single crystals and powders a pulse transient method has also been used to evaluate their phase transitions [117,224]. This method provides access to the specific heat c_{spec} and thermal diffusivity a, while the thermal conductivity λ is determined indirectly via the relation $\lambda = a \cdot \rho c$. However, these techniques did not confirm the expected behavior of $c(T)$ when going from the monoclinic to the orthorhombic to the tetragonal phase of $CsPbCl_3$ [117]: specifically, at the first order transitions one would expect a divergence of $c(T)$ due to the latent heat involved. Note, in case of $CsPbCl_3$ the measurement may be complicated as all these transitions occur within a narrow temperature range of $\Delta T \approx 10\ K$. On the contrary, for $CsPbBr_3$ the two phase transitions (orthorhombic-tetragonal-cubic) are separated by a $\Delta T = 42\ K$ [224].

6.4.1. Determination of the thermal conductivity, thermal diffusivity, and heat capacity characteristics in 3D-polymorph CsPbCl₃ at phase transitions

In the case of CsPbCl₃ elevated moderate temperatures can give rise to phase transitions from a monoclinic to orthorhombic to tetragonal to cubic phase. Here, we analyze the thermal properties, $\lambda(\vec{r})$, $a(\vec{r})$, and $c_{vol}(\vec{r})$, of CsPbCl₃ perovskite thin films as a function of temperature, upon increasing the temperature of the perovskite samples starting at RT. As can be seen from our direct measurements shown in **Figure 40** a), only minor changes of the average thermal conductivity in CsPbCl₃ perovskite thin films appear for temperatures between room temperature and 36 °C, where the crystal is in its monoclinic phase. A very slight decrease of λ occurs between 37 °C and 41 °C (orthorhombic phase) due to a slight change in phonon dispersion. In the tetragonal phase, between 42 °C and 46 °C, the thermal conductivity of the CsPbCl₃ thin film shows a slight increase back to values found in the monoclinic phase below 36 °C. While these variations are only marginal, a significant increase of $\lambda_{CsPbCl_3}(T)$ by a factor of three to a level of $1.60 \pm 0.08\ \mathrm{W}\ (m\ K)^{-1}$ is clearly detected at T > 46 °C, where the material assumes its cubic phase. This behavior has been predicted theoretically, due to a significantly higher group velocity of acoustic phonons in the cubic structure compared to that in the tetragonal or orthorhombic phase [106]. In a next step, the average thermal diffusivity, and the average volumetric heat capacity of the CsPbCl₃ perovskites thin films will be discussed. Importantly for perovskite devices, the thermal diffusivity varies notably for the different crystal phases (see **Figure 40** b)). As discussed above, the variations of the average $a(T)$, and $c_{vol}(T)$ can be measured with better accuracy than the respective absolute values. Thus, in contrast to earlier transient measurements on a single crystal [117,224], our technique allows us to unambiguously separate the thermal properties of the different phases. In the orthorhombic structure, the highest thermal diffusivity of $0.7 \pm 0.1\ \mathrm{mm}^2 s^{-1}$ is found, even though the thermal conductivity is minimum there and a considerable acoustic phonon attenuation was observed by neutron scattering experiments in this temperature range [116]. The experimentally determined increase of $a(T)$ in dependence of the structural phases results in a concomitant decrease of $c_{vol}(T)$, as $c_{vol}(T)$ is derived by $\lambda(T)/a(T)$ (see **Figure 40** c) (please note the log scale on the ordinate)).
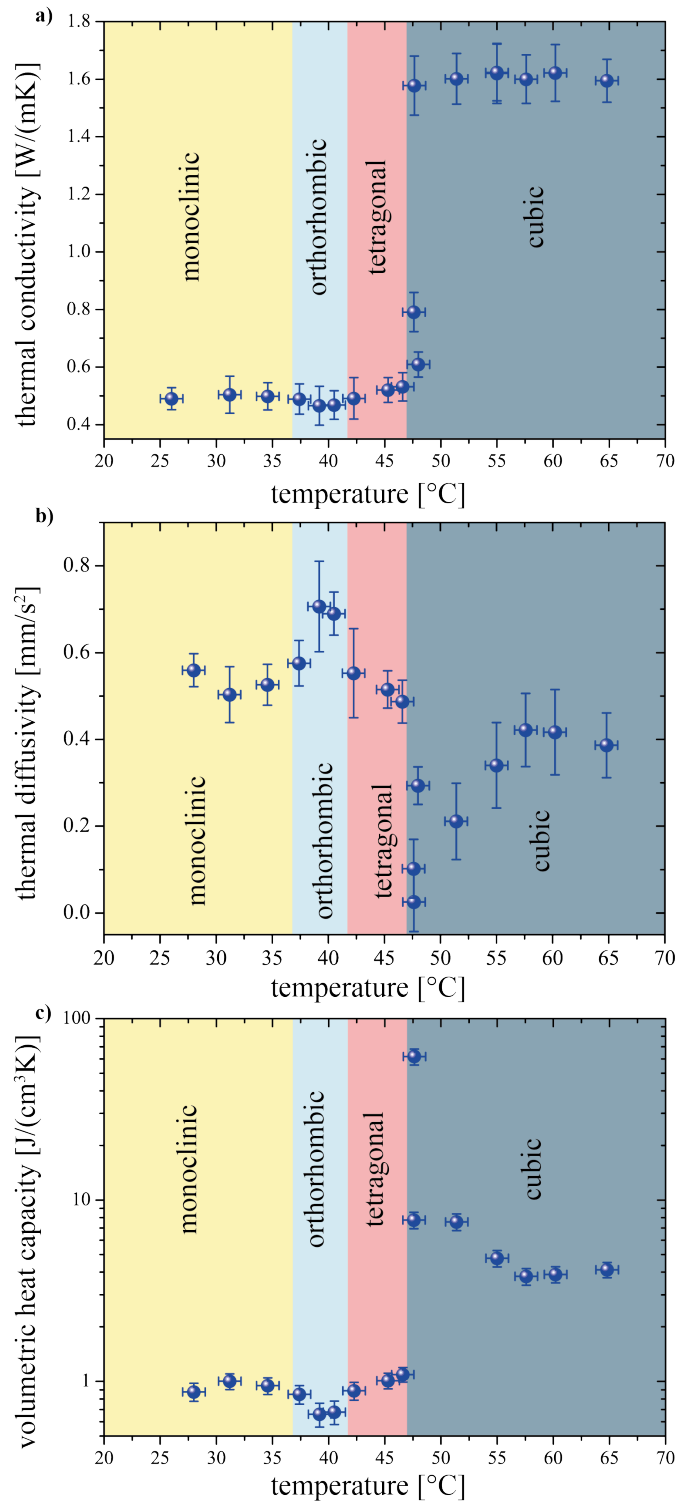
Figure 40: *Simultaneously measured thermal conductivity (a) and thermal diffusivity (b) of CsPbCl₃ perovskite thin films as function of temperature at the phase transitions. The temperature ranges of the corresponding phases are labeled according to earlier studies [11,76]. The volumetric heat capacity calculated from the thermal conductivity and thermal diffusivity is shown below.*

However, apart from the minor changes in thermal properties during the transitions from monoclinic to the tetragonal structural phase at low temperatures, only the latent heat in the average volumetric heat capacity of the $CsPbCl_3$ perovskite thin film is determined at the first-order transition to the cubic phase at 47°C. In the transition from the monoclinic to the orthorhombic phase, no latent heat was measured as an indication of a first-order phase transition. Finally, $c_{vol}(T) = 4.1 \pm 0.4 \, J(cm^3 \cdot K)^{-1}$, is more than 4 times higher in the cubic structure compared to the other phases. This increase can be understood due to the highest degree of freedom for the rotational modes of $PbCl_6$ octahedra around the three principal axes in the cubic phase [116]. Thus, considering the variation in $\lambda(T)$ and $c_{vol}(T)$, the thermal diffusivity $a(T)$ in the cubic phase, after going through a minimum of $0.2 \pm 0.1 \, mm^2 s^{-1}$ at around 47 °C due to latent heat, saturates at $0.4 \pm 0.1 \, mm^2 s^{-1}$ and is smaller than that of the other phases at lower temperature. Finally, it must be mentioned, in contrast to our investigations and theoretical predictions, the transient measurements by the research group of Kubicar et al on single crystals carried out so far showed a lowered specific heat capacity in the cubic structure compared to the monoclinic phase [117,224]. An abnormal characteristic of the thermal diffusivity was also observed and the thermal diffusivity at room temperature is less than that at higher temperatures in the cubic phase.

6.4.2. Determination of heat transport characteristics in 3D-polymorph CsPbBr₃ at phase transitions

In a similar way, micro-crystalline $CsPbBr_3$ perovskite thin films and single crystals were measured in terms of thermal conductivity, thermal diffusivity, and volumetric heat capacity as a function of phase (orthorhombic-tetragonal-cubic) (see **Figure 41**). The measurements were performed from RT up to about 150°C since the phase transitions appear at $T_{o-t} = 88°C$ and $T_{t-c} = 130°C$ [115].The average thermal properties of $CsPbBr_3$ perovskites micro-crystalline thin films and single crystals were determined across their phase transitions to be same in their values of thermal conductivity, thermal diffusivity, and volumetric heat capacity. Only minor changes of the average thermal conductivity are found for temperatures between RT and 88 °C, where the material is in its orthorhombic phase. A slight decrease of λ occurs between 88 °C and 130 °C (within the tetragonal phase).

A significant increase of $\lambda_{CsPbBr_3}(T)$ by a factor of approximately two to a value of 0.85 $\pm$ 0.05 W $(m\,K)^{-1}$ is observed at T > 130 °C. Thus, the thermal conductivity behaves similarly to that CsPbCl$_3$ at the transition to its cubic phase. The orthorhombic-tetragonal phase transition occurs at 88°C, as described in the theoretical literature, and represents an abrupt transition in the thermal conductivity.
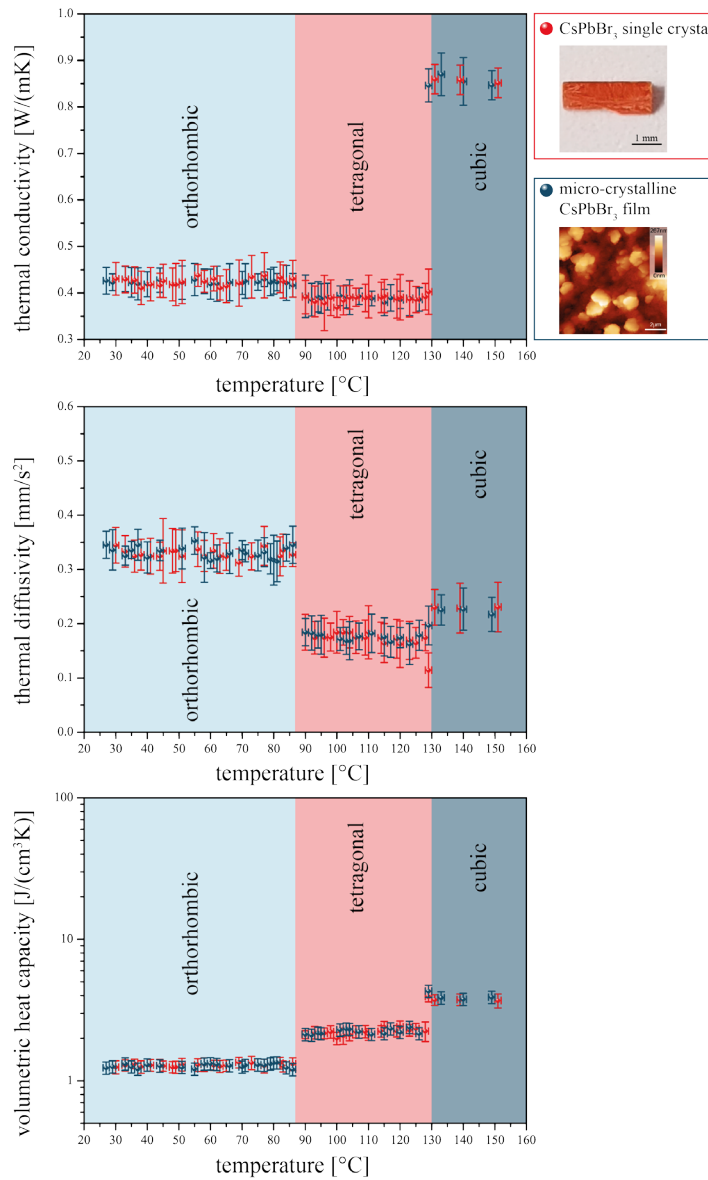
Figure 41: *Thermal conductivity, thermal diffusivity, and volumetric heat capacity vs. temperature pristine micro-crystalline CsPbBr₃ perovskite thin films and single crystal. The temperature ranges of the corresponding crystalline phases are labelled according to earlier structural studies* [115].

Since the behavior of the thermal conductivity of the $CsPbBr_3$ films was comparable to that of the $CsPbCl_3$ films in terms of the absolute values, the thermal diffusivity and the heat capacity also behave in the same way. The decisive difference, which is evident here in the case of the $CsPbBr_3$ thin films, is that no diverging increase in the volumetric heat capacity was detected at the tetragonal-cubic transition and thus there is no indication of latent heat. This behaviour would point to second order phase transition, which deviates from the literature reports of a first-order phase transition [115]. The question of why this behavior is observed here will be taken up in the next section of this chapter. Note that however second order phase transitions, which are quite often associated with substructure properties of crystals [88,258], can depend on the size of perovskite crystals. In the following section the substructure properties of perovskites are described in more detail and will be discussed.

In this regard, the thermal properties were studied for layers with thickness varied between 110-200 nm (see **Figure 42**). Most strikingly, the onset for the increase of the thermal conductivity shifts to lower temperatures with decreasing the layer thickness. Similar to the case of pristine films and single crystals, the thermal conductivity does not change abruptly for the transition from the tetragonal to the cubic crystal phase. In this context, the next section discusses what this behavior might be due to and and offers possible reasons for the shifted transition temperature.
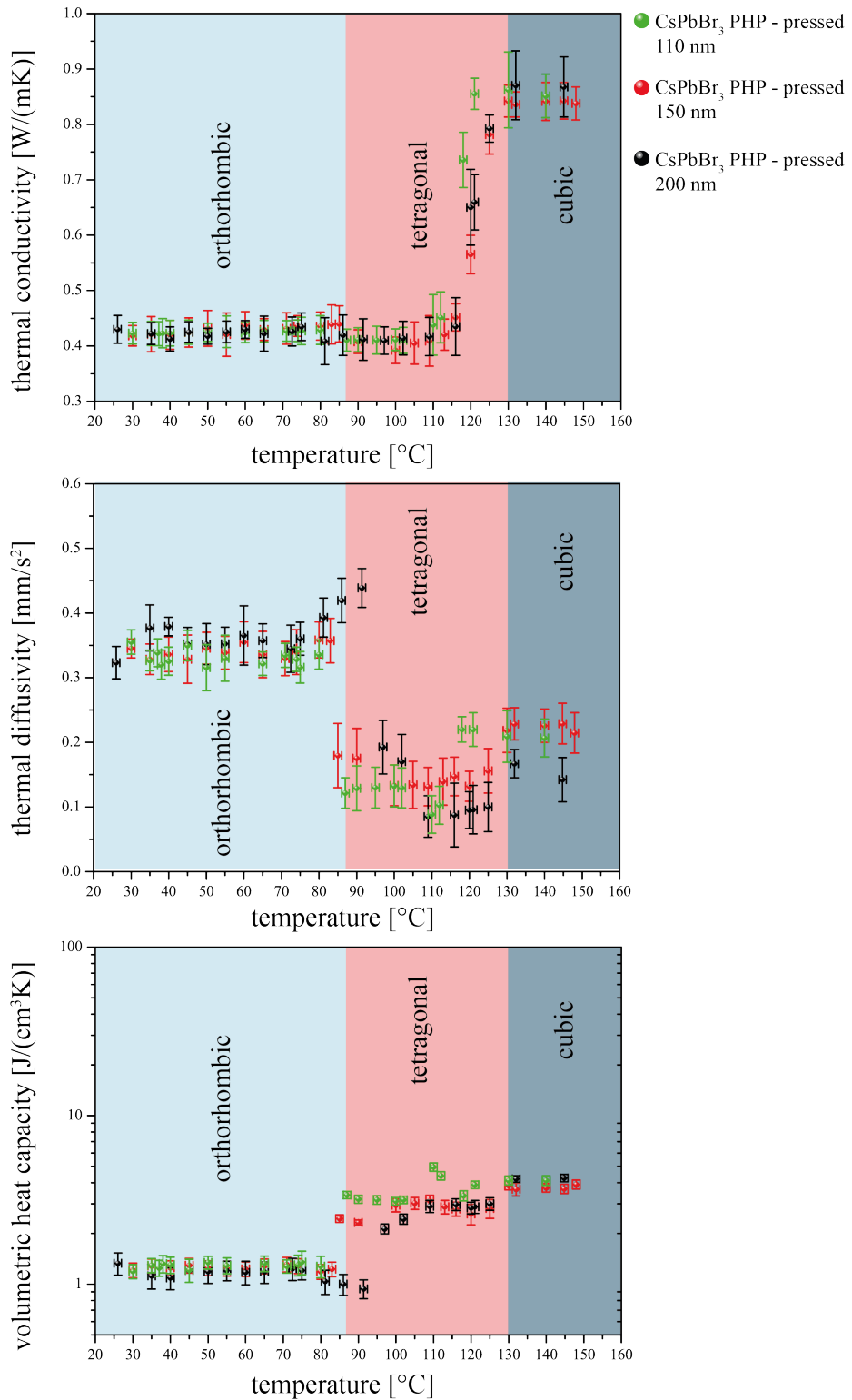
Figure 42: *Thermal conductivity, thermal diffusivity, and volumetric heat capacity vs. temperature for large crystalline CsPbBr₃ perovskite thin films. The temperature ranges of the corresponding crystalline phases are labelled according to earlier structural studies [115].*

6.4.3. Discussion of abnormal heat transport characteristics in tetragonal to cubic phase transitions of halide perovskite semiconductors

First-order phase transitions from tetragonal to cubic crystal structures are usually predicted from MLS simulations as well as early neutron scattering experiments for halide perovskite semiconductors. This prediction is confirmed for the $CsPbCl_3$ phase transitions, where latent heat as an indicator for first-order transitions was measured for the first time within this thesis. This transition additionally indicates an abrupt change in thermal conductivity, due to an abrupt change in the entropy. Note, although the same behavior of λ was also shown for $CsPbBr_3$ perovskites micro-crystalline thin films and single crystals, no latent heat has been detected there. In addition, both the corresponding highly ordered large crystalline films and $MAPbI_3$ single crystals show a continuous increase in thermal conductivity. It is presented that the $CsPbBr_3$ pressed thin films also show a shift in the transition temperature as a function of the film thickness. Latent heat was only detected at the phase transition from the tetragonal to the cubic phase in $CsPbCl_3$. No latent heat could be detected for the predicted first order phase transition from the monoclinic to the orthorhombic phase of $CsPbCl_3$. Note, no latent heats could be detected for the phase transitions of $CsPbBr_3$ at all, even where a first-order phase transition was expected. To what extent the used SThM thermal measurement techniques can provide insights into the order of the phase transitions is not yet clarified and represents a baseline for further research.

7. Summary

Aside from photovoltaics, metal-halide perovskite (MHP) semiconductors have also emerged as an attractive platform for LEDs and lasers. For all of them, performance and operational stability are strongly influenced by thermally activated processes. As a result, studying the heat transport of halide perovskite semiconductors has become increasingly important. In addition to thermal conductivity measurements, thermal diffusivity and heat capacity studies are relevant.

MHPs are a special class of materials with a thermal conductivity typically below 1 W $(m\,K)^{-1}$ and likewise low thermal diffusivity and volumetric heat capacity, which renders thermal studies particularly challenging. Within this thesis, the scanning thermal microscopy (SThM), which uses the 3ω measurement methodology, was further developed to address these challenges. For the first time, local thermal conductivity, thermal diffusivity, and volumetric heat capacity could be measured simultaneously with a high spatial resolution of less than 100 nm independent of the temperature. With SThM operated in the frequency domain, it was possible to measure the thermal properties and to determine the influences of polymorphs/dimensionalities (3D, 2D, 0D) of individual grains in films of MHPs.

Single crystals have also been investigated as reference materials in addition to the thin films. Furthermore, as deposited microcrystalline MHP thin films were improved in terms of their morphology and optoelectronic properties by a thermal imprint using a flat stamp (i.e. planar hot pressing (PHP)). The process enabled an optimal basis for thermal scanning probe microscopy due to the smooth topography with a roughness below 1 nm. The pristine layers of $MAPbX_3$ (X = Cl, Br, I) and $CsPbBr_3$ / $CsPb_2Br_5$ films were prepared by liquid processing, whereas $CsPbCl_3$ thin films were prepared by thermal evaporation, due to limited solubility of the precursors. The PHP method prepared highly oriented, large crystalline thin films.

The thermal conductivity of $MAPbX_3$ single crystals with X= I, Br, and Cl is found to be 0.34 ± 0.12 W $(m\,K)^{-1}$, 0.44 ± 0.08 W $(m\,K)^{-1}$, and 0.50 ± 0.05 W $(m\,K)^{-1}$ at room temperature, respectively. Strikingly, similar thermal conductivities are determined for the corresponding thin-film samples. We could experimentally verify that perovskites with decreasing atomic number of the halide possess a slightly higher average thermal conductivity, due to and increased elastic modulus, which infers an increased speed of sound when going from X = I to X = Cl. By a similar token, the thermal conductivity of $CsPbCl_3$ was found to be

$0.49 \pm 0.04\ W\ (m\ K)^{-1}$, higher than that of $CsPbBr_3$ ($\lambda = 0.43 \pm 0.03\ W\ (m\ K)^{-1}$). These results also reveal that the change of the A-site cation from MA+ to Cs+ did not notably alter the thermal conductivity. A study of the thermal properties of the inorganic MHP polymorphs revealed that the thermal conductivity as well as volumetric heat capacities decrease with decreasing dimensionality.

In this work, first studies on the temperature-dependent thermal conductivity as well as the change of the thermal expansion coefficients of a cleaved $MAPbI_3$ single crystal across the tetragonal-cubic phase transition were obtained. The thermal conductivity of $MAPbI_3$ single crystals in the cubic structure increases to $1.1 \pm 0.1\ W\ (m\ K)^{-1}$. This is due to a significantly higher group velocity of phonons in the cubic structure compared to that in the tetragonal or orthorhombic phase. The temperature-dependent thermal conductivity characteristics of the cleaved $MAPbI_3$ single crystal was determined as a continuous curve. The absolute value of the negative linear thermal expansion coefficients in the tetragonal structure is determined to be $\alpha_{c-tet} = (-5.1 \pm 0.4) \cdot 10^{-4} K^{-1}$.

In addition, the thermal properties across the phase transitions were analyzed in detail for $CsPbCl_3$ and $CsPbBr_3$. In both cases significant increase of the thermal conductivity was found when going from the tetragonal to the cubic phase due to the phonon behaviour.

On the other hand, only slight variations in the thermal conductivity were found for the other phase transitions. Notably, for the transition to the cubic phase of $CsPbCl_3$ thin films, a first-order phase transition was found associated with latent heat and a diverging volumetric heat capacity. In contrast to the findings for $CsPbCl_3$, no latent heat at the phase transition from the tetragonal to the cubic phase was detected for $CsPbBr_3$, which also contrasts with the literature, that reports a first order transition.

On the one hand, instead of abrupt changes in $\lambda_{CsPbBr_3}(T)$ at the phase transition temperature, a continuous increase was found. The onset of the increase of $\lambda_{CsPbBr_3}(T)$ shifts slightly to lower temperatures with decreasing the layer thickness. On the other hand, $c_{vol}(T)$, of the thin films exhibit no typical signature of latent heat. However, these results require further experiments and complementing theoretical studies to gain a consistent understanding.

In summary, this thesis demonstrates that the SThM is well suited for thermal conductivity measurements of ultra-low thermal conducting perovskite semiconductors. The fabrication of single crystals and methods for highly oriented large crystalline films are presented to compare the heat transport of bulk material with that of thin films. Moreover, thermal expansion studies at the phase transition, the temperature dependence of the thermal conductivities, thermal diffusivities, and volumetric heat capacities above room temperature was evaluated experimentally for the first time. The findings of the thermal microscopy are of great general importance for the thermal design and reliability of thin-film devices based on metal halide perovskites, while the measurement technique itself is generally applicable for other thin-film optoelectronic materials.

Bibliography

[1]   National Renewable Energy Laboratory, Best Research-Cell Efficiency Chart, (2022). https://www.nrel.gov/pv/assets/pdfs/best-research-cell-efficiencies-rev220126.pdf (accessed March 12, 2023).

[2]   K. Brinkmann, T. Becker, F. Zimmermann, T. Gahlmann, M. Theisen, T. Haeger, S. Olthof, C. Kreusel, M. Günster, T. Maschwitz, F. Göbelsmann, C. Koch, D. Hertel, P. Caprioglio, L. Perdigon, A. Al-Ashouri, 23.5% efficient monolithic perovskite/organic tandem solar cells based on an ultra-thin metal-like metal-oxide interconnect, Nature. 604 (2022) 280–286. https://doi.org/10.1038/s41586-022-04455-0.

[3]   Z.K. Tan, R.S. Moghaddam, M.L. Lai, P. Docampo, R. Higler, F. Deschler, M. Price, A. Sadhanala, L.M. Pazos, D. Credgington, F. Hanusch, T. Bein, H.J. Snaith, R.H. Friend, Bright light-emitting diodes based on organometal halide perovskite, Nat Nanotechnol. 9 (2014) 687–692. https://doi.org/10.1038/nnano.2014.149.

[4]   F. Deschler, M. Price, S. Pathak, L.E. Klintberg, D.D. Jarausch, R. Higler, S. Hüttner, T. Leijtens, S.D. Stranks, H.J. Snaith, M. Atatüre, R.T. Phillips, R.H. Friend, High photoluminescence efficiency and optically pumped lasing in solution-processed mixed halide perovskite semiconductors, Journal of Physical Chemistry Letters. 5 (2014) 1421–1426. https://doi.org/10.1021/jz5005285.

[5]   G. Xing, N. Mathews, S.S. Lim, N. Yantara, X. Liu, D. Sabba, M. Grätzel, S. Mhaisalkar, T.C. Sum, Low-temperature solution-processed wavelength-tunable perovskites for lasing, Nat Mater. 13 (2014) 476–480. https://doi.org/10.1038/nmat3911.

[6]   C. Lee, J. Hong, A. Stroppa, M.-H. Whangbo, J.H. Shim, Organic–inorganic hybrid perovskites ABI_3 ($A = CH_3NH_3$, NH_2CHNH_2; $B = Sn$, Pb) as potential thermoelectric materials: a density functional evaluation, RSC Adv. 5 (2015) 78701–78707. https://doi.org/10.1039/C5RA12536G.

[7]   N. Aristidou, I. Sanchez-Molina, T. Chotchuangchutchaval, M. Brown, L. Martinez, T. Rath, S.A. Haque, The Role of Oxygen in the Degradation of Methylammonium Lead Trihalide Perovskite Photoactive Layers, Angewandte Chemie. 127 (2015) 8326–8330. https://doi.org/10.1002/ange.201503153.

[8]   R.K. Misra, S. Aharon, B. Li, D. Mogilyansky, I. Visoly-Fisher, L. Etgar, E.A. Katz, Temperature- and component-dependent degradation of perovskite photovoltaic materials under concentrated sunlight, Journal of Physical Chemistry Letters. 6 (2015) 326–330. https://doi.org/10.1021/jz502642b.

[9]   D. Bryant, N. Aristidou, S. Pont, I. Sanchez-Molina, T. Chotchunangatchaval, S. Wheeler, J.R. Durrant, S.A. Haque, Light and oxygen induced degradation limits the operational stability of methylammonium lead triiodide perovskite solar cells, Energy Environ Sci. 9 (2016) 1655–1660. https://doi.org/10.1039/c6ee00409a.

[10]   E.J. Juarez-Perez, Z. Hawash, S.R. Raga, L.K. Ono, Y. Qi, Thermal degradation of CH3NH3PbI3 perovskite into NH3 and CH3I gases observed by coupled thermogravimetry-mass spectrometry analysis, Energy Environ Sci. 9 (2016) 3406–3410. https://doi.org/10.1039/c6ee02016j.

[11]   S. Hirotsu, Experimental Studies of Structural Phase Transitions in CsPbCl3, J Physical Soc Japan. 31 (1971) 552–560. https://doi.org/10.1143/JPSJ.31.552.

[12]   S. Hirotsu, T. Suzuki, Elastic Constants and Thermal Expansion of CsPbCl3, J Physical Soc Japan. 44 (1978) 1604–1611. https://doi.org/10.1143/JPSJ.44.1604.

[13]   B. Conings, J. Drijkoningen, N. Gauquelin, A. Babayigit, J. D'Haen, L. D'Olieslaeger, A. Ethirajan, J. Verbeeck, J. Manca, E. Mosconi, F. de Angelis, H.G. Boyen, Intrinsic Thermal Instability of Methylammonium Lead Trihalide Perovskite, Adv Energy Mater. 5 (2015). https://doi.org/10.1002/aenm.201500477.

[14]   R. Heiderhoff, T. Haeger, N. Pourdavoud, T. Hu, M. Al-Khafaji, A. Mayer, Y. Chen, H.C. Scheer, T. Riedl, Thermal Conductivity of Methylammonium Lead Halide Perovskite Single Crystals and Thin Films: A Comparative Study, Journal of Physical Chemistry C. 121 (2017) 28306–28311. https://doi.org/10.1021/acs.jpcc.7b11495.

[15]   CHR.KN. MØLLER, A Phase Transition in Cæsium Plumbochloride, Nature. 180 (1957) 981–982. https://doi.org/10.1038/180981a0.

[16]   Y. Liu, Z. Yang, S.F. Liu, Recent Progress in Single-Crystalline Perovskite Research Including Crystal Preparation, Property Evaluation, and Applications, Advanced Science. 5 (2018) 1700471. https://doi.org/10.1002/advs.201700471.

[17] Y. Jia, R.A. Kerner, A.J. Grede, A.N. Brigeman, B.P. Rand, N.C. Giebink, Diode-Pumped Organo-Lead Halide Perovskite Lasing in a Metal-Clad Distributed Feedback Resonator, Nano Lett. 16 (2016) 4624–4629. https://doi.org/10.1021/acs.nanolett.6b01946.

[18] M. Cadelano, V. Sarritzu, N. Sestu, D. Marongiu, F. Chen, R. Piras, R. Corpino, C.M. Carbonaro, F. Quochi, M. Saba, A. Mura, G. Bongiovanni, Can Trihalide Lead Perovskites Support Continuous Wave Lasing?, Adv Opt Mater. 3 (2015) 1557–1564. https://doi.org/10.1002/adom.201500229.

[19] J.P. Attfield, P. Lightfoot, R.E. Morris, Perovskites, Dalton Transactions. 44 (2015) 10541–10542. https://doi.org/10.1039/c5dt90083b.

[20] A.R. Chakhmouradian, P.M. Woodward, Celebrating 175 years of perovskite research: A tribute to Roger H. Mitchell, Phys Chem Miner. 41 (2014) 387–391. https://doi.org/10.1007/s00269-014-0678-9.

[21] Y. Noguchi, H. Matsuo, Polarization and dielectric properties of bifeo3-batio3 superlattice-structured ferroelectric films, Nanomaterials. 11 (2021). https://doi.org/10.3390/nano11071857.

[22] N. Nuraje, K. Su, Perovskite ferroelectric nanomaterials, Nanoscale. 5 (2013) 8752. https://doi.org/10.1039/c3nr02543h.

[23] F. Wang, I. Grinberg, A.M. Rappe, Band gap engineering strategy via polarization rotation in perovskite ferroelectrics, Appl Phys Lett. 104 (2014). https://doi.org/10.1063/1.4871707.

[24] A.K. Jena, A. Kulkarni, T. Miyasaka, Halide Perovskite Photovoltaics: Background, Status, and Future Prospects, Chem Rev. 119 (2019) 3036–3103. https://doi.org/10.1021/acs.chemrev.8b00539.

[25] W. Shockley, H.J. Queisser, Detailed Balance Limit of Efficiency of p-n Junction Solar Cells, J Appl Phys. 32 (1961) 510–519. https://doi.org/10.1063/1.1736034.

[26] N. Pourdavoud, A. Mayer, M. Buchmüller, K. Brinkmann, T. Haeger, T. Hu, R. Heiderhoff, I. Shutsko, P. Görrn, Y. Chen, H.-C. Scheer, T. Riedl, Distributed Feedback Lasers Based on MAPbBr3, Adv Mater Technol. 3 (2018) 1700253. https://doi.org/10.1002/admt.201700253.

[27] G. Li, Z.K. Tan, D. Di, M.L. Lai, L. Jiang, J.H.W. Lim, R.H. Friend, N.C. Greenham, Efficient Light-Emitting Diodes Based on Nanocrystalline Perovskite in a Dielectric Polymer Matrix, Nano Lett. 15 (2015) 2640–2644. https://doi.org/10.1021/acs.nanolett.5b00235.

[28] L. Schmidt-Mende, V. Dyakonov, S. Olthof, F. Ünlü, K.M.T. Lê, S. Mathur, A.D. Karabanov, D.C. Lupascu, L.M. Herz, A. Hinderhofer, F. Schreiber, A. Chernikov, D.A. Egger, O. Shargaieva, C. Cocchi, E. Unger, M. Saliba, M.M. Byranvand, M. Kroll, F. Nehm, K. Leo, A. Redinger, J. Höcker, T. Kirchartz, J. Warby, E. Gutierrez-Partida, D. Neher, M. Stolterfoht, U. Würfel, M. Unmüssig, J. Herterich, C. Baretzky, J. Mohanraj, M. Thelakkat, C. Maheu, W. Jaegermann, T. Mayer, J. Rieger, T. Fauster, D. Niesner, F. Yang, S. Albrecht, T. Riedl, A. Fakharuddin, M. Vasilopoulou, Y. Vaynzof, D. Moia, J. Maier, M. Franckevičius, V. Gulbinas, R.A. Kerner, L. Zhao, B.P. Rand, N. Glück, T. Bein, F. Matteocci, L.A. Castriotta, A. di Carlo, M. Scheffler, C. Draxl, Roadmap on organic-inorganic hybrid perovskite semiconductors and devices, APL Mater. 9 (2021). https://doi.org/10.1063/5.0047616.

[29] M.A. Green, A. Ho-Baillie, H.J. Snaith, The emergence of perovskite solar cells, Nat Photonics. 8 (2014) 506–514. https://doi.org/10.1038/nphoton.2014.134.

[30] S. Tao, I. Schmidt, G. Brocks, J. Jiang, I. Tranca, K. Meerholz, S. Olthof, Absolute energy level positions in tin- and lead-based halide perovskites, Nat Commun. 10 (2019). https://doi.org/10.1038/s41467-019-10468-7.

[31] K.O. Brinkmann, T. Becker, F. Zimmermann, C. Kreusel, T. Gahlmann, T. Haeger, T. Riedl, The Optical Origin of Near-Unity External Quantum Efficiencies in Perovskite Solar Cells, Solar RRL. 5 (2021). https://doi.org/10.1002/solr.202100371.

[32] J. Hieulle, X. Wang, C. Stecker, D.Y. Son, L. Qiu, R. Ohmann, L.K. Ono, A. Mugarza, Y. Yan, Y. Qi, Unraveling the Impact of Halide Mixing on Perovskite Stability, J Am Chem Soc. 141 (2019) 3515–3523. https://doi.org/10.1021/jacs.8b11210.

[33] N. Rybin, D. Ghosh, J. Tisdale, S. Shrestha, M. Yoho, D. Vo, J. Even, C. Katan, W. Nie, A.J. Neukirch, S. Tretiak, Effects of Chlorine Mixing on Optoelectronics, Ion Migration, and Gamma-Ray Detection in Bromide Perovskites, Chemistry of Materials. 32 (2020) 1854–1863. https://doi.org/10.1021/acs.chemmater.9b04244.

[34] H. Chen, S. Xiang, W. Li, H. Liu, L. Zhu, S. Yang, Inorganic Perovskite Solar Cells: A Rapidly Growing Field, Solar RRL. 2 (2018). https://doi.org/10.1002/solr.201700188.

[35] Z. Wang, A.K. Baranwal, M.A. Kamarudin, Y. Kamata, C.H. Ng, M. Pandey, T. Ma, S. Hayase, Structured crystallization for efficient all-inorganic perovskite solar cells with high phase stability, J Mater Chem A Mater. 7 (2019) 20390–20397. https://doi.org/10.1039/c9ta05556h.

[36] A.J. Knight, L.M. Herz, Preventing phase segregation in mixed-halide perovskites: A perspective, Energy Environ Sci. 13 (2020) 2024–2046. https://doi.org/10.1039/d0ee00788a.

[37] S. Khalfin, Y. Bekenstein, Advances in lead-free double perovskite nanocrystals, engineering band-gaps and enhancing stability through composition tunability, Nanoscale. 11 (2019) 8665–8679. https://doi.org/10.1039/c9nr01031a.

[38] F.H. Gourji, D. Velauthapillai, A review on Cs-based Pb-free double halide perovskites: From theoretical and experimental studies to doping and applications, Molecules. 26 (2021). https://doi.org/10.3390/molecules26072010.

[39] T. Zhou, M. Wang, Z. Zang, X. Tang, L. Fang, Two-dimensional lead-free hybrid halide perovskite using superatom anions with tunable electronic properties, Solar Energy Materials and Solar Cells. 191 (2019) 33–38. https://doi.org/10.1016/j.solmat.2018.10.021.

[40] Z. Li, X. Liu, J. Xu, S. Yang, H. Zhao, H. Huang, S. (Frank) Liu, J. Yao, All-inorganic 0D/3D $Cs_4Pb(IBr)_6$ /$CsPbI_{3-x}Br_x$ mixed-dimensional perovskite solar cells with enhanced efficiency and stability, J Mater Chem C Mater. 8 (2020) 6977–6987. https://doi.org/10.1039/D0TC01832E.

[41] M. Cao, Y. Damji, C. Zhang, L. Wu, Q. Zhong, P. Li, D. Yang, Y. Xu, Q. Zhang, Low-Dimensional-Networked Cesium Lead Halide Perovskites: Properties, Fabrication, and Applications, Small Methods. 4 (2020). https://doi.org/10.1002/smtd.202000303.

[42] P. Gao, A.R. bin Mohd Yusoff, M.K. Nazeeruddin, Dimensionality engineering of hybrid halide perovskite light absorbers, Nat Commun. 9 (2018). https://doi.org/10.1038/s41467-018-07382-9.

[43] R.L.Z. Hoye, J. Hidalgo, R.A. Jagt, J.P. Correa-Baena, T. Fix, J.L. MacManus-Driscoll, The Role of Dimensionality on the Optoelectronic Properties of Oxide and Halide Perovskites, and their Halide Derivatives, Adv Energy Mater. 12 (2022). https://doi.org/10.1002/aenm.202100499.

[44] M.I. Saidaminov, O.F. Mohammed, O.M. Bakr, Low-dimensional-networked metal halide perovskites: The next big thing, ACS Energy Lett. 2 (2017) 889–896. https://doi.org/10.1021/acsenergylett.6b00705.

[45] S. Seth, A. Samanta, Photoluminescence of Zero-Dimensional Perovskites and Perovskite-Related Materials, Journal of Physical Chemistry Letters. 9 (2018) 176–183. https://doi.org/10.1021/acs.jpclett.7b02931.

[46] Z. Li, X. Liu, J. Xu, S. Yang, H. Zhao, H. Huang, S.F. Liu, J. Yao, 2D–3D $Cs_2PbI_2Cl_2$ –$CsPbI_{2.5}Br_{0.5}$ Mixed-Dimensional Films for All-Inorganic Perovskite Solar Cells with Enhanced Efficiency and Stability, J Phys Chem Lett. 11 (2020) 4138–4146. https://doi.org/10.1021/acs.jpclett.0c01134.

[47] X. Zhang, B. Xu, J. Zhang, Y. Gao, Y. Zheng, K. Wang, X.W. Sun, All-Inorganic Perovskite Nanocrystals for High-Efficiency Light Emitting Diodes: Dual-Phase CsPbBr3-CsPb2Br5 Composites, Adv Funct Mater. 26 (2016) 4595–4600. https://doi.org/10.1002/adfm.201600958.

[48] X. Tang, Z. Hu, W. Yuan, W. Hu, H. Shao, D. Han, J. Zheng, J. Hao, Z. Zang, J. Du, Y. Leng, L. Fang, M. Zhou, Perovskite $CsPb_2Br_5$ Microplate Laser with Enhanced Stability and Tunable Properties, Adv Opt Mater. 5 (2017) 1600788. https://doi.org/10.1002/adom.201600788.

[49] M.I. Saidaminov, J. Almutlaq, S. Sarmah, I. Dursun, A.A. Zhumekenov, R. Begum, J. Pan, N. Cho, O.F. Mohammed, O.M. Bakr, Pure Cs4PbBr6: Highly Luminescent Zero-Dimensional Perovskite Solids, ACS Energy Lett. 1 (2016) 840–845. https://doi.org/10.1021/acsenergylett.6b00396.

[50] I. Dursun, M. De Bastiani, B. Turedi, B. Alamer, A. Shkurenko, J. Yin, A.M. El-Zohry, I. Gereige, A. AlSaggaf, O.F. Mohammed, M. Eddaoudi, O.M. Bakr, $CsPb_2Br_5$ Single Crystals: Synthesis and Characterization, ChemSusChem. 10 (2017) 3746–3749. https://doi.org/10.1002/cssc.201701131.

[51] T.T. Ava, A. al Mamun, S. Marsillac, G. Namkoong, A review: Thermal stability of methylammonium lead halide based perovskite solar cells, Applied Sciences (Switzerland). 9 (2019). https://doi.org/10.3390/app9010188.

[52] S. Sharma, N., Weiden, A. Weiss, Phase Diagrams of Quasibinary Systems of the Type: ABX3 — A′BX3; ABX3 — AB′X3, and ABX3 — ABX′3; X = Halogen, Zeitschrift Für Physikalische Chemie. 175 (1992) 63–80.

[53] C.C. Stoumpos, C.D. Malliakas, J.A. Peters, Z. Liu, M. Sebastian, J. Im, T.C. Chasapis, A.C. Wibowo, D.Y. Chung, A.J. Freeman, B.W. Wessels, M.G. Kanatzidis, Crystal growth of the perovskite semiconductor CsPbBr3: A new material for high-energy radiation detection, Cryst Growth Des. 13 (2013) 2722–2727. https://doi.org/10.1021/cg400645t.

[54] F. Fayon, Y. Vaills, P. Simon, P. Echegut, C. Bessada, J. Emery, J.-Y. Buzare, Study of CsPbCl $_3$ between T = 47°C and the melting point by the ^{133} Cs NMR AND Gd $^{3+}$ epr measurements, Ferroelectrics. 185 (1996) 201–204. https://doi.org/10.1080/00150199608210513.

[55] Q. Xu, H. Wei, W. Wei, W. Chuirazzi, D. DeSantis, J. Huang, L. Cao, Detection of charged particles with a methylammonium lead tribromide perovskite single crystal, Nucl Instrum Methods Phys Res A. 848 (2017) 106–108. https://doi.org/10.1016/j.nima.2016.12.062.

[56] Y.C. Kim, K.H. Kim, D.-Y. Son, D.-N. Jeong, J.-Y. Seo, Y.S. Choi, I.T. Han, S.Y. Lee, N.-G. Park, Printable organometallic perovskite enables large-area, low-dose X-ray imaging, Nature. 550 (2017) 87–91. https://doi.org/10.1038/nature24032.

[57] S. Yakunin, D.N. Dirin, Y. Shynkarenko, V. Morad, I. Cherniukh, O. Nazarenko, D. Kreil, T. Nauser, M. v. Kovalenko, Detection of gamma photons using solution-grown single crystals of hybrid lead halide perovskites, Nat Photonics. 10 (2016) 585–589. https://doi.org/10.1038/nphoton.2016.139.

[58] B. Brunetti, C. Cavallo, A. Ciccioli, G. Gigli, A. Latini, On the Thermal and Thermodynamic (In)Stability of Methylammonium Lead Halide Perovskites, Sci Rep. 6 (2016). https://doi.org/10.1038/srep31896.

[59] Z. Song, S.C. Watthage, A.B. Phillips, B.L. Tompkins, R.J. Ellingson, M.J. Heben, Impact of Processing Temperature and Composition on the Formation of Methylammonium Lead Iodide Perovskites, Chemistry of Materials. 27 (2015) 4612–4619. https://doi.org/10.1021/acs.chemmater.5b01017.

[60] M. Kulbak, S. Gupta, N. Kedem, I. Levine, T. Bendikov, G. Hodes, D. Cahen, Cesium Enhances Long-Term Stability of Lead Bromide Perovskite-Based Solar Cells, Journal of Physical Chemistry Letters. 7 (2016) 167–172. https://doi.org/10.1021/acs.jpclett.5b02597.

[61] I. Deretzis, A. Alberti, G. Pellegrino, E. Smecca, F. Giannazzo, N. Sakai, T. Miyasaka, A. la Magna, Atomistic origins of $CH_3NH_3PbI_3$ degradation to PbI_2 in vacuum, Appl Phys Lett. 106 (2015) 131904. https://doi.org/10.1063/1.4916821.

[62] E.J. Juarez-Perez, L.K. Ono, Y. Qi, Thermal degradation of formamidinium based lead halide perovskites into: Sym -triazine and hydrogen cyanide observed by coupled thermogravimetry-mass spectrometry analysis, J Mater Chem A Mater. 7 (2019) 16912–16919. https://doi.org/10.1039/c9ta06058h.

[63] A. García-Fernández, E.J. Juarez-Perez, S. Castro-García, M. Sánchez-Andújar, L.K. Ono, Y. Jiang, Y. Qi, Benchmarking Chemical Stability of Arbitrarily Mixed 3D Hybrid Halide Perovskites for Solar Cell Applications, Small Methods. 2 (2018) 1800242. https://doi.org/10.1002/smtd.201800242.

[64] T.J. Jacobsson, L.J. Schwan, M. Ottosson, A. Hagfeldt, T. Edvinsson, Determination of Thermal Expansion Coefficients and Locating the Temperature-Induced Phase Transition in Methylammonium Lead Perovskites Using X-ray Diffraction, Inorg Chem. 54 (2015) 10678–10685. https://doi.org/10.1021/acs.inorgchem.5b01481.

[65] C. Ge, M. Hu, P. Wu, Q. Tan, Z. Chen, Y. Wang, J. Shi, J. Feng, Ultralow Thermal Conductivity and Ultrahigh Thermal Expansion of Single-Crystal Organic–Inorganic Hybrid Perovskite $CH_3NH_3PbX_3$ (X = Cl, Br, I), The Journal of Physical Chemistry C. 122 (2018) 15973–15978. https://doi.org/10.1021/acs.jpcc.8b05919.

[66] M. Keshavarz, M. Ottesen, S. Wiedmann, M. Wharmby, R. Küchler, H. Yuan, E. Debroye, J.A. Steele, J. Martens, N.E. Hussey, M. Bremholm, M.B.J. Roeffaers, J. Hofkens, Tracking Structural Phase Transitions in Lead-Halide Perovskites by Means of Thermal Expansion, Advanced Materials. 31 (2019). https://doi.org/10.1002/adma.201900521.

[67] H. Mashiyama, Y. Kawamura, E. Magome, Y. Kubota, Displacive Character of the Cubic-Tetragonal Transition in CH, Journal of the Korean Physical Society. 42 (2003) 1026–1029.

[68] D.M. Trots, S.V. Myagkota, High-temperature structural evolution of caesium and rubidium triiodoplumbates, Journal of Physics and Chemistry of Solids. 69 (2008) 2520–2526. https://doi.org/10.1016/j.jpcs.2008.05.007.

[69] J.A. Steele, H. Jin, I. Dovgaliuk, R.F. Berger, T. Braeckevelt, H. Yuan, C. Martin, E. Solano, K. Lejaeghere, S.M.J. Rogge, C. Notebaert, W. Vandezande, K.P.F. Janssen, B. Goderis, E. Debroye, Y.-K. Wang, Y. Dong, D. Ma, M. Saidaminov, H. Tan, Z. Lu, V. Dyadkin, D. Chernyshov, V. van Speybroeck, E.H. Sargent, J. Hofkens, M.B.J. Roeffaers, Thermal unequilibrium of strained black CsPbI $_3$ thin films, Science (1979). 365 (2019) 679–684. https://doi.org/10.1126/science.aax3878.

[70] K. Nitsch, M. Rodova, Thermomechanical Measurements of Lead Halide Single Crystals, Physica Status Solidi (b). 234 (2002) 701–709. https://doi.org/10.1002/1521-3951(200211)234:2<701::AID-PSSB701>3.0.CO;2-1.

[71] Y. Rakita, S.R. Cohen, N.K. Kedem, G. Hodes, D. Cahen, Mechanical properties of APbX3 (A = Cs or CH3NH3; X= I or Br) perovskite single crystals, MRS Commun. 5 (2015) 623–629. https://doi.org/10.1557/mrc.2015.69.

[72] M. Rodová, J. Brooek, K. Kníek, K. Nitsch, PHASE TRANSITIONS IN TERNARY CAESIUM LEAD BROMIDE, J Therm Anal Calorim. 71 (2003) 667–673. https://doi.org/10.1023/A:1022836800820.

[73] D.H. Fabini, C.C. Stoumpos, G. Laurita, A. Kaltzoglou, A.G. Kontos, P. Falaras, M.G. Kanatzidis, R. Seshadri, Reentrant Structural and Optical Properties and Large Positive Thermal Expansion in Perovskite Formamidinium Lead Iodide, Angewandte Chemie. 128 (2016) 15618–15622. https://doi.org/10.1002/ange.201609538.

[74] D.S. Tsvetkov, M.O. Mazurin, V. V. Sereda, I.L. Ivanov, D.A. Malyshkin, A.Y. Zuev, Formation Thermodynamics, Stability, and Decomposition Pathways of CsPbX3 (X = Cl, Br, I) Photovoltaic Materials, Journal of Physical Chemistry C. 124 (2020) 4252–4260. https://doi.org/10.1021/acs.jpcc.9b11494.

[75] P. Pistor, J. Borchert, W. Fränzel, R. Csuk, R. Scheer, Monitoring the phase formation of coevaporated lead halide perovskite thin films by in situ x-ray diffraction, Journal of Physical Chemistry Letters. 5 (2014) 3308–3312. https://doi.org/10.1021/jz5017312.

[76] M.I. Cohen, K.F. Young, T.T. Chang, W.S. Brower, Phase transitions in CsPbCl3, J Appl Phys. 42 (1971) 5267–5272. https://doi.org/10.1063/1.1659935.

[77] J. Sadanandam, G. Jayasagar, S. V Suryanarayana, Lattice thermal expansion of cesium plumbo chloride, Pramana. 13 (1979) 127–130. https://doi.org/10.1007/BF02872131.

[78] J. Zhao, Y. Deng, H. Wei, X. Zheng, Z. Yu, Y. Shao, J.E. Shield, J. Huang, Strained hybrid perovskite thin films and their impact on the intrinsic stability of perovskite solar cells, 2017. https://www.science.org.

[79] A.D. Wright, C. Verdi, R.L. Milot, G.E. Eperon, M.A. Pérez-Osorio, H.J. Snaith, F. Giustino, M.B. Johnston, L.M. Herz, Electron-phonon coupling in hybrid lead halide perovskites, Nat Commun. 7 (2016). https://doi.org/10.1038/ncomms11755.

[80] T.W. Jones, A. Osherov, M. Alsari, M. Sponseller, B.C. Duck, Y.K. Jung, C. Settens, F. Niroui, R. Brenes, C. v. Stan, Y. Li, M. Abdi-Jalebi, N. Tamura, J.E. MacDonald, M. Burghammer, R.H. Friend, V. Bulović, A. Walsh, G.J. Wilson, S. Lilliu, S.D. Stranks, Lattice strain causes non-radiative losses in halide perovskites, Energy Environ Sci. 12 (2019) 596–606. https://doi.org/10.1039/c8ee02751j.

[81] S. Jariwala, H. Sun, G.W.P. Adhyaksa, A. Lof, L.A. Muscarella, B. Ehrler, E.C. Garnett, D.S. Ginger, Local Crystal Misorientation Influences Non-radiative Recombination in Halide Perovskites, Joule. 3 (2019) 3048–3060. https://doi.org/10.1016/j.joule.2019.09.001.

[82] X. Li, Y. Luo, M. v. Holt, Z. Cai, D.P. Fenning, Residual Nanoscale Strain in Cesium Lead Bromide Perovskite Reduces Stability and Shifts Local Luminescence, Chemistry of Materials. 31 (2019) 2778–2785. https://doi.org/10.1021/acs.chemmater.8b04937.

[83] H. Tsai, R. Asadpour, J.-C. Blancon, C.C. Stoumpos, O. Durand, J.W. Strzalka, B. Chen, R. Verduzco, P.M. Ajayan, S. Tretiak, J. Even, M.A. Alam, M.G. Kanatzidis, W. Nie, A.D. Mohite, Light-induced lattice expansion leads to high-efficiency perovskite solar cells, 2018. https://www.science.org.

[84] N. Rolston, R. Bennett-Kennett, L.T. Schelhas, J.M. Luther, J.A. Christians, J.J. Berry, R.H. Dauskardt, Comment on "Light-induced lattice expansion leads to high-efficiency perovskite solar cells," Science (1979). 368 (2020) 67–70. https://doi.org/10.1126/science.aay8691.

[85] X. Li, M. Tschumi, H. Han, S.S. Babkair, R.A. Alzubaydi, A.A. Ansari, S.S. Habib, M.K. Nazeeruddin, S.M. Zakeeruddin, M. Grätzel, Outdoor Performance and Stability under Elevated Temperatures and Long-Term Light Soaking of Triple-Layer Mesoporous Perovskite Photovoltaics, Energy Technology. 3 (2015) 551–555. https://doi.org/10.1002/ente.201500045.

[86] M. Wu, N. Haji Ladi, Z. Yi, H. Li, Y. Shen, M. Wang, Stability Issue of Perovskite Solar Cells under Real-World Operating Conditions, Energy Technology. 8 (2020) 1900744. https://doi.org/10.1002/ente.201900744.

[87] A.N. Cleland, Foundations of Nanomechanics, 1st ed., Springer Berlin, Heidelberg, 2003. https://doi.org/10.1007/978-3-662-05287-7.

[88] C. Kittel, Introduction to solid state physics, 8th ed., John Wiley & Sons, New York, 2005.

[89] A. Majumdar, Microscale Heat Conduction in Dielectric Thin Films, J Heat Transfer. 115 (1993) 7–16. https://doi.org/10.1115/1.2910673.

[90] J.B.J. Fourier, A. Freeman, The Analytical Theory of Heat, Cambridge University Press, 1878.

[91] R. Franz, G. Wiedemann, Ueber die Wärme-Leitungsfähigkeit der Metalle, Annalen Der Physik Und Chemie. 165 (1853) 497–531. https://doi.org/10.1002/andp.18531650802.

[92] Z. Lin, L. v. Zhigilei, V. Celli, Electron-phonon coupling and electron heat capacity of metals under conditions of strong electron-phonon nonequilibrium, Phys Rev B Condens Matter Mater Phys. 77 (2008). https://doi.org/10.1103/PhysRevB.77.075133.

[93] N.W. Ashcroft, D.N. Mermin, Solid State Physics, Holt, Rinehart and Winston, New York, 1976.

[94] W. Lv, A. Henry, Examining the Validity of the Phonon Gas Model in Amorphous Materials, Sci Rep. 6 (2016). https://doi.org/10.1038/srep37675.

[95] G.A. Elbaz, W.L. Ong, E.A. Doud, P. Kim, D.W. Paley, X. Roy, J.A. Malen, Phonon Speed, Not Scattering, Differentiates Thermal Transport in Lead Halide Perovskites, Nano Lett. 17 (2017) 5734–5739. https://doi.org/10.1021/acs.nanolett.7b02696.

[96] M.A. Haque, S. Kee, D.R. Villalva, W.L. Ong, D. Baran, Halide Perovskites: Thermal Transport and Prospects for Thermoelectricity, Advanced Science. 7 (2020). https://doi.org/10.1002/advs.201903389.

[97] M.K. Jana, K. Biswas, Crystalline Solids with Intrinsically Low Lattice Thermal Conductivity for Thermoelectric Energy Conversion, ACS Energy Lett. 3 (2018) 1315–1324. https://doi.org/10.1021/acsenergylett.8b00435.

[98] L. Lindsay, C. Hua, X.L. Ruan, S. Lee, Survey of ab initio phonon thermal transport, Materials Today Physics. 7 (2018) 106–120. https://doi.org/10.1016/j.mtphys.2018.11.008.

[99] W.L. Ong, E.S. O'Brien, P.S.M. Dougherty, D.W. Paley, C. Fred Higgs, A.J.H. McGaughey, J.A. Malen, X. Roy, Orientational order controls crystalline and amorphous thermal transport in superatomic crystals, Nat Mater. 16 (2017) 83–88. https://doi.org/10.1038/nmat4739.

[100] T. Haeger, R. Heiderhoff, T. Riedl, Thermal properties of metal-halide perovskites, J Mater Chem C Mater. 8 (2020) 14289–14311. https://doi.org/10.1039/d0tc03754k.

[101] T. Haeger, M. Ketterer, J. Bahr, N. Pourdavoud, M. Runkel, R. Heiderhoff, T. Riedl, Thermal properties of CsPbCl3 thin films across phase transitions, Journal of Physics: Materials. 3 (2020) 024044. https://doi.org/10.1088/2515-7639/ab749d.

[102] T. Handa, T. Yamada, M. Nagai, Y. Kanemitsu, Phonon, thermal, and thermo-optical properties of halide perovskites, Physical Chemistry Chemical Physics. 22 (2020) 26069–26087. https://doi.org/10.1039/d0cp04426a.

[103] T. Hata, G. Giorgi, K. Yamashita, The Effects of the Organic-Inorganic Interactions on the Thermal Transport Properties of CH3NH3PbI3, Nano Lett. 16 (2016) 2749–2753. https://doi.org/10.1021/acs.nanolett.6b00457.

[104] H. Xie, S. Hao, J. Bao, T.J. Slade, G.J. Snyder, C. Wolverton, M.G. Kanatzidis, All-Inorganic Halide Perovskites as Potential Thermoelectric Materials: Dynamic Cation off-Centering Induces Ultralow Thermal Conductivity, J Am Chem Soc. 142 (2020) 9553–9563. https://doi.org/10.1021/jacs.0c03427.

[105] M. Wang, S. Lin, Anisotropic and Ultralow Phonon Thermal Transport in Organic–Inorganic Hybrid Perovskites: Atomistic Insights into Solar Cell Thermal Management and Thermoelectric Energy Conversion Efficiency, Adv Funct Mater. 26 (2016) 5297–5306. https://doi.org/10.1002/adfm.201600284.

[106] X. Qian, X. Gu, R. Yang, Lattice thermal conductivity of organic-inorganic hybrid perovskite CH3NH3PbI3, Appl Phys Lett. 108 (2016). https://doi.org/10.1063/1.4941921.

[107] C. Caddeo, C. Melis, M.I. Saba, A. Filippetti, L. Colombo, A. Mattoni, Tuning the thermal conductivity of methylammonium lead halide by the molecular substructure, Physical Chemistry Chemical Physics. 18 (2016) 24318–24324. https://doi.org/10.1039/c6cp04246e.

[108] S.Y. Yue, X. Zhang, G. Qin, J. Yang, M. Hu, Insight into the collective vibrational modes driving ultralow thermal conductivity of perovskite solar cells, Phys Rev B. 94 (2016). https://doi.org/10.1103/PhysRevB.94.115427.

[109] A. Giri, A.Z. Chen, A. Mattoni, K. Aryana, D. Zhang, X. Hu, S.H. Lee, J.J. Choi, P.E. Hopkins, Ultralow thermal conductivity of two-dimensional metal halide perovskites, Nano Lett. 20 (2020) 3331–3337. https://doi.org/10.1021/acs.nanolett.0c00214.

[110] Z.-K. Liu, L.-Q. Chen, K. Rajan, Linking Length Scales via Materials Informatics, JOM. 58 (2006) 42–50. https://doi.org/10.1007/s11837-006-0226-2.

[111] M.R. Tonks, L.K. Aagesen, The Phase Field Method: Mesoscale Simulation Aiding Material Discovery Keywords mesoscale modeling and simulation, phase field method, material discovery, Annu Rev Mater Res. 49 (2019) 79–102. https://doi.org/10.1146/annurev-matsci-070218-010151.

[112] P. Saxena, N.E. Gorji, COMSOL Simulation of Heat Distribution in Perovskite Solar Cells: Coupled Optical-Electrical-Thermal 3-D Analysis, IEEE J Photovolt. 9 (2019) 1693–1698. https://doi.org/10.1109/JPHOTOV.2019.2940886.

[113] S. Zandi, P. Saxena, N.E. Gorji, Numerical simulation of heat distribution in RGO-contacted perovskite solar cells using COMSOL, Solar Energy. 197 (2020) 105–110. https://doi.org/10.1016/j.solener.2019.12.050.

[114] Y.F. Makableh, I. Abu Awad, W. Hassan, G. Aljaiuossi, Enhancement of the thermal properties of heterojunction perovskite solar cells by nanostructured contacts design, Solar Energy. 202 (2020) 204–209. https://doi.org/10.1016/j.solener.2020.04.002.

[115] S. Hirotsu, J. Harada, M. Iizumi, K. Gesi, Structural Phase Transistions in CsPbBr3, J Physical Soc Japan. 37 (1974) 1393–1398. https://doi.org/10.1143/JPSJ.37.1393.

[116] Y. Fujii, S. Hoshino, Y. Yarnada, G. Shirane, Neutron-scattering study on phase transitions of CsPbCl3, Phys Rev B. 9 (1974) 4549–4559. https://doi.org/10.1103/PhysRevB.9.4549.

[117] L. Kubičár, V. Boháč, K. Nitsch, Thermophysical Properties of the CsPbCl3 Single Crystal Using Pulse Transient Method, Int J Thermophys. 21 (2000) 571–583. https://doi.org/10.1023/A:1006668520775.

[118] W. Lee, H. Li, A.B. Wong, D. Zhang, M. Lai, Y. Yu, Q. Kong, E. Lin, J.J. Urban, J.C. Grossman, P. Yang, Ultralow thermal conductivity in all-inorganic halide perovskites, Proceedings of the National Academy of Sciences. 114 (2017) 8693–8697. https://doi.org/10.1073/pnas.1711744114.

[119] Y. Wang, R. Lin, P. Zhu, Q. Zheng, Q. Wang, D. Li, J. Zhu, Cation Dynamics Governed Thermal Properties of Lead Halide Perovskite Nanowires, Nano Lett. 18 (2018) 2772–2779. https://doi.org/10.1021/acs.nanolett.7b04437.

[120] N. Onoda-Yamamuro, T. Matsuo, H. Suga, Calorimetric and IR spectroscopic studies of phase transitions in methylammonium trihalogenoplumbates (II)†, Journal of Physics and Chemistry of Solids. 51 (1990) 1383–1395. https://doi.org/10.1016/0022-3697(90)90021-7.

[121] A. Pisoni, J. Jaćimović, O.S. Barišić, M. Spina, R. Gaál, L. Forró, E. Horváth, Ultra-low thermal conductivity in organic-inorganic hybrid perovskite CH3NH3PbI3, Journal of Physical Chemistry Letters. 5 (2014) 2488–2492. https://doi.org/10.1021/jz5012109.

[122] R.R. Heikes, R.W. Ure, Thermoelectricity: science and engineering, Interscience Publishers, New York, London, 1961.

[123] A. Kovalsky, L. Wang, G.T. Marek, C. Burda, J.S. Dyck, Thermal Conductivity of CH3NH3PbI3 and CsPbI3: Measuring the Effect of the Methylammonium Ion on Phonon Scattering, Journal of Physical Chemistry C. 121 (2017) 3228–3233. https://doi.org/10.1021/acs.jpcc.6b12231.

[124] Y. He, G. Galli, Perovskites for Solar Thermoelectric Applications: A First Principle Study of $CH_3NH_3AI_3$ (A = Pb and Sn), Chemistry of Materials. 26 (2014) 5394–5400. https://doi.org/10.1021/cm5026766.

[125] X. Mettan, R. Pisoni, P. Matus, A. Pisoni, J. Jaćimović, B. Náfrádi, M. Spina, D. Pavuna, L. Forró, E. Horváth, Tuning of the thermoelectric figure of merit of CH3NH3MI3 (M=Pb,Sn) photovoltaic perovskites, Journal of Physical Chemistry C. 119 (2015) 11506–11510. https://doi.org/10.1021/acs.jpcc.5b03939.

[126] C. Motta, F. El-Mellouhi, S. Sanvito, Charge carrier mobility in hybrid halide perovskites, Sci Rep. 5 (2015) 12746. https://doi.org/10.1038/srep12746.

[127] S.D. Stranks, G.E. Eperon, G. Grancini, C. Menelaou, M.J.P. Alcocer, T. Leijtens, L.M. Herz, A. Petrozza, H.J. Snaith, Electron-Hole Diffusion Lengths Exceeding 1 Micrometer in an Organometal Trihalide Perovskite Absorber, Science (1979). 342 (2013) 341–344. https://doi.org/10.1126/science.1243982.

[128] T. Ye, X. Wang, X. Li, A.Q. Yan, S. Ramakrishna, J. Xu, Ultra-high Seebeck coefficient and low thermal conductivity of a centimeter-sized perovskite single crystal acquired by a modified fast growth method, J Mater Chem C Mater. 5 (2017) 1255–1260. https://doi.org/10.1039/c6tc04594d.

[129] Z. Guo, S.J. Yoon, J.S. Manser, P. v. Kamat, T. Luo, Structural Phase- and Degradation-Dependent Thermal Conductivity of $CH_3NH_3PbI_3$ Perovskite Thin Films, The Journal of Physical Chemistry C. 120 (2016) 6394–6401. https://doi.org/10.1021/acs.jpcc.6b00513.

[130] Q. Chen, C. Zhang, M. Zhu, S. Liu, M.E. Siemens, S. Gu, J. Zhu, J. Shen, X. Wu, C. Liao, J. Zhang, X. Wang, M. Xiao, Efficient thermal conductance in organometallic perovskite CH3NH3PbI3 films, Appl Phys Lett. 108 (2016). https://doi.org/10.1063/1.4942779.

[131] P. Gill, T.T. Moghadam, B. Ranjbar, Differential scanning calorimetry techniques: applications in biology and nanoscience., J Biomol Tech. 21 (2010) 167–93. http://www.ncbi.nlm.nih.gov/pubmed/21119929.

[132] W.J. Parker, R.J. Jenkins, C.P. Butler, G.L. Abbott, Flash method of determining thermal diffusivity, heat capacity, and thermal conductivity, J Appl Phys. 32 (1961) 1679–1684. https://doi.org/10.1063/1.1728417.

[133] A. Rosencwaig, J. Opsal, W.L. Smith, D.L. Willenborg, Detection of thermal waves through optical reflectance, Appl Phys Lett. 46 (1985) 1013–1015. https://doi.org/10.1063/1.95794.

[134] I. Hatta, Y. Sasuga, R. Kato, A. Maesono, Thermal diffusivity measurement of thin films by means of an ac calorimetric method, Review of Scientific Instruments. 56 (1985) 1643–1647. https://doi.org/10.1063/1.1138117.

[135] Z. Hu, L. Aigouy, Z. Chen, D. Fournier, Thermal conductivity and diffusivity of triple-cation perovskite halide materials for solar cells, J Appl Phys. 127 (2020). https://doi.org/10.1063/1.5138480.

[136] F. Xu, C. Frétigny, D. Fournier, L. Belliard, S. Vincent, B. Perrin, S. Martin, C. Secouard, J.Y. Duquesne, Lateral heat diffusion investigation of a layered structure: Application to the complete thermal characterization of a lithium phosphorous oxynitride film, J Appl Phys. 113 (2013). https://doi.org/10.1063/1.4811520.

[137] A. Merdasa, M. Bag, Y. Tian, E. Källman, A. Dobrovolsky, I.G. Scheblykin, Super-resolution luminescence microspectroscopy reveals the mechanism of photoinduced degradation in CH3NH3PbI3 perovskite nanocrystals, Journal of Physical Chemistry C. 120 (2016) 10711–10719. https://doi.org/10.1021/acs.jpcc.6b03512.

[138] C. Quarti, E. Mosconi, J.M. Ball, V. D'Innocenzo, C. Tao, S. Pathak, H.J. Snaith, A. Petrozza, F. de Angelis, Structural and optical properties of methylammonium lead iodide across the tetragonal to cubic phase transition: Implications for perovskite solar cells, Energy Environ Sci. 9 (2016) 155–163. https://doi.org/10.1039/c5ee02925b.

[139] N. Yi, S. Wang, Z. Duan, K. Wang, Q. Song, S. Xiao, Tailoring the Performances of Lead Halide Perovskite Devices with Electron-Beam Irradiation, Advanced Materials. 29 (2017). https://doi.org/10.1002/adma.201701636.

[140] S. Saini, A.K. Baranwal, T. Yabuki, S. Hayase, K. Miyazaki, Growth of halide perovskites thin films for thermoelectric applications, MRS Adv. 4 (2019) 1719–1725. https://doi.org/10.1557/adv.2019.279.

[141] T. Liu, X. Zhao, J. Li, Z. Liu, F. Liscio, S. Milita, B.C. Schroeder, O. Fenwick, Enhanced control of self-doping in halide perovskites for improved thermoelectric performance, Nat Commun. 10 (2019). https://doi.org/10.1038/s41467-019-13773-3.

[142] A.K. Baranwal, S. Saini, Z. Wang, D. Hirotani, T. Yabuki, S. Iikubo, K. Miyazaki, S. Hayase, Interface engineering using Y2O3 scaffold to enhance the thermoelectric performance of CsSnI3 thin film, Org Electron. 76 (2020). https://doi.org/10.1016/j.orgel.2019.105488.

[143] F. Hao, C.C. Stoumpos, D.H. Cao, R.P.H. Chang, M.G. Kanatzidis, Lead-free solid-state organic-inorganic halide perovskite solar cells, Nat Photonics. 8 (2014) 489–494. https://doi.org/10.1038/nphoton.2014.82.

[144] B.W. Park, B. Philippe, X. Zhang, H. Rensmo, G. Boschloo, E.M.J. Johansson, Bismuth Based Hybrid Perovskites A3Bi2I9 (A: Methylammonium or Cesium) for Solar Cell Application, Advanced Materials. 27 (2015) 6806–6813. https://doi.org/10.1002/adma.201501978.

[145] X. Long, Z. Pan, Z. Zhang, J.J. Urban, H. Wang, Solvent-free synthesis of organometallic halides CH3NH3PbI3 and (CH3NH3)3Bi2I9 and their thermoelectric transport properties, Appl Phys Lett. 115 (2019). https://doi.org/10.1063/1.5113535.

[146] H. Ma, C. Li, Y. Ma, H. Wang, Z.W. Rouse, Z. Zhang, C. Slebodnick, A. Alatas, S.P. Baker, J.J. Urban, Z. Tian, Supercompliant and Soft (CH3NH3)3Bi2 I9 Crystal with Ultralow Thermal Conductivity, Phys Rev Lett. 123 (2019). https://doi.org/10.1103/PhysRevLett.123.155901.

[147] C.A. Paddock, G.L. Eesley, Transient thermoreflectance from thin metal films, J Appl Phys. 60 (1986) 285–290. https://doi.org/10.1063/1.337642.

[148] A. Mandelis, Frequency modulated (FM) time delay photoacoustic and photothermal wave spectroscopies. Technique, instrumentation, and detection. Part I: Theoretical, Review of Scientific Instruments. 57 (1986) 617–621. https://doi.org/10.1063/1.1138879.

[149] S. Govorkov, W. Ruderman, M.W. Horn, R.B. Goodman, M. Rothschild, A new method for measuring thermal conductivity of thin films, Review of Scientific Instruments. 68 (1997) 3828–3834. https://doi.org/10.1063/1.1148035.

[150] D.G. Cahill, Analysis of heat flow in layered structures for time-domain thermoreflectance, Review of Scientific Instruments. 75 (2004) 5119–5122. https://doi.org/10.1063/1.1819431.

[151] A.J. Schmidt, R. Cheaito, M. Chiesa, A frequency-domain thermoreflectance method for the characterization of thermal properties, Review of Scientific Instruments. 80 (2009). https://doi.org/10.1063/1.3212673.

[152] T. Liu, S.Y. Yue, S. Ratnasingham, T. Degousée, P. Varsini, J. Briscoe, M.A. McLachlan, M. Hu, O. Fenwick, Unusual Thermal Boundary Resistance in Halide Perovskites: A Way to Tune Ultralow Thermal Conductivity for Thermoelectrics, ACS Appl Mater Interfaces. 11 (2019) 47507–47515. https://doi.org/10.1021/acsami.9b14174.

[153] M.A. Haque, M.I. Nugraha, S.H.K. Paleti, D. Baran, Role of Compositional Tuning on Thermoelectric Parameters of Hybrid Halide Perovskites, Journal of Physical Chemistry C. (2019). https://doi.org/10.1021/acs.jpcc.9b02830.

[154] J.C. Jaeger, H.S. Carslaw, Conduction of Heat in Solids, Oxford University Press, 1989.

[155] G.B.M. Fiege, A. Altes, R. Heiderhoff, L.J. Balk, Quantitative thermal conductivity measurements with nanometre resolution, J Phys D Appl Phys. 32 (1999) L13–L17. https://doi.org/10.1088/0022-3727/32/5/003.

[156] D.G. Cahill, Thermal conductivity measurement from 30 to 750 K: The 3ω method, Review of Scientific Instruments. 61 (1990) 802–808. https://doi.org/10.1063/1.1141498.

[157] D.G. Cahill, P. v. Braun, G. Chen, D.R. Clarke, S. Fan, K.E. Goodson, P. Keblinski, W.P. King, G.D. Mahan, A. Majumdar, H.J. Maris, S.R. Phillpot, E. Pop, L. Shi, Nanoscale thermal transport. II. 2003-2012, Appl Phys Rev. 1 (2014). https://doi.org/10.1063/1.4832615.

[158] T. Luo, G. Chen, Nanoscale heat transfer-from computation to experiment, Physical Chemistry Chemical Physics. 15 (2013) 3389–3412. https://doi.org/10.1039/c2cp43771f.

[159] S. Adachi, Lattice thermal conductivity of group-IV and III-V semiconductor alloys, J Appl Phys. 102 (2007). https://doi.org/10.1063/1.2779259.

[160] MatWeb, Http://Www.Matweb.Com/. (2020).

[161] S. Adachi, Physical properties of III-V semiconductor compounds: InP, InAs, GaAs, GaP, InGaAs, and InGaAsP, Wiley, 1992.

[162] S. Adachi, Earth-Abundant Materials for Solar Cells: Cu2-II-IV-VI4 Semiconductors, John Wiley & Sons, Chichester, UK, 2015.

[163] B. Russ, A. Glaudell, J.J. Urban, M.L. Chabinyc, R.A. Segalman, Organic thermoelectric materials for energy harvesting and temperature control, Nat Rev Mater. 1 (2016). https://doi.org/10.1038/natrevmats.2016.50.

[164] J.C. Duda, P.E. Hopkins, Y. Shen, M.C. Gupta, Thermal transport in organic semiconducting polymers, Appl Phys Lett. 102 (2013). https://doi.org/10.1063/1.4812234.

[165] J.W. Valvano, B. Engineering, J.T. Allen, M.F. Bowman, The Simultaneous Measurement of Thermal Conductivity, Thermal Diffusivity, and Perfusion in Small Volumes of Tissue, 1984. http://biomechanical.asmedigitalcollection.asme.org/.

[166] T.A. Balasubramaniam, H.F. Bowman, Thermal Conductivity and Thermal Diffusivity of Biomaterials: A Simultaneous Measurement Technique, J Biomech Eng. 99 (1977) 148–154. https://doi.org/10.1115/1.3426282.

[167] P. Nesvadba, Methods for the measurement of thermal conductivity and diffusivity of foodstuffs, J Food Eng. 1 (1982) 93–113. https://doi.org/10.1016/0260-8774(82)90003-6.

[168] A. Makris, T. Haeger, R. Heiderhoff, T. Riedl, From diffusive to ballistic Stefan-Boltzmann heat transport in thin non-crystalline films, RSC Adv. 6 (2016) 94193–94199. https://doi.org/10.1039/c6ra20407d.

[169] R. Heiderhoff, T. Haeger, K. Dawada, T. Riedl, From diffusive in-plane to ballistic out-of-plane heat transport in thin non-crystalline films, Microelectronics Reliability. 76–77 (2017) 222–226. https://doi.org/10.1016/j.microrel.2017.06.064.

[170] A. Sood, F. Xiong, S. Chen, R. Cheaito, F. Lian, M. Asheghi, Y. Cui, D. Donadio, K.E. Goodson, E. Pop, Quasi-Ballistic Thermal Transport Across MoS 2 Thin Films, Nano Lett. 19 (2019) 2434–2442. https://doi.org/10.1021/acs.nanolett.8b05174.

[171] M. Nonnenmacher, H.K. Wickramasinghe, Scanning probe microscopy of thermal conductivity and subsurface properties, Appl Phys Lett. 61 (1992) 168–170. https://doi.org/10.1063/1.108207.

[172] M.J. Pylkki, R.J. Balk, Imaging of Local Thermal and Electrical Conductivity with Scanning Force Microscopy, 1994. https://digitalcommons.usu.edu/microscopyAvailableat:https://digitalcommons.usu.edu/microscopy/vol8/iss2/4.

[173] R.J. Pylkki, P.J. Moyer, P.E. West, Scanning Near-Field Optical Microscopy and Scanning Thermal Microscopy, Jpn J Appl Phys. 33 (1994) 3785–3790. https://doi.org/10.1143/JJAP.33.3785.

[174] Bruker Corporation, VITA-HE-GLA-1 by Bruker, Https://Www.Brukerafmprobes.Com/p-3705-Vita-He-Gla-1.Aspx. (2022).

[175] A. Altes, R. Heiderhoff, L.J. Balk, Quantitative dynamic near-field microscopy of thermal conductivity, J Phys D Appl Phys. 37 (2004) 952–963. https://doi.org/10.1088/0022-3727/37/6/023.

[176] A.A. Wilson, M. Muñoz Rojo, B. Abad, J.A. Perez, J. Maiz, J. Schomacker, M. Martín-Gonzalez, D.A. Borca-Tasciuc, T. Borca-Tasciuc, Thermal conductivity measurements of high and low thermal conductivity films using a scanning hot probe method in the 3ω mode and novel calibration strategies, Nanoscale. 7 (2015) 15404–15412. https://doi.org/10.1039/c5nr03274a.

[177] A. Altes, R. Heiderhoff, L.J. Balk, Quantitative dynamic near-field microscopy of thermal conductivity, J Phys D Appl Phys. 37 (2004) 952–963. https://doi.org/10.1088/0022-3727/37/6/023.

[178] R. Heiderhoff, T. Haeger, K. Dawada, T. Riedl, From diffusive in-plane to ballistic out-of-plane heat transport in thin non-crystalline films, Microelectronics Reliability. 6 (2017) 94193–94199. https://doi.org/10.1016/j.microrel.2017.06.064.

[179] T. Haeger, M. Wilmes, R. Heiderhoff, T. Riedl, Simultaneous Mapping of Thermal Conductivity, Thermal Diffusivity, and Volumetric Heat Capacity of Halide Perovskite Thin Films: A Novel Nanoscopic Thermal Measurement Technique, Journal of Physical Chemistry Letters. 10 (2019) 3019–3023. https://doi.org/10.1021/acs.jpclett.9b01053.

[180] A. Altes, K. Mutamba, R. Heiderhoff, H.L. Hartnagel, L.J. Balk, Scanning near field thermal microscopy on a micromachined thin membrane, Superlattices Microstruct. 35 (2004) 465–476. https://doi.org/10.1016/j.spmi.2003.09.008.

[181] N. Onoda-Yamamuro, T. Matsuo, H. Suga, Calorimetric and IR spectroscopic studies of phase transitions in methylammonium trihalogenoplumbates, Journal of Physics and Chemistry of Solids. 51 (1990) 1383–1395. https://doi.org/10.1016/0022-3697(90)90021-7.

[182] Schott, https://www.schott.com/de-de/products/borofloat-p1000314, BOROFLOAT® 33. (2022).

[183] Maximilian Wilmes, Erfassung des Kation-Einflusses auf die thermischen Eigenschaften von Perowskiten, Bergische Universität Wuppertal, 2018.

[184] A. Cappella, J.-L. Battaglia, V. Schick, A. Kusiak, A. Lamperti, C. Wiemer, B. Hay, High Temperature Thermal Conductivity of Amorphous Al_2O_3 Thin Films Grown by Low Temperature ALD, Adv Eng Mater. 15 (2013) 1046–1050. https://doi.org/10.1002/adem.201300132.

[185] A. Cappella, J.-L. Battaglia, V. Schick, A. Kusiak, A. Lamperti, C. Wiemer, B. Hay, High Temperature Thermal Conductivity of Amorphous Al_2O_3 Thin Films Grown by Low Temperature ALD, Adv Eng Mater. 15 (2013) 1046–1050. https://doi.org/10.1002/adem.201300132.

[186] B. Barbés, R. Páramo, E. Blanco, M.J. Pastoriza-Gallego, M.M. Piñeiro, J.L. Legido, C. Casanova, Thermal conductivity and specific heat capacity measurements of Al 2O3 nanofluids, J Therm Anal Calorim. 111 (2013) 1615–1625. https://doi.org/10.1007/s10973-012-2534-9.

[187] M.D. Groner, F.H. Fabreguette, J.W. Elam, S.M. George, Low-Temperature Al2O3 Atomic Layer Deposition, Chemistry of Materials. 16 (2004) 639–645. https://doi.org/10.1021/cm0304546.

[188] L. Hoffmann, Spatial atomic layer deposition of electrically (non-)conductive gas diffusion barriers, Bergische Universität Wuppertal, 2018.

[189] A. Mayer, M. Buchmüller, S. Wang, C. Steinberg, M. Papenheim, H.-C. Scheer, N. Pourdavoud, T. Haeger, T. Riedl, Thermal nanoimprint to improve the morphology of MAPbX3 (MA = methylammonium, X = I or Br), Journal of Vacuum Science & Technology B, Nanotechnology and Microelectronics: Materials, Processing, Measurement, and Phenomena. 35 (2017) 06G803. https://doi.org/10.1116/1.4991619.

[190] N. Pourdavoud, T. Haeger, A. Mayer, P.J. Cegielski, A.L. Giesecke, R. Heiderhoff, S. Olthof, S. Zaefferer, I. Shutsko, A. Henkel, D. Becker-Koch, M. Stein, M. Cehovski, O. Charfi, H. Johannes, D. Rogalla, M.C. Lemme, M. Koch, Y. Vaynzof, K. Meerholz, W. Kowalsky, H. Scheer, P. Görrn, T. Riedl, Room-Temperature Stimulated Emission and Lasing in Recrystallized Cesium Lead Bromide Perovskite Thin Films, Advanced Materials. 31 (2019) 1903717. https://doi.org/10.1002/adma.201903717.

[191] N. Pourdavoud, Stimulated Emission and Lasing in Metal Halide Perovskites by Direct Thermal Nanoimprint, Bergische Universität Wuppertal, 2020. https://doi.org/10.25926/b4j1-zj06.

[192] N. Pourdavoud, S. Wang, A. Mayer, T. Hu, Y. Chen, A. Marianovich, W. Kowalsky, R. Heiderhoff, H.C. Scheer, T. Riedl, Photonic Nanostructures Patterned by Thermal Nanoimprint Directly into Organo-Metal Halide Perovskites, Advanced Materials. 29 (2017). https://doi.org/10.1002/adma.201605003.

[193] A. Mayer, T. Haeger, M. Runkel, J. Staabs, J. Rond, F. van gen Hassend, P. Görrn, T. Riedl, H.-C. Scheer, Direct patterning of methylammonium lead bromide perovskites by thermal imprint, Applied Physics A. 128 (2022) 399. https://doi.org/10.1007/s00339-022-05521-0.

[194] A. Mayer, K. Dhima, S. Möllenbeck, S. Wang, H.-C. Scheer, A novel tool for frequency assisted thermal nanoimprint (T-NIL), in: 28th European Mask and Lithography Conference, SPIE, 2012: p. 83520N. https://doi.org/10.1117/12.918037.

[195] C. Steinberg, K. Dhima, D. Blenskens, A. Mayer, S. Wang, M. Papenheim, H.C. Scheer, J. Zajadacz, K. Zimmer, A scalable anti-sticking layer process via controlled evaporation, Microelectron Eng. 123 (2014) 4–8. https://doi.org/10.1016/j.mee.2014.04.002.

[196] A. Mayer, T. Haeger, M. Runkel, J. Rond, J. Staabs, F. van gen Hassend, A. Röttger, P. Görrn, T. Riedl, H.C. Scheer, Relevance of processing parameters for grain growth of metal halide perovskites with nanoimprint, Appl Phys A Mater Sci Process. 127 (2021). https://doi.org/10.1007/s00339-021-04830-0.

[197] J. Li, H. Wang, X.Y. Chin, H.A. Dewi, K. Vergeer, T.W. Goh, J.W.M. Lim, J.H. Lew, K.P. Loh, C. Soci, T.C. Sum, H.J. Bolink, N. Mathews, S. Mhaisalkar, A. Bruno, Highly Efficient Thermally Co-evaporated Perovskite Solar Cells and Mini-modules, Joule. 4 (2020) 1035–1053. https://doi.org/10.1016/j.joule.2020.03.005.

[198] P. Gui, H. Zhou, F. Yao, Z. Song, B. Li, G. Fang, Space-Confined Growth of Individual Wide Bandgap Single Crystal $CsPbCl_3$ Microplatelet for Near-Ultraviolet Photodetection, Small. 15 (2019) 1902618. https://doi.org/10.1002/smll.201902618.

[199] Dr. Detlef Rogalla, https://www.rubion.rub.de/de/methods/rbs-rutherford-backscattering-spectrometry/, RUBION Webpage. (2022).

[200] Merck / Sigma-Aldrich, Cesium chloride - ≥99.999% trace metals basis - specification sheet, Https://Www.Sigmaaldrich.Com/DE/En/Product/Aldrich/203025. (2022).

[201] Merck / Sigma-Aldrich, Lead(II) chloride - 99.999% trace metals basis - specification sheet, Https://Www.Sigmaaldrich.Com/DE/En/Product/Aldrich/203572. (2022).

[202] J. Ye, M.M. Byranvand, C.O. Martínez, R.L.Z. Hoye, M. Saliba, L. Polavarapu, Defect Passivation in Lead-Halide Perovskite Nanocrystals and Thin Films: Toward Efficient LEDs and Solar Cells, Angewandte Chemie International Edition. 60 (2021) 21636–21660. https://doi.org/10.1002/anie.202102360.

[203] T. Ahmed, S. Seth, A. Samanta, Boosting the Photoluminescence of CsPbX3 (X = Cl, Br, I) Perovskite Nanocrystals Covering a Wide Wavelength Range by Postsynthetic Treatment with Tetrafluoroborate Salts, Chemistry of Materials. 30 (2018) 3633–3637. https://doi.org/10.1021/acs.chemmater.8b01235.

[204] G.H. Ahmed, J.K. El-Demellawi, J. Yin, J. Pan, D.B. Velusamy, M.N. Hedhili, E. Alarousu, O.M. Bakr, H.N. Alshareef, O.F. Mohammed, Giant Photoluminescence Enhancement in CsPbCl3 Perovskite Nanocrystals by Simultaneous Dual-Surface Passivation, ACS Energy Lett. 3 (2018) 2301–2307. https://doi.org/10.1021/acsenergylett.8b01441.

[205] R.K. Behera, S. das Adhikari, S.K. Dutta, A. Dutta, N. Pradhan, Blue-Emitting CsPbCl 3 Nanocrystals: Impact of Surface Passivation for Unprecedented Enhancement and Loss of Optical Emission, Journal of Physical Chemistry Letters. 9 (2018) 6884–6891. https://doi.org/10.1021/acs.jpclett.8b03047.

[206] D.P. Nenon, K. Pressler, J. Kang, B.A. Koscher, J.H. Olshansky, W.T. Osowiecki, M.A. Koc, L.-W. Wang, A.P. Alivisatos, Design Principles for Trap-Free CsPbX 3 Nanocrystals: Enumerating and Eliminating Surface Halide Vacancies with Softer Lewis Bases, J Am Chem Soc. 140 (2018) 17760–17772. https://doi.org/10.1021/jacs.8b11035.

[207] W. Wei, Y. Zhang, Q. Xu, H. Wei, Y. Fang, Q. Wang, Y. Deng, T. Li, A. Gruverman, L. Cao, J. Huang, Monolithic integration of hybrid perovskite single crystals with heterogenous substrate for highly sensitive X-ray imaging, Nat Photonics. 11 (2017) 315–321. https://doi.org/10.1038/nphoton.2017.43.

[208] Y. Liu, Y. Zhang, Z. Yang, J. Feng, Z. Xu, Q. Li, M. Hu, H. Ye, X. Zhang, M. Liu, K. Zhao, S. Liu, Low-temperature-gradient crystallization for multi-inch high-quality perovskite single crystals for record performance photodetectors, Materials Today. 22 (2019) 67–75. https://doi.org/10.1016/j.mattod.2018.04.002.

[209] J. Ding, S. Du, Z. Zuo, Y. Zhao, H. Cui, X. Zhan, High Detectivity and Rapid Response in Perovskite CsPbBr3 Single-Crystal Photodetector, The Journal of Physical Chemistry C. 121 (2017) 4917–4923. https://doi.org/10.1021/acs.jpcc.7b01171.

[210] M.I. Saidaminov, A.L. Abdelhady, B. Murali, E. Alarousu, V.M. Burlakov, W. Peng, I. Dursun, L. Wang, Y. He, G. Maculan, A. Goriely, T. Wu, O.F. Mohammed, O.M. Bakr, High-quality bulk hybrid perovskite single crystals within minutes by inverse temperature crystallization, Nat Commun. 6 (2015) 7586. https://doi.org/10.1038/ncomms8586.

[211] D. Shi, V. Adinolfi, R. Comin, M. Yuan, E. Alarousu, A. Buin, Y. Chen, S. Hoogland, A. Rothenberger, K. Katsiev, Y. Losovyj, X. Zhang, P.A. Dowben, O.F. Mohammed, E.H. Sargent, O.M. Bakr, Low trap-state density and long carrier diffusion in organolead trihalide perovskite single crystals, Science (1979). 347 (2015) 519–522. https://doi.org/10.1126/science.aaa2725.

[212] H. Zhang, X. Liu, J. Dong, H. Yu, C. Zhou, B. Zhang, Y. Xu, W. Jie, Centimeter-sized inorganic lead halide perovskite CsPbBr3 crystals grown by an improved solution method, Cryst Growth Des. 17 (2017) 6426–6431. https://doi.org/10.1021/acs.cgd.7b01086.

[213] H. Zhang, X. Liu, J. Dong, H. Yu, C. Zhou, B. Zhang, Y. Xu, W. Jie, Centimeter-sized inorganic lead halide perovskite CsPbBr3 crystals grown by an improved solution method, Cryst Growth Des. 17 (2017) 6426–6431. https://doi.org/10.1021/acs.cgd.7b01086.

[214] C. Zhang, J. Yuan, J.K.W. Ho, J. Song, H. Zhong, Y. Xiao, W. Liu, X. Lu, Y. Zou, S.K. So, Correlating the Molecular Structure of A-DA′D-A Type Non-Fullerene Acceptors to Its Heat Transfer and Charge Transport Properties in Organic Solar Cells, Adv Funct Mater. 31 (2021). https://doi.org/10.1002/adfm.202101627.

[215] S. Sun, Y. Fang, G. Kieslich, T.J. White, A.K. Cheetham, Mechanical properties of organic-inorganic halide perovskites, CH3NH3PbX3 (X = I, Br and Cl), by nanoindentation, J Mater Chem A Mater. 3 (2015) 18450–18455. https://doi.org/10.1039/c5ta03331d.

[216] A. Mehdizadeh, S.F. Akhtarianfar, S. Shojaei, Role of Methylammonium Rotation in Hybrid Halide MAPbX3 (X = I, Br, and Cl) Perovskites by a Density Functional Theory Approach: Optical and Electronic Properties, Journal of Physical Chemistry C. 123 (2019) 6725–6734. https://doi.org/10.1021/acs.jpcc.8b11422.

[217] O. Hentz, Z. Zhao, S. Gradečak, Impacts of Ion Segregation on Local Optical Properties in Mixed Halide Perovskite Films, Nano Lett. 16 (2016) 1485–1490. https://doi.org/10.1021/acs.nanolett.5b05181.

[218] M.I. Dar, G. Jacopin, M. Hezam, N. Arora, S.M. Zakeeruddin, B. Deveaud, M.K. Nazeeruddin, M. Grätzel, Asymmetric Cathodoluminescence Emission in CH3NH3PbI3-xBrx Perovskite Single Crystals, ACS Photonics. 3 (2016) 947–952. https://doi.org/10.1021/acsphotonics.6b00290.

[219] C. Xiao, Z. Li, H. Guthrey, J. Moseley, Y. Yang, S. Wozny, H. Moutinho, B. To, J.J. Berry, B. Gorman, Y. Yan, K. Zhu, M. Al-Jassim, Mechanisms of Electron-Beam-Induced Damage in Perovskite Thin Films Revealed by Cathodoluminescence Spectroscopy, Journal of Physical Chemistry C. 119 (2015) 26904–26911. https://doi.org/10.1021/acs.jpcc.5b09698.

[220] Z. Zhang, Y. Zhu, W. Wang, W. Zheng, R. Lin, F. Huang, Growth, characterization and optoelectronic applications of pure-phase large-area CsPb $_2$ Br $_5$ flake single crystals, J Mater Chem C Mater. 6 (2018) 446–451. https://doi.org/10.1039/C7TC04834C.

[221] M.A. Haque, A.N. Gandi, R. Mohanraman, Y. Weng, B. Davaasuren, A.H. Emwas, C. Combe, D. Baran, A. Rothenberger, U. Schwingenschlögl, H.N. Alshareef, S. Dong, T. Wu, A 0D Lead-Free Hybrid Crystal with Ultralow Thermal Conductivity, Adv Funct Mater. 29 (2019). https://doi.org/10.1002/adfm.201809166.

[222] V.K. Ravi, G.B. Markad, A. Nag, Band Edge Energies and Excitonic Transition Probabilities of Colloidal CsPbX3 (X = Cl, Br, I) Perovskite Nanocrystals, ACS Energy Lett. 1 (2016) 665–671. https://doi.org/10.1021/acsenergylett.6b00337.

[223] K. Nitsch, A. Cihlar, M. Dusek, V. Hamplova, M. Nikl, M. Rodova, N. Rysava, Growth and Characterization of Crystals of Incongruently Melting Ternary Alkali Lead Chlorides, n.d.

[224] L. Kubičár, V. Vretenár, V. Boháč, Study of phase transitions by transient methods, Solid State Phenomena. 138 (2008) 3–28. https://doi.org/10.4028/www.scientific.net/SSP.138.3.

[225] G.J. Snyder, E.S. Toberer, Complex thermoelectric materials, Nat Mater. 7 (2008) 105–114. https://doi.org/10.1038/nmat2090.

[226] T. Haeger, M. Wilmes, J. Bahr, N. Pourdavoud, S. Zaefferer, R. Heiderhoff, T. Riedl, Thermal properties of highly oriented all-inorganic CsPbX3 (X=Br, Cl) perovskite films: dependence on halide, dimensionality, and crystal-phase, in: MRS Fall Meeting - EN09.15.02, Boston, Massachusetts, 2019.

[227] E. Haque, M.A. Hossain, Origin of ultra-low lattice thermal conductivity in Cs2BiAgX6 (X=Cl, Br) and its impact on thermoelectric performance, J Alloys Compd. 748 (2018) 63–72. https://doi.org/10.1016/j.jallcom.2018.03.137.

[228] X. He, M. Krogstad, M.K. Gupta, T. Lanigan-Atkins, C. Mao, F. Ye, Y. Liu, T. Hong, S. Chi, H. Wei, J. Huang, S. Rosenkranz, R. Osborn, O. Delaire, Multiple lattice instabilities and complex ground state in Cs$_2$AgBiBr$_6$, (2021). http://arxiv.org/abs/2112.04717.

[229] Z. Zhang, G. Yang, C. Zhou, C.C. Chung, I. Hany, Optical and electrical properties of all-inorganic Cs2AgBiBr6 double perovskite single crystals, RSC Adv. 9 (2019) 23459–23464. https://doi.org/10.1039/c9ra04045e.

[230] E. Haque, M.A. Hossain, Electronic, phonon transport and thermoelectric properties of Cs 2 InAgCl 6 from first-principles study, Computational Condensed Matter. 19 (2019). https://doi.org/10.1016/j.cocom.2019.e00374.

[231] D. Yao, X. Mao, X. Wang, Y. Yang, N.D. Pham, A. Du, P. Chen, L. Wang, G.J. Wilson, H. Wang, Dimensionality-Controlled Surface Passivation for Enhancing Performance and Stability of Perovskite Solar Cells via Triethylenetetramine Vapor, ACS Appl Mater Interfaces. 12 (2020) 6651–6661. https://doi.org/10.1021/acsami.9b19908.

[232] A. Behrendt, C. Friedenberger, T. Gahlmann, S. Trost, T. Becker, K. Zilberberg, A. Polywka, P. Görrn, T. Riedl, Highly Robust Transparent and Conductive Gas Diffusion Barriers Based on Tin Oxide, Advanced Materials. 27 (2015) 5961–5967. https://doi.org/10.1002/adma.201502973.

[233] L. Hoffmann, K.O. Brinkmann, J. Malerczyk, D. Rogalla, T. Becker, D. Theirich, I. Shutsko, P. Görrn, T. Riedl, Spatial Atmospheric Pressure Atomic Layer Deposition of Tin Oxide as an Impermeable Electron Extraction Layer for Perovskite Solar Cells with Enhanced Thermal Stability, ACS Appl Mater Interfaces. 10 (2018) 6006–6013. https://doi.org/10.1021/acsami.7b17701.

[234] K.O. Brinkmann, J. Zhao, N. Pourdavoud, T. Becker, T. Hu, S. Olthof, K. Meerholz, L. Hoffmann, T. Gahlmann, R. Heiderhoff, M.F. Oszajca, N.A. Luechinger, D. Rogalla, Y. Chen, B. Cheng, T. Riedl, Suppressed decomposition of organometal halide perovskites by impermeable electron-extraction layers in inverted solar cells, Nat Commun. 8 (2017). https://doi.org/10.1038/ncomms13938.

[235] N. Rolston, K.A. Bush, A.D. Printz, A. Gold-Parker, Y. Ding, M.F. Toney, M.D. McGehee, R.H. Dauskardt, Engineering Stress in Perovskite Solar Cells to Improve Stability, Adv Energy Mater. 8 (2018). https://doi.org/10.1002/aenm.201802139.

[236] K.A. Bush, N. Rolston, A. Gold-Parker, S. Manzoor, J. Hausele, Z.J. Yu, J.A. Raiford, R. Cheacharoen, Z.C. Holman, M.F. Toney, R.H. Dauskardt, M.D. McGehee, Controlling Thin-Film Stress and Wrinkling during Perovskite Film Formation, ACS Energy Lett. 3 (2018) 1225–1232. https://doi.org/10.1021/acsenergylett.8b00544.

[237] D.J. Xue, Y. Hou, S.C. Liu, M. Wei, B. Chen, Z. Huang, Z. Li, B. Sun, A.H. Proppe, Y. Dong, M.I. Saidaminov, S.O. Kelley, J.S. Hu, E.H. Sargent, Regulating strain in perovskite thin films through charge-transport layers, Nat Commun. 11 (2020). https://doi.org/10.1038/s41467-020-15338-1.

[238] S. Adjokatse, H.H. Fang, M.A. Loi, Broadly tunable metal halide perovskites for solid-state light-emission applications, Materials Today. 20 (2017) 413–424. https://doi.org/10.1016/j.mattod.2017.03.021.

[239] J. Zhao, K.O. Brinkmann, T. Hu, N. Pourdavoud, T. Becker, T. Gahlmann, R. Heiderhoff, A. Polywka, P. Görrn, Y. Chen, B. Cheng, T. Riedl, Self-Encapsulating Thermostable and Air-Resilient Semitransparent Perovskite Solar Cells, Adv Energy Mater. 7 (2017). https://doi.org/10.1002/aenm.201602599.

[240] C.C. Boyd, R. Cheacharoen, T. Leijtens, M.D. McGehee, Understanding Degradation Mechanisms and Improving Stability of Perovskite Photovoltaics, Chem Rev. 119 (2019) 3418–3451. https://doi.org/10.1021/acs.chemrev.8b00336.

[241] G. Schileo, G. Grancini, Halide perovskites: current issues and new strategies to push material and device stability, JPhys Energy. 2 (2020). https://doi.org/10.1088/2515-7655/ab6cc4.

[242] U. Krishnan, M. Kaur, M. Kumar, A. Kumar, Factors affecting the stability of perovskite solar cells: a comprehensive review, J Photonics Energy. 9 (2019) 1. https://doi.org/10.1117/1.JPE.9.021001.

[243] U. Fotheringham, Thermal Properties of Glass, in: 1998: pp. 201–228. https://doi.org/10.1007/978-3-642-57769-7_5.

[244] T. Ashida, A. Miyamura, N. Oka, Y. Sato, T. Yagi, N. Taketoshi, T. Baba, Y. Shigesato, Thermal transport properties of polycrystalline tin-doped indium oxide films, J Appl Phys. 105 (2009). https://doi.org/10.1063/1.3093684.

[245] J.H. Pöhls, M.B. Johnson, M.A. White, Origins of ultralow thermal conductivity in bulk [6,6]-phenyl-C61-butyric acid methyl ester (PCBM), Physical Chemistry Chemical Physics. 18 (2016) 1185–1190. https://doi.org/10.1039/c5cp06575e.

[246] J. Liu, X. Wang, D. Li, N.E. Coates, R.A. Segalman, D.G. Cahill, Thermal conductivity and elastic constants of PEDOT:PSS with high electrical conductivity, Macromolecules. 48 (2015) 585–591. https://doi.org/10.1021/ma502099t.

[247] N. Oka, K. Kimura, T. Yagi, N. Taketoshi, T. Baba, Y. Shigesato, Thermophysical and electrical properties of Al-doped ZnO films, J Appl Phys. 111 (2012). https://doi.org/10.1063/1.4706572.

[248] Korth Kristalle GmbH, https://www.korth.de/index.php/162/items/34.html, (n.d.).

[249] S. Olthof, T. Riedl, Metal-Oxide Interface Materials for Organic and Perovskite Solar Cells, in: 2019: pp. 61–104. https://doi.org/10.1142/9789813270541_0003.

[250] J. Meyer, S. Hamwi, M. Kröger, W. Kowalsky, T. Riedl, A. Kahn, Transition metal oxides for organic electronics: Energetics, device physics and applications, Advanced Materials. 24 (2012) 5408–5427. https://doi.org/10.1002/adma.201201630.

[251] M. Acik, S.B. Darling, Graphene in perovskite solar cells: Device design, characterization and implementation, J Mater Chem A Mater. 4 (2016) 6185–6235. https://doi.org/10.1039/c5ta09911k.

[252] F. Guo, H. Azimi, Y. Hou, T. Przybilla, M. Hu, C. Bronnbauer, S. Langner, E. Spiecker, K. Forberich, C.J. Brabec, High-performance semitransparent perovskite solar cells with solution-processed silver nanowires as top electrodes, Nanoscale. 7 (2015) 1642–1649. https://doi.org/10.1039/c4nr06033d.

[253] S. Sandell, J. Maire, E. Chávez-ángel, C.M.S. Torres, H. Kristiansen, Z. Zhang, J. He, Enhancement of thermal boundary conductance of metal–polymer system, Nanomaterials. 10 (2020). https://doi.org/10.3390/nano10040670.

[254] S.G. Kandlikar, Review and projections of integrated cooling systems for three-dimensional integrated circuits, Journal of Electronic Packaging, Transactions of the ASME. 136 (2014). https://doi.org/10.1115/1.4027175.

[255] F.L. Tan, S.C. Fok, Thermal Management of Mobile Phone using Phase Change Material, in: 2007 9th Electron. Packag. Technol. Conf. (2 VOLS), 2007: pp. 836–842.

[256] J.D. Renteria, D.L. Nika, A.A. Balandin, Graphene thermal properties: Applications in thermal management and energy storage, Applied Sciences (Switzerland). 4 (2014) 525–547. https://doi.org/10.3390/app4040525.

[257] H. Ibach, H. Lüth, Festkörperphysik, Springer Berlin Heidelberg, Berlin, Heidelberg, 1999. https://doi.org/10.1007/978-3-662-07211-0.

[258] T.J. Whitcher, L.C. Gomes, D. Zhao, M. Bosman, X. Chi, Y. Wang, A. Carvalho, H.K. Hui, Q. Chang, M.B.H. Breese, A.H. Castro Neto, A.T.S. Wee, H.D. Sun, E.E.M. Chia, A. Rusydi, Dual phases of crystalline and electronic structures in the nanocrystalline perovskite CsPbBr3, NPG Asia Mater. 11 (2019) 70. https://doi.org/10.1038/s41427-019-0170-6.

[259] C. Shen, W. Du, Z. Wu, J. Xing, S.T. Ha, Q. Shang, W. Xu, Q. Xiong, X. Liu, Q. Zhang, Thermal conductivity of suspended single crystal CH3NH3PbI3 platelets at room temperature, Nanoscale. 9 (2017) 8281–8287. https://doi.org/10.1039/c7nr01894k.

[260] O. Knop, R.E. Wasylishen, M. Anne White, T. Stanley Cameron, M.J. M Van Oort, Alkylammonium lead halides. Part 2. CH3NH3PbX3 (X = C1, Br, I) perovskites: cuboctahedral halide cages with isotropic cation reorientation1, n.d.

[261] H. Zhu, Y. Fu, F. Meng, X. Wu, Z. Gong, Q. Ding, M. v. Gustafsson, M.T. Trinh, S. Jin, X.Y. Zhu, Lead halide perovskite nanowire lasers with low lasing thresholds and high quality factors, Nat Mater. 14 (2015) 636–642. https://doi.org/10.1038/nmat4271.

[262] N.J. Jeon, J.H. Noh, Y.C. Kim, W.S. Yang, S. Ryu, S. il Seok, Solvent engineering for high-performance inorganic-organic hybrid perovskite solar cells, Nat Mater. 13 (2014) 897–903. https://doi.org/10.1038/nmat4014.

Author's Publications and Conference Contributions

Publications

1. A. Mayer, **T. Haeger**, M. Runkel, J. Staabs, J. Rond, F. van gen Hassend, P. Görrn, T. Riedl, H.-C. Scheer, Direct patterning of methylammonium lead bromide perovskites by thermal imprint, Applied Physics A. 128 (2022) 399. https://doi.org/10.1007/s00339-022-05521-0.

2. K. Brinkmann, T. Becker, F. Zimmermann, T. Gahlmann, M. Theisen, **T. Haeger**, S. Olthof, C. Kreusel, M. Günster, T. Maschwitz, F. Göbelsmann, C. Koch, D. Hertel, P. Caprioglio, L. Perdigon, A. Al-Ashouri, 23.5% efficient monolithic perovskite/organic tandem solar cells based on an ultra-thin metal-like metal-oxide interconnect, Nature. 604 (2022) 280–286. https://doi.org/10.1038/s41586-022-04455-0.

3. L. Gomell, **T. Haeger**, M. Roscher, H. Bishara, R. Heiderhoff, T. Riedl, C. Scheu, B. Gault, Microstructure manipulation by laser-surface remelting of a full-Heusler compound to enhance thermoelectric properties, Acta Materialia. 223 (2022) 117501. https://doi.org/10.1016/j.actamat.2021.117501.

4. K.O. Brinkmann, T. Becker, F. Zimmermann, C. Kreusel, T. Gahlmann, **T. Haeger**, T. Riedl, The Optical Origin of Near-Unity External Quantum Efficiencies in Perovskite Solar Cells, Solar RRL. 5 (2021). https://doi.org/10.1002/solr.202100371.

5. A. Mayer, **T. Haeger**, M. Runkel, J. Rond, J. Staabs, F. van gen Hassend, A. Röttger, P. Görrn, T. Riedl, H.C. Scheer, Relevance of processing parameters for grain growth of metal halide perovskites with nanoimprint, Applied Physics A: Materials Science and Processing. 127 (2021). https://doi.org/10.1007/s00339-021-04830-0.

6. T. Gahlmann, T. Tschorn, T. Maschwitz, L. Gomell, **T. Haeger**, G. Grötsch, R. Heiderhoff, T. Riedl, Bifacial Color-Tunable Electroluminescent Devices, ACS Applied Materials and Interfaces. 13 (2021) 28514–28520. https://doi.org/10.1021/acsami.1c08360.

7. **T. Haeger**, R. Heiderhoff, T. Riedl, Thermal properties of metal-halide perovskites, Journal of Materials Chemistry C. 8 (2020) 14289–14311. https://doi.org/10.1039/d0tc03754k.

8. N. Boysen, B. Misimi, A. Muriqi, J.L. Wree, T. Hasselmann, D. Rogalla, T. Haeger, D. Theirich, M. Nolan, T. Riedl, A. Devi, A carbene stabilized precursor for the spatial atomic layer deposition of copper thin films, Chemical Communications. 56 (2020) 13752–13755. https://doi.org/10.1039/d0cc05781a.

9. **T. Haeger**, M. Ketterer, J. Bahr, N. Pourdavoud, M. Runkel, R. Heiderhoff, T. Riedl, Thermal properties of $CsPbCl_3$ thin films across phase transitions, Journal of Physics: Materials. 3 (2020) 024044. https://doi.org/10.1088/2515-7639/ab749d.

10. C. Tückmantel, U. Kalita, **T. Haeger**, M. Theisen, U. Pfeiffer, T. Riedl, Amorphous Indium-Gallium-Zinc-Oxide TFTs Patterned by Self-Aligned Photolithography Overcoming the GHz Threshold, IEEE Electron Device Letters. 41 (2020) 1786–1789. https://doi.org/10.1109/LED.2020.3029956.

11. C. Kriso, M. Stein, **T. Haeger**, N. Pourdavoud, M. Gerhard, A. Rahimi-Iman, T. Riedl, M. Koch, Nonlinear refraction in $CH_3NH_3PbBr_3$ single crystals, Optics Letters. 45 (2020) 2431–2434. https://doi.org/10.1364/OL.383917.

12. N. Pourdavoud, **T. Haeger**, A. Mayer, P.J. Cegielski, A.L. Giesecke, R. Heiderhoff, S. Olthof, S. Zaefferer, I. Shutsko, A. Henkel, D. Becker-Koch, M. Stein, M. Cehovski, O. Charfi, H. Johannes, D. Rogalla, M.C. Lemme, M. Koch, Y. Vaynzof, K. Meerholz, W. Kowalsky, H. Scheer, P. Görrn, T. Riedl, Room-Temperature Stimulated Emission and Lasing in Recrystallized Cesium Lead Bromide Perovskite Thin Films, Advanced Materials. 31 (2019) 1903717. https://doi.org/10.1002/adma.201903717.

13. **T. Haeger**, M. Wilmes, R. Heiderhoff, T. Riedl, Simultaneous Mapping of Thermal Conductivity, Thermal Diffusivity, and Volumetric Heat Capacity of Halide Perovskite Thin Films: A Novel Nanoscopic Thermal Measurement Technique, Journal of Physical Chemistry Letters. 10 (2019) 3019–3023. https://doi.org/10.1021/acs.jpclett.9b01053.

14. N. Pourdavoud, A. Mayer, M. Buchmüller, K. Brinkmann, **T. Haeger**, T. Hu, R. Heiderhoff, I. Shutsko, P. Görrn, Y. Chen, H.-C. Scheer, T. Riedl, Distributed Feedback Lasers Based on MAPbBr$_3$, Advanced Materials Technologies. 3 (2018) 1700253. https://doi.org/10.1002/admt.201700253.

15. R. Heiderhoff, **T. Haeger**, N. Pourdavoud, T. Hu, M. Al-Khafaji, A. Mayer, Y. Chen, H.C. Scheer, T. Riedl, Thermal Conductivity of Methylammonium Lead Halide Perovskite Single Crystals and Thin Films: A Comparative Study, Journal of Physical Chemistry C. 121 (2017) 28306–28311. https://doi.org/10.1021/acs.jpcc.7b11495.

16. A. Mayer, M. Buchmüller, S. Wang, C. Steinberg, M. Papenheim, H.-C. Scheer, N. Pourdavoud, **T. Haeger**, T. Riedl, Thermal nanoimprint to improve the morphology of MAPbX3 (MA = methylammonium, X = I or Br), Journal of Vacuum Science & Technology B, Nanotechnology and Microelectronics: Materials, Processing, Measurement, and Phenomena. 35 (2017) 06G803. https://doi.org/10.1116/1.4991619.

17. R. Heiderhoff, **T. Haeger**, K. Dawada, T. Riedl, From diffusive in-plane to ballistic out-of-plane heat transport in thin non-crystalline films, Microelectronics Reliability. 76–77 (2017) 222–226. https://doi.org/10.1016/j.microrel.2017.06.064.

18. A. Makris, **T. Haeger**, R. Heiderhoff, T. Riedl, From diffusive to ballistic Stefan-Boltzmann heat transport in thin non-crystalline films, RSC Advances. 6 (2016) 94193–94199. https://doi.org/10.1039/c6ra20407d.

Conference contributions

1. **T. Haeger**, M. Ketterer, R. Heiderhoff, and T. Riedl:
   Thermal Properties of Large Crystalline $CsPbBr_3$ Perovskite Thin Films—Remarkable Behavior at Phase Transitions
   MRS Fall Meeting, Boston (USA), EN05.04.10 (2021).

2. K. O. Brinkmann, T. Becker, F. Zimmermann, C. Kreusel, T. Gahlmann, **T. Haeger**, and T. Riedl:
   Optical Origin of External Quantum Efficiencies near Unity in Perovskite Solar Cells
   MRS Fall Meeting, Boston (USA), EN05.09.16 (2021).

3. M. Runkel, **T. Haeger**, H. Ping, J. Bahr, L. Merten, S. Olthof, D. Rogalla, A. Hinderhofer, R. Heiderhoff, F. Schreiber, K. Meerholz, and T. Riedl:
   Room-Temperature Amplified Spontaneous Emission and Lasing of Sequentially Thermally Evaporated $CsPbCl_3$ Perovskite Thin Films
   MRS Fall Meeting, Boston (USA), EN08.02.04 (2021).

4. C. Tückmantel, U. Kalita, **T. Haeger**, M. Theisen, U. Pfeiffer, and T. Riedl:
   Self-Aligned Amorphous Indium-Gallium-Zinc-Oxide TFTs Breaking the GHz Threshold
   MRS Fall Meeting, Boston (USA), EQ11.04.03 (2021).

5. K. O. Brinkmann, T. Becker, F. Zimmermann, C. Kreusel, T. Gahlmann, M. Theisen, **T. Haeger**, S. Olthof, M. Günster, T. Maschwitz, F. Göbelsmann, C. Koch, D. Hertel, P. Caprioglio, L. Perdigon, L. Merten, A. Hinderhofer, A. Al-Ashouri, L. Gomell, F. Schreiber, S. Albrecht, K. Meerholz, D. Neher, M. Stolterfoht, and T. Riedl:
   No Need for Tin - Perovskite/Organic Tandem Solar Cells Approaching 24% MRS Fall Meeting, Boston (USA), EN05.03.01 (2021).

6. **T. Haeger**, M. Runkel, N. Pourdavoud, R. Heiderhoff, J. Bahr, and T. Riedl: Room temperature amplified spontaneous emission and lasing in $CsPbCl_3$ spontaneously formed in superlattices of $PbCl_2/CsCl$

   SPIE Organic Photonics + Electronics, Proc. SPIE 11473, Organic and Hybrid Light Emitting Materials and Devices XXIV, 1147319 (20 August 2020), DOI: 10.1117/12.2568611

7. C. Kriso, M. Stein, **T. Haeger**, N. Pourdavoud, M. Gerhard, A. Rahimi-Iman, T. Riedl, and M. Koch:

   Nonlinear optical properties of metal halide perovskite single crystals

   Conference on Lasers and Electro-Optics, JTh2E.14 (2020)

8. E. Shkura, D. Theirich, K. Brinkmann, **T. Haeger**, J. Schneidewind, M. Siebert, and T. Riedl: Atomic Layer Etching at Atmospheric Pressure

   19th Conference on Atomic Layer Deposition, Seattle (USA) ALE2-TuM16 (2019)

9. **T. Haeger**, M. Wilmes, J. Bahr, N. Pourdavoud, S. Zaefferer, R. Heiderhoff, T. Riedl:

   Thermal properties of highly oriented all-inorganic $CsPbX_3$ (X=Br, Cl) perovskite films: dependence on halide, dimensionality, and crystal-phase

   2019 MRS Fall Meeting, EN09.15.02, Hynes Convention Center, Boston, Massachusetts, USA, December 1-6, (2019)

10. A. Mayer, N. Pourdavoud, **T. Haeger**, R. Heiderhoff, M. Leifels, J. Rond, J. Staabs, P. Görrn, T. Riedl, H. Scheer:

    Imprint-induced grain growth in perovskite layers

    45th International Conference on Micro & Nano Engineering, Rodos Palace Hotel, Rhodes, Greece, September 23rd - 26th, (2019)

11. **T. Haeger**, R. Heiderhoff, and T. Riedl:

    Thermal properties of all-inorganic halide perovskites: dependence on dimensionality and crystal-phase

    2019 E-MRS Fall Meeting, T.9.1, Warsaw University of Technology, September 16 to 19, Warsaw, Poland (2019)

12. **T. Haeger**, M. Wilmes, R. Heiderhoff, and T. Riedl:

    Mapping the low thermal conductivity of lead-halide based perovskite films with high spatial resolution

    2018 MRS Fall Meeting, November 25-30, Hynes Convention Center and Sheraton Boston Hotel, Boston, Massachusetts (2018), Session TP02

13. N. Pourdavoud, A. Mayer, **T. Haeger**, R. Heiderhoff, I. Shutsko, H.-C. Scheer, P. Görrn, and T. Riedl:

    Ultra-smooth perovskite thin films for lasers

    SPIE Optics and Photonics, San Diego (USA), Proc. SPIE 10724, Physical Chemistry of Semiconductor Materials and Interfaces XVII, 107240C (17 September 2018) doi.org/10.1117/12.2319364

14. N. Pourdavoud, A. Mayer, K.O. Brinkmann, **T. Haeger**, R. Heiderhoff, I. Shutsko, P. Görrn, I. Peschke, H.-C. Scheer, T. Riedl:

    Low-Threshold $MAPbBr_3$ Distributed Feedback Laser Prepared by Direct Thermal Nanoimprint of Resonator Gratings into Perovskite

    2017 MRS Fall Meeting, November 26-December 1, Hynes Convention Center and Sheraton Boston Hotel, Boston, Massachusetts (2017).

15. R. Heiderhoff, **T. Haeger**, K. Dawada, and T. Riedl:

    SThM of disparate anisotropic heat transports in thin non-crystalline films

    European Materials Research Society Fall Meeting 2017 (E-MRS 2017) 18th-21st September 2017, Warsaw University of Technology – Poland

16. N. Pourdavoud, A. Mayer, S. Wang, M. Buchmüller, K. Brinkmann, **T. Haeger**, T. Hu, R. Heiderhoff, A. Marianovich, I. Shutsko, P. Görrn, Y. Chen, W. Kowalsky, H.-C. Scheer, T. Riedl:

    Low-threshold Distributed Feedback Lasers Prepared By Direct Thermal Nanoimprint Of Resonator Gratings Into Organometal Halide Perovskites

    Nature Photonics, Photonics @ SG, Singapore, 3-1D-5, 2017.

17. R. Heiderhoff, **T. Haeger**, K. Dawada, and T. Riedl:

    From diffusive in-plane to ballistic out-of-plane heat transport in thin non-crystalline films

    presented at ESREF 2017, 28th European Symposium on Reliability of Electron Devices, Failure Physics and Analysis, September 25th -28th, Bordeaux, France, (2017), Microelectronics Reliability,76-77 (2017), 222-226, DOI: 10.1016/j.microrel.2017.06.064

18. A. Makris, **T. Haeger**, R. Heiderhoff, and T. Riedl:

    Diffusive to ballistic dynamic out-of-plane heat transport in thin films

    MRS Fall Meeting, Boston (USA) (2015), II2.03

Supervised Student Thesis

1. **Erfassung des Kation-Einflusses auf die thermischen Eigenschaften von Perowskiten**
   Maximilian Wilmes
   Bachelor Thesis (2018)

2. **Prozessierung und Charakterisierung von CsPbCl$_3$-Dünnschichten**
   Johannes Bahr
   Bachelor Thesis (2019)

3. **Die Erfassung der thermischen Eigenschaften von Cs$_X$Pb$_Y$Cl$_Z$-Perowskiten**
   Moritz Ketterer
   Bachelor Thesis (2019)

4. **Thermische Evaporation und Charakterisierung von CsPbCl$_3$-Dünnschichten**
   Huiyue Ping
   Bachelor Thesis (2021)

5. **Thermische Untersuchungen an IGZO-Dünnschichttransistoren**
   Björn Saborowski
   Bachelor Thesis (2022)